Evidence of Regional and Global Climate Change in the Mineral Aerosol (Dust) Record from Ice Cores Through the Anthropocene and Pleistocene

by

Sarah Miranda Aarons

A dissertation submitted in partial fulfillment
of the requirements for the degree of
Doctor of Philosophy
(Geology)
in the University of Michigan
2016

Doctoral Committee:

Assistant Professor Sarah M. Aciego, Co-Chair
Professor Joel D. Blum, Co-Chair
Associate Professor Jeremy N. Bassis
Assistant Professor Rose Cory
Assistant Professor Mark G. Flanner

ACKNOWLEDGMENTS

First I thank the University of Michigan, Rackham Graduate School, and the Department of Earth and Environmental Sciences for providing me with the opportunity to pursue my passion. My graduate experience would not be possible without the sponsorship and mentorship from my adviser, Dr. Sarah Aciego, who opened doors to me that allowed me to conduct fieldwork in some of the most beautiful places in the world. Her mentorship style allowed me to explore problems and research questions independently, and I know this will benefit me tremendously in the future. As Sarah's student, it is clear that she made a concerted effort to provide opportunities and educational outreach to students from diverse backgrounds, and I am appreciative of her efforts. I would also like to thank the other members of my dissertation committee: Dr. Joel Blum, Dr. Jeremy Bassis, Dr. Rose Cory, and Dr. Mark Flanner for their guidance and advice during my Ph.D.

I am also grateful for the support of others during my time as a graduate student. My colleagues, Carli, Molly, Yi-Wei, Emily and Mark provided companionship and emotional support during long workdays. Carli and Molly were exceptional field mates (and future roommates) and I am so grateful for the time we spent together. Life as a graduate student can be stressful, and my lab mates were

always there to support me when I needed it. There are many other unnamed graduate students in my cohort and I am thankful for their friendship and camaraderie.

I would like to acknowledge my Mom, Dad, sisters Miriam and Elizabeth and my remaining family members for their continuing emotional support throughout my Ph.D. work. Specifically, thank you to my dad who sparked my curiosity in the earth and taught me the power of using science to answer questions. I am grateful to my mom, who placed so much value and emphasis on the importance of obtaining an education. She taught me that education and knowledge provides empowerment, especially for underrepresented minorities. My Ph.D. degree has been a difficult journey, but my mom is the reason I have persisted. Finally, I would like to thank Nick, who is an endless source of reassurance and comfort.

TABLE OF CONTENTS

LIST OF FIGURES

Figure

LIST OF TABLES

Table

ABSTRACT

Dust in the atmosphere has a significant effect on earth's climate by scattering or absorption of incoming solar radiation, acting as cloud condensation nuclei, or providing critical nutrients to oceans and terrestrial biospheres. Changes in the locations of dust source areas and pathways can provide insight into understanding the relationship between mineral dust, global climate, and biogeochemical cycles. To gain a better understanding of the impact of the dust cycle on global and regional climate, the dust records within ice-cores from three locations are utilized to reconstruct changes in atmospheric circulation and dust provenance using radiogenic isotope data, trace and rare earth element composition, anion concentration, dust concentration, and size distribution. In this dissertation thesis, we applied this methodology to investigate three case studies. Ice-core samples from the Upper Fremont Glacier (UFG) in Wyoming, Taylor Dome, an East Antarctic ice-dome, and Taylor Glacier, the outlet glacier for Taylor Dome, are investigated here. In the UFG, we found that samples reveal anthropogenic influences. Variability in dust sources and pathways indicates a transition from far to near-range transport due to land-use changes

associated with agricultural activity and livestock grazing expansion during 1700 – 1975 A.D. Samples from Taylor Dome and Taylor Glacier, spanning the time period 1,800 – 55,000 years before present, indicate a shift from long-range transported dust to a more variable local input during the transition out of the last glacial period when global temperatures rose 4-7 degrees C. Dust sources and transport pathway changes reveal atmospheric circulation restructuring following the last climatic transition and subsequent retreat of the Ross Ice Shelf.

Chapter I

Introduction

1.1. Effect of Dust on climate

Fine-grained mineral dust particles are formed by the physical and chemical breakdown of rocks, via mechanical weathering through the constant force imposed by moving water or wind. Eolian processes concentrate these mineral particles (dust) into desert dunes, and the advance and retreat of glaciers or ice sheets leaves behind exposed silt, fine-grained crushed bedrock. Dust from these deserts and glacial processes is uplifted into the atmosphere by wind gusts and transported thousands of kilometers before being deposited on the global oceans, ice sheets and land. Where and when deposition occurs depends on the dominant wind direction and strength.

Dust suspended in the atmosphere can scatter or absorb incoming solar radiation or outgoing long-wave radiation, serve as cloud condensation nuclei, and lower the albedo of ice sheets, glaciers and snowpacks (Gaiero, 2007; Griffin et al., 2001; Harrison et al., 2001; Maher et al., 2010; Shao et al., 2011; Tegen et al., 1996). Dust is also recognized as a source of fertilization providing limiting nutrients (P, K, Mg, Na, Ca, Fe, Cu, Mn and Mo) in grassland, forest, river, lake

and marine ecoystems (McTainsh and Strong, 2007; Okin et al., 2004; Reynolds et al., 2001) and therefore may affect the global carbon cycle (Jickells et al., 2005; Mahowald et al., 2005; Martin, 1990). Dust deposition has a significant impact on ecosystems, for example the deposition of desert dust on semi-arid lands encourages the development of soil (Kohfeld and Harrison, 2001; McTainsh, 1984; Reheis et al., 2009; Reheis et al., 1995; Tsoar and Pye, 1987). Variations in the provenance of dust reaching a particular location can be a valuable indicator of changes in dust production, sources, and atmospheric transport pathways through time as a function of climate change. Thus, temporal changes in (1) locations of dust source areas and (2) the transport pathways that bring particles from source to depositional environment have implications for understanding the interactions between mineral dust, global climate, and biogeochemical cycles.

1.2. Climate change in ice record

One of the most reliable sources of global climate change records for the last 800 thousand years is the cryosphere – the frozen surface of the earth. The accumulation and compaction of snow forms ice sheets and ice caps in Antarctica, Greenland and high elevations at low latitudes, which flow outward from the accumulation area under their own weight (Figure 1.1). The ice at the base of an ice sheet is oldest, as younger ice accrues on top. As snow is compacted into ice three forms of records are preserved: precipitation in the form of snow and ice, atmospheric gases trapped in bubbles, and particles deposited

on the surface. Consequently, climate change over thousands of years is examined using ice cores: a long cylindrical core retrieved from an ice sheet or glacier, which can be more than 3000 meters long and encompass more than 800,000 years of climate history. Ice cores serve as indicators of past climate by serving as a proxy for temperature through physical and chemical examination of the atmospheric gas bubbles, isotopes of melted ice, and dust particles entrained within the ice (Delmonte et al., 2004a; Jouzel et al., 1997; Petit et al., 1999; Severinghaus and Brook, 1999). Ice cores are an ultra-pure and precise source for documenting variations in the relationship between greenhouse gases such as CO_2 and CH_4 in addition to other indicators of climate such as dust transport and young sea-ice extent (Delmonte et al., 2004a; Wolff, 2006).

1.3. Paleo-dust record in ice cores

Continental-derived dust that is transported throughout the atmosphere can be used as a tracer of air circulation and transport patterns (Basile et al., 1997; Delmonte et al., 2010; Grousset and Biscaye, 2005; Revel-Rolland et al., 2006). Chemical and physical characterization of dust transported in the atmosphere and deposited on ice sheets and glaciers provide information about the dust's source region, or provenance, the amount of material available for deflation into the atmosphere (e.g. aridity and land cover), and the dominant wind direction and speed. Combined, these factors provide insight into the regional and global climate conditions through time (Delmonte et al., 2004a; Fischer, 2007; Wolff, 2006). Physical measurements of dust, concentration and size, indicate short

versus long distance transport and can reveal changes in dust availability and dust flux. This information provides insight into hydrological and environmental changes such as variations in aridity and windiness occurring at the source area related to land-use and/or climate change.

Paleo-dust records preserved in ice cores from Greenland and Antarctica reveal distinguishable variations in dust emissions over glacial-interglacial timescales, and dust concentration is one-to-two orders of magnitude greater during glacial versus interglacial periods (Basile et al., 1997; Biscaye et al., 1997; Delmonte et al., 2004b; Delmonte et al., 2007; Grousset et al., 1992; Lambert et al., 2008; Petit et al., 1981; Petit et al., 1999; Revel-Rolland et al., 2006). The higher dust concentration during glacial periods is attributed to increased dust availability at dust source areas and stronger winds due to a strong equator-pole temperature gradient (Delmonte et al., 2004a; Hammer et al., 1985). The use of radiogenic isotopes have indicated that dust during the glacial periods in Antarctica is primarily sourced from South America despite the proximity of large dust sources in Australia, New Zealand, South Africa and the exposed areas in the Transantarctic Mountains (Basile et al., 1997; Delmonte et al., 2008; Delmonte et al., 2004a; Gaiero, 2007).

Reconstruction of paleoclimate and paleoenvironment records from ice cores originating from alpine glaciers in midlatitude regions provides high time resolution and regional records of climate change (Thompson et al., 1998;

Thompson et al., 2000). However, determining the sources and pathways of atmospheric mineral dust and marine aerosols remains a difficult problem. To address this issue, researchers have investigated mineralogy, elemental compositions, radiogenic isotopic compositions and size distributions of both potential source areas (PSAs) and dust deposited in ice from Europe, Asia, Antarctica and Greenland (Bory et al., 2003a; Bory et al., 2003b; Delmonte et al., 2004a; Delmonte et al., 2004b; McConnell et al., 2002; Thevenon et al., 2009; Thompson et al., 2000).

1.4. Rare Earth, Trace Elements and Dust Provenance

Chemical measurements of dust, radiogenic isotopic composition and trace and rare earth element (REE) analysis, compared to global dust source area chemical compositions provides a mechanism for determining the location of earth surface changes on short (~300 years) and glacial-interglacial timescales (Aarons et al., In Press; Aarons et al., in preparation; Gabrielli, 2010). REEs have been used as estimators of aeolian dust provenance changes on glacial-interglacial cycles in Antarctic ice from Dome C (Gabrielli, 2010). The 14 REEs (La, Ce, Pr, Nd, Sm, Eu, Gd, Tb, Dy, Ho, Er, Tm, Yb, Lu) range in atomic number from 57 (La) to 71 (Lu); the light REEs (LREEs) are La, Ce, Pr, Nd, the medium REEs (MREEs) are Sm, Eu, Gd, Tb, Dy, Ho and the heavy REEs (HREEs) are Er, Tm, Yb, Lu. An increasing atomic mass corresponds to a decreasing radius, however the external electronic configuration remains the same resulting in elements that maintain their chemical properties. As such, the lithophilic

refractory REEs behave similar to isotopes and are primarily transported in the particulate phase due to their low solubility. Recent studies of Antarctic and midlatitude ice cores (Gabrielli, 2010; Wegner et al., 2012; Zhang et al., 2009) used REEs to distinguish varying atmospheric transport processes and more importantly, to serve as an additional proxy for determining source areas of dust.

Trace elements (TE) in ice cores are a complementary tracer of dust, sea-salt, and anthropogenic input to ice (Hinkley, 2001; McConnell et al., 2002). Concentrations of sea-salt aerosols, often denoted as sea-salt sodium ($ssNa^+$), in Antarctic ice cores are two-to-three times higher in glacial versus interglacial periods despite the relatively small variations in proximity to the open ocean (Fischer, 2007). The shift in sea-salt aerosol flux is attributed to changes in summer sea ice extent, with younger sea ice producing more sea-salt deposition to the ice sheet. The amount of sea-salt Na^+ and calcium ($ssCa^{2+}$) versus non-sea-salt Na^+ and Ca^{2+} is determined using established ratios of sea-salt Ca^{2+}/ Na^+ (0.038) and average crustal Ca^{2+}/ Na^+ (1.78) (Rothlisberger et al., 2002), allowing measurements of trace elements to evaluate the proximity of non-permanent sea ice associated with the changing grounding line location of the Ross Ice Shelf. In midlatitude glaciers, other trace elements such as lead (Pb), arsenic (As) and zinc (Zn) are powerful indicators of air pollution from industrialization such as fossil fuel burning, smelting and coal mining (McConnell et al., 2002).

1.5. Principles of strontium and neodymium isotope geochemistry

Variable rubidium/strontium (Rb/Sr), and samarium/neodymium (Sm/Nd) ratios in the primary mineral constituents will lead to different $^{87}Sr/^{86}Sr$ and $^{143}Nd/^{144}Nd$ ratios in mineral dust, as the decay of parent isotopes rubidium-87 (^{87}Rb) and samarium-147 (^{147}Sm) lead to changes in the abundance of the daughter isotopes ^{87}Sr and ^{143}Nd respectively. The natural variability of Sr and Nd isotopic compositions are expressed as ratios of the abundances of the radiogenic daughter isotope to a non-radiogenic isotope of the same element. The abundance of ^{87}Sr and ^{143}Nd is compared against non-radiogenic ^{86}Sr and ^{144}Nd abundances respectively. The decay constants for the systems are all very small, the half-life of ^{87}Rb is 48.8 billion years and that of ^{147}Sm is 106 billion years. As a result of the slow elemental fractionation of Sm/Nd, the natural variability in Nd isotopic compositions is quite low, and for the sake of observing extremely small changes they are reported in epsilon notation: ε_{Nd}, which are deviations from the Chondritic Uniform Reservoir (CHUR) in parts per 10,000 as follows:

$$\varepsilon_{Nd} = ([(^{143}Nd/^{144}Nd)_{sample}/(^{143}Nd/^{144}Nd)_{CHUR}]-1) \times 10^4$$

where $(^{143}Nd/^{144}Nd)_{CHUR}$ is the Nd isotopic composition of CHUR which is $^{143}Nd/^{144}Nd=0.512638$ (Jacobsen and Wasserberg, 1980).

The evolution of the bulk earth over earth's history is assumed to be same as the evolution of CHUR in Nd isotopic composition. The major host phases of Nd in rock have similar Sm/Nd ratios (Taylor and McLennan, 1985), and as a result the weathering products are usually similar in Nd isotopic compositions compared to the rock it originates from. Strontium has been shown to fractionate with respect

to weathering (Biscaye, 1971; Goldstein and Jacobsen, 1987), and recent work indicates a significant isotopic variation in Sr occurring in airborne mineral dust with respect to distance from the source (Aarons et al., 2013).

1.6. Dust provenance and Radiogenic Isotopes

Continental-derived dust transported through the atmosphere can be used a tracer of paleo- air circulation and transport patterns (Basile et al., 1997; Delmonte et al., 2010; Grousset and Biscaye, 2005; Revel-Rolland et al., 2006). The radiogenic isotope compositions of dust are used as a proxy for paleoclimate and atmospheric circulation reconstruction on a regional and global scale (Harrison et al., 2001).

The chemical “fingerprinting” of ice core dust to a specific dust source area and physical measurements that indicate travel distance and flux impart a more complete understanding of the relationship between climate, land use change and dustiness. A powerful proxy for dust provenance determination is the radiogenic Sr and Nd isotopic composition (Biscaye et al., 1997; Grousset and Biscaye, 2005; Grousset et al., 1992). These tracers are considered robust indicators of source because the radiogenic isotopic compositions should show variability between source regions due to the varying geologic history and crustal age of each PSA. Neodymium isotopes ($^{143}Nd/^{144}Nd$) have been used to distinguish source areas with similar Sr ($^{87}Sr/^{86}Sr$) isotopic ratios and the combined Sr and Nd isotopic composition has been proven to be an excellent

"fingerprint" of dust source (Grousset and Biscaye, 2005). It has been demonstrated that Sr isotopic ratios are size fraction dependent (Dasch, 1969), whereas Nd isotopes are less sensitive to size fraction in loess and desert sands (Chen et al., 2007; Rao et al., 2006; Yokoo et al., 2004). Weathering is also noted to affect Sr isotopic ratios: the leaching of carbonates with low $^{87}Sr/^{86}Sr$ ratios results in an increase of the bulk sample's $^{87}Sr/^{86}Sr$ ratio with weathering (Blum and Erel, 1997). The primary difficulty in using these novel tools to investigate climate change is the amount of dust present is less than one milligram per kilogram of ice.

1.7. The Horizontal ice core

Traditional ice cores are expensive and logistically challenging to retrieve, and the small amount recovered ice places limitations on the amount and variety of analytical measurements. The extremely small concentration of dust present in Antarctic ice requires the collection of larger ice samples for more precise and accurate radiogenic isotope measurement. An alternative to traditional vertically drilled ice cores lies in the nature of glacier and ice sheet dynamics. Precipitation in the form of snow falls at the accumulation area of ice sheets and forms firn and eventually ice as it is compacted under its own weight. As ice sheets and glaciers move outwards towards the margins from the accumulation area, ice is re-exposed in the ablation area resulting in a horizontal exposure of ice stratigraphy. The exposed ice is oldest at the ice sheet margin (toe of glacier) and progressively younger towards the equilibrium line, or point of accumulation. The

horizontally exposed ice has been referred to as a “horizontal ice core” and has successfully provided paleoclimate reconstruction (Aciego et al., 2007; Reeh et al., 1991), and is notably useful to acquire previously unobtainable measurements of trace gases, isotopes of trace gases and low concentration particles (dust).

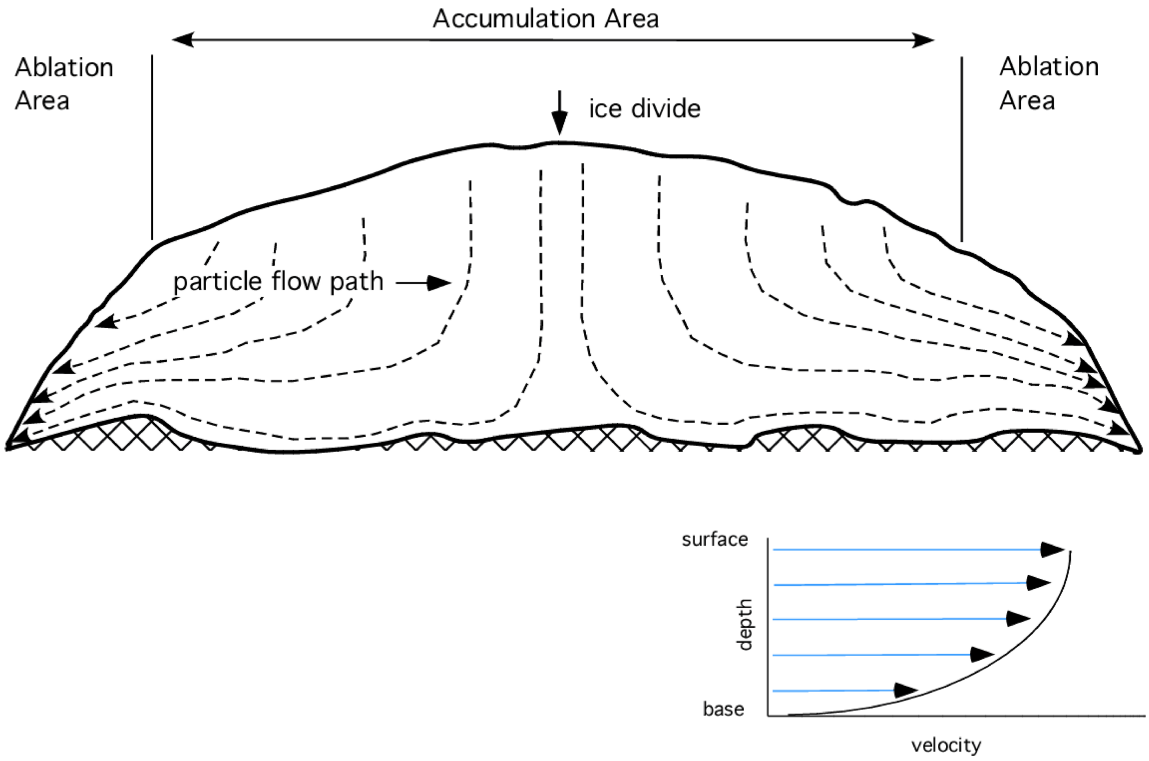

Figure 1.1. Schematic cross-section of ice sheet showing relative velocity, accumulation and ablation areas, ice divide, and particle flow path. Note particle flow path deforms with distance from the ice divide. (Figure courtesy S.M. Aciego).

1.8. Aims and motivation of this thesis

1.8.1. Taylor Dome and Taylor Glacier

We use high-precision geochemical techniques to the high-volume, high-resolution horizontal ice core at Taylor Glacier to deconvolve regional versus

global aerosol flux sources, determine if the changing climate and weather in the Ross Sea region from the LGM (21 ka) through the Preboreal Holocene is recorded by aerosol compositional changes and to provide a record of Southern Hemisphere dust through the Younger Dryas and Antarctic Cold Reversal. The movement of the Ross Ice Shelf grounding line, transition from ice sheet to ice shelf, and the establishment during the Holocene of atmospheric moisture transport from the south, which reduced snowfall on the north side of Taylor Dome (Figure 1.2a) and would have been one of the largest and most rapid climate and weather pattern change in the region (Morse et al., 1998). We establish baseline measurements of trace elements, anions and cations, and radiogenic isotopes of dust within the Taylor Dome and Taylor Glacier horizontal ice core and integrate our results into the current understanding of climate in the Ross Sea region, Antarctica.

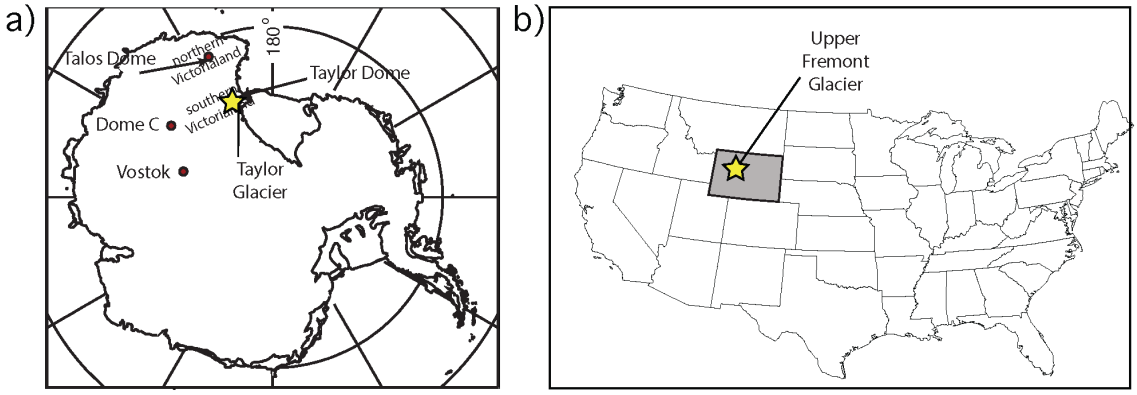

Figure 1.2. Map of Taylor Dome, Taylor Glacier, and Upper Fremont Glacier. a) Map of Taylor Dome and Taylor Glacier relative to Ross Sea and other major East Antarctic ice core drilling sites: Talos Dome, Dome C, Vostok. (Figure adapted from Morse et al., 1998). b) Map of Upper Fremont Glacier drilling site relative to United States.

1.8.2. Upper Fremont Glacier

The sources and transport pathways of aerosol dust particles deposited on midlatitude glaciers in North America are currently unknown. The goals of the work on the Upper Fremont Glacier ice core (Figure 1.2b) is to provide the first high resolution chemical and physical dataset of the dust cycle in the American West throughout the past 270 years, including throughout the Agricultural and Industrial Revolution. Additionally, we broadened the library of PSAs from North America and we integrate our results into the current understanding of recent climate in the American West, US, North America and globally to address anthropogenically driven changes in the dust cycle. We use the dust within the UFG ice to identify regional versus global aerosol flux sources to midlatitude glaciers. The geochemical results of this research may be used to better understand land use and climate change via geochemical mixing models.

1.9. Publications resulting from this dissertation

1) Aarons, S.M., Aciego, S.M., Gabrielli, P., Delmonte, B., Koornneef, J.M., Uglietti, C., Wegner, A., Blakowski, M.A., Bouman, C., *In Preparation*. Ice core evidence for variable dust sources in the western United States over the last 300 years. Chemical Geology, **(Chapter 2)**.

2) Aarons, S.M. Aciego, S.M., Gabrielli, P., Delmonte, B., Koornneef, J.M., Wegner, A., Blakowski, M.A. *In Press*. The impact of glacier retreat from the Ross Sea on local climate: characterization of mineral dust in the Taylor Dome ice core, East Antarctica. Earth and Planetary Science Letters, **(Chapter 3)**.

3) S.M. Aarons, S.M. Aciego, C.A. Arendt, M.A. Blakowski, A. Steigmeyer, P. Gabrielli, Hernandez, R.S., B. Delmonte, Baccolo, G., Pratt, K., and May, N., *In Preparation*. Dust aerosol composition changes in East Antarctic during Glacial-Interglacial transition. Quaternary Science Reviews, **(Chapter 4)**.

1.10. References

Aarons, S.M., Aciego, S.M., Gabrielli, P., Delmonte, B., Koornneef, J.M., Wegner, A., Blakowski, M.A., In Press. The impact of glacier retreat from the Ross Sea on local climate: characterization of mineral dust in the Taylor Dome ice core, East Antarctica. Earth and Planetary Science Letters.
Aarons, S.M., Aciego, S.M., Gabrielli, P., Delmonte, B., Koornneef, J.M., Wegner, A., Blakowski, M.A., Bouman, C., in preparation. Ice core evidence for variable dust sources in the western United States over the last 300 years. Chemical Geology.
Aarons, S.M., Aciego, S.M., Gleason, J.D., 2013. Variable Hf-Sr-Nd radiogenic isotopic compositions in a Saharan dust storm over the Atlantic: Implications for dust flux to oceans, ice sheets and the terrestrial biosphere. Chemical Geology 349-350, 18-26.
Aciego, S.M., Cuffey, K.M., Kavanaugh, J.L., Morse, D.L., Severinghaus, J.P., 2007. Pleistocene ice and paleo-strain rates at Taylor Glacier, Antarctica. Quaternary Research 68, 303-313.
Basile, I., Grousset, F.E., Revel, M., Petit, J.R., Biscaye, P.E., Barkov, N.I., 1997. Patagonian origin of glacial dust deposited in East Antarctica (Vostok and Dome C) during glacial stages 2, 4 and 6. Earth and Planetary Science Letters 146, 573-589.
Biscaye, P., Grousset, F., Revel, M., Van der Gaast, S., Zielinski, G., Vaars, A., Kukla, G., 1997. Asian provenance of glacial dust (stage 2) in the Greenland Ice Sheet project 2 ice core, Summit, Greenland. Journal of Geophysical Research 102, 765-781.
Biscaye, P.E., 1971. The rubidium, strontium, strontium-isotope system in deep-sea sediments: Argentine basin. Journal of Geophysical Research 76, 5087-5095.
Blum, J.D., Erel, Y., 1997. Rb-Sr isotope systematics of a granitic soil chronosequence: The importance of biotite weathering. Geochimica Et Cosmochimica Acta 61, 3193-3204.
Bory, A.J.-M., Biscaye, P.E., Grousset, F.E., 2003a. Two distinct seasonal Asian source regions for mineral dust deposited in Greenland (NorthGRIP). Geophysical Research Letters 30.
Bory, A.J.-M., Biscaye, P.E., Piotrowski, A.M., Steffensen, J.P., 2003b. Regional variability of ice core dust composition and provenance in Greenland. Geochemistry Geophysics Geosystems 4.
Chen, J., Li, G.J., Yang, J.D., Rao, W.B., Lu, H.Y., Balsam, W., Sun, Y.B., Ji, J.F., 2007. Nd and Sr isotopic characteristics of Chinese deserts: Implications for the provenances of Asian dust. Geochimica Et Cosmochimica Acta 71, 3904-3914.
Dasch, E.J., 1969. STRONTIUM ISOTOPES IN WEATHERING PROFILES, DEEP-SEA SEDIMENTS, AND SEDIMENTARY ROCKS. Geochimica Et Cosmochimica Acta 33, 1521-1552.
Delmonte, B., Andersson, P., Hansson, M., Schoberg, H., Petit, J.-R., Basile-Doelsch, I., Maggi, V., 2008. Aeolian dust in East Antarctica (EPICA - Dome C

and Vostok): Provenance during glacial ages over the last 800 kyr. Geophysical Research Letters 35.
Delmonte, B., Baroni, C., Andersson, P.S., Schoberg, H., Hansson, M., Aciego, S., Petit, J.R., Albani, S., Mazzola, C., Maggi, V., Frezzotti, M., 2010. Aeolian dust in the Talos Dome ice core (East Antarctica, Pacific/Ross Sea sector): Victoria Land versus remote sources over the last two climate cycles. Journal of Quaternary Science 25, 1327-1337.
Delmonte, B., Basile-Doelsch, I., Petit, J., Maggi, V., Revel-Rolland, M., Michard, A., Jagoutz, E., Grousset, F., 2004a. Comparing the EPICA and Vostok dust records during the last 220,000 years: stratigraphical correlation and provenance in glacial periods. Earth-Science Reviews 66, 63-87.
Delmonte, B., Petit, J.R., Andersen, K.K., Basile-Doelsch, I., Maggi, V., Ya Lipenkov, V., 2004b. Dust size evidence for opposite regional atmospheric circulation changes over east Antarctica during the last climatic transition. Climate Dynamics 23, 427-438.
Delmonte, B., Petit, J.R., Basile-Doelsch, I., Jagoutz, E., Maggi, V., 2007. Late quaternary interglacials in East Antarctica from ice-core dust records. Developments in Quaternary Sciences 7, 53-73.
Fischer, H., et al., 2007. Glacial/Interglacial Changes in Mineral Dust and Sea-Salt Records in Polar Ice Cores: Sources, Transport, and Deposition. Reviews of Geophysics 45, 1-26.
Gabrielli, P., et al., 2010. A major glacial-interglacial change in aeolian dust composition inferred from Rare Earth Elements in Antarctic ice. Quaternary Science Reviews 29, 265-273.
Gaiero, D.M., 2007. Dust provenance in Antarctic ice during glacial periods: from where in southern South America? Geophysical Research Letters 34.
Goldstein, S.J., Jacobsen, S.B., 1987. The Nd and Sr isotopic systematics of river-water dissolved material: implications for the sources of Nd and Sr in seawater. Chemical Geology 66, 221-236.
Griffin, D., Kellogg, C., Shinn, E.A., 2001. Dust in the Wind: Long Range Transport of Dust in the Atmosphere and Its Implications for Global Public and Ecosystem Health. Global Change and Human Health 2, 20-33.
Grousset, F.E., Biscaye, P.E., 2005. Tracing dust sources and transport patterns using Sr, Nd and Pb isotopes. Chemical Geology 222, 149-167.
Grousset, F.E., Biscaye, P.E., Revel, M., Petit, J.-R., Pye, K., Joussaume, S., Jouzel, J., 1992. Antarctic (Dome C) ice-core dust at 18 k.y. B.P.: Isotopic constraints on origins. Earth and Planetary Science Letters 111, 175-182.
Hammer, C., Clausen, H., Dansgaard, W., Neftel, A., Kristinsdottir, P., Johnson, E., 1985. Continuous impurity analysis along the Dye-3 deep core. Geophys. Monog. Series. 33, 90-94.
Harrison, S.P., Kohfeld, K.E., Roelandt, C., Claquin, T., 2001. The role of dust in climate changes today, at the last glacial maximum and in the future. Earth-Science Reviews 54, 43-80.
Hinkley, T.K., 2001. Atmospheric regime of dust and salt through 75,000 years of Taylor Dome ice core: Refinement by measurement of major, minor, and trace metal suites. Journal of Geophysical Research 106.

Jacobsen, S.B., Wasserberg, G.J., 1980. Sm-Nd Isotopic Evolution of Chondrites. Earth and Planetary Science Letters 50, 139-155.
Jickells, T.D., An, Z.S., Andersen, K.K., Baker, A.R., Bergametti, G., Brooks, N., Cao, J.J., Boyd, P.W., Duce, R.A., Hunter, K.A., Kawahata, H., Kubilay, N., laRoche, J., Liss, P.S., Mahowald, N., Prospero, J.M., Ridgwell, A.J., Tegen, I., Torres, R., 2005. Global Iron Connections Between Desert Dust, Ocean Biogeochemistry, and Climate. Science 308, 67-71.
Jouzel, J., Alley, R., Cuffey, K., Dansgaard, W., Grootes, P., Hoffmann, G., Johnsen, S., Koster, R., Peel, D., Shuman, C., Stievenard, M., Stuiver, M., White, J., 1997. Vaildity of the temperature reconstruction from water isotopes in ice cores. Journal of Geophysical Research: Oceans 102, 26471-26487.
Kohfeld, K., Harrison, S., 2001. DIRTMAP: the geological record of dust. Earth-Science Reviews 54, 81-114.
Lambert, F., Delmonte, B., Petit, J.R., Bigler, M., Kaufmann, P.R., Hutterli, M.A., Stocker, T.F., Ruth, U., Steffensen, J.P., Maggi, V., 2008. Dust-climate couplings over the past 800,000 years from the EPICA Dome C ice core. Nature 452, 616-619.
Maher, B.A., Prospero, J.M., Mackie, D., Gaiero, D.M., Hesse, P.P., Balkanski, Y., 2010. Global connections between aeolian dust, climate and ocean biogeochemistry at the present day and at the last glacial maximum. Earth-Science Reviews 99, 61-97.
Mahowald, N.M., Baker, A.R., Bergametti, G., Brooks, N., Duce, R.A., Jickells, T.D., Kubilay, N., Prospero, J.M., Tegen, I., 2005. Atmospheric global dust cycle and iron inputs to the ocean. Global Biogeochemical Cycles 19.
Martin, J.H., 1990. Glacial-interglacial CO2 change: The Iron Hypothesis. Paleoceanography 5, 1-13.
McConnell, J., Lamorey, G., Hutterli, M., 2002. A 250-year high-resolution record of Pb flux and crustal enrichment in central Greenland. Geophysical Research Letters 29.
McTainsh, G., Strong, C., 2007. The role of aeolian dust in ecosystems. Geomorphology 89, 39-54.
McTainsh, G.H., 1984. The nature and origin of the aeolian mantles of central northern Nigeria. Geoderma 33, 13-37.
Morse, D.L., Waddington, E.D., Steig, E.J., 1998. Ice age storm trajectories inferred from radar stratigraphy at Taylor Dome, Antarctica. Geophysical Research Letters 25, 3383-3386.
Okin, G.S., Mahowald, N., Chadwich, O.A., Artaxo, P., 2004. Impact of desert dust on the biogeochemistry of phosphorus in terrestrial ecosystems. Global Biogeochemical Cycles 18.
Petit, J.R., Briat, M., Royer, A., 1981. Ice age aerosol content from East Antarctic ice core samples and past wind strength. Nature 293, 391-394.
Petit, J.R., Jouzel, J., Raynaud, D., Barkov, N.I., Barnola, J.-M., Basile, I., Bender, M., Chappellaz, J., Davis, M., Delaygue, G., Delmotte, M., Kotlyakov, V.M., Legrand, M., Lipenkov, V.Y., Lorius, C., Pepin, L., Ritz, C., Saltzman, E., Stievenard, M., 1999. Climate and atmospheric history of the past 420,000 years from the Vostok ice core, Antarctica. Nature 399, 429-436.

Rao, W.B., Yang, B., Chen, J.D., Lu, J., 2006. Sr-Nd isotope geochemistry of eolian dust of the arid-semiarid areas in China: Implications for loess provenance and monsoon evolution. Chinese Science Bulletin 51, 1401-1412.
Reeh, N., Oerter, H., Letreguilly, A., Miller, H., Hubberten, H.-W., 1991. A new, detailed ice-age oxygen-18 record from the ice-sheet margin in central West Greenland. Global and Planetary Change 4, 373-383.
Reheis, M.C., Budahn, J.R., Lamothe, P.J., Reynolds, R.L., 2009. Compositions of modern dust and surface sediments in the Desert Southwest, United States. Journal of Geophysical Research 114.
Reheis, M.C., Goodmacher, J.C., Harden, J.W., McFadden, L.D., Rockwell, T.K., Shroba, R.R., Sowers, J.M., Taylor, E.M., 1995. Quaternary soils and dust deposition in southern Nevada and California. Geological Society of Amerrica Bulletin 107, 1003-1022.
Revel-Rolland, M., De Deckker, P., Delmonte, B., Hesse, P., Magee, J., Basile-Doelsch, I., Grousset, F., Bosch, D., 2006. Eastern Australia: a possible source of dust in East Antarctica interglacial ice. Earth and Planetary Science Letters 249, 1-13.
Reynolds, R., Belnap, J., Reheis, M., Lamothe, P., Luiszer, F., 2001. Aeolian dust in Colorado Plateau soils: Nutrient inputs and recent change in source. Proceedings of the National Academy of Sciences of the United States of America 98, 7123-7127.
Rothlisberger, R., Mulvaney, R., Wolff, E.W., Hutterli, M.A., Bigler, M., Sommer, S., Jouzel, J., 2002. Dust and sea salt variability in central East Antarctica (Dome C) over he last 45 kyrs and its implications for southern high-latitude climate. Geophysical Research Letters 29.
Severinghaus, J.P., Brook, E.J., 1999. Abrupt Climate Change at the End of the Last Glacial Period Inferred from Trapped Air in Polar Ice. Science 286, 930-934.
Shao, Y., Wrywoll, K.-H., Chappell, A., Huang, J., Lin, Z., McTainsh, G.H., Mikami, M., Tanaka, T.Y., Wang, X., Yoon, S., 2011. Dust cycle: An emerging core theme in Earth system science. Aeolian Research 2, 181-204.
Taylor, S.R., McLennan, S.M., 1985. The continental crust: its composition and evolution. Blackwell Scientific.
Tegen, I., Lacis, A.A., Fung, I., 1996. The influence on climate forcing of mineral aerosols from disturbed soils. Nature 380, 419-422.
Thevenon, F., Anselmetti, F., Bernasconi, S., Schwikowski, M., 2009. Mineral dust and elemental black carbon records from an Alpine ice core (Colle Gnifetti glacier) over the last millennium. Journal of Geophysical Research-Atmospheres 114.
Thompson, L., Davis, M., Mosley-Thompson, E., Sowers, T., Henderson, K., Zagorodnov, V., Lin, P., Mikhalenko, V., Campen, R., Bolzan, J., Cole-Dai, J., Francou, B., 1998. A 25,000-year tropical climate history from Bolivian ice cores. Science 282, 1858-1864.
Thompson, L., Yao, T., Mosley-Thompson, E., Davis, M., Henderson, K., Lin, P., 2000. A high-resolution millennial record of the South Asian Monsoon from Himalayan ice cores. Science 289, 1916-1919.

Tsoar, H., Pye, K., 1987. Dust transport and the question of desert loess formation. Sedimentology 34, 139-154.
Wegner, A., Gabrielli, P., Wilhelms-Dick, D., Ruth, U., Kriews, M., De Deckker, P., Barbante, C., Cozzi, G., Delmonte, B., Fischer, H., 2012. Change in dust variability in the Atlantic sector of Antarctica at the end of the last deglaciation. Climate of the Past 8, 135-147.
Wolff, E.W., et al., 2006. Southern Ocean sea ice, DMS production and iron flux over the last eight glacial cycles. Nature 440, 491-496.
Yokoo, Y., Nakano, T., Nishikawa, M., Quan, H., 2004. Mineralogical variation of Sr-Nd isotopic and elemental compositions in loess and desert sand from the central Loess Plateau in China as a provenance tracer of wet and dry deposition in the northwestern Pacific. Chemical Geology 204, 45-62.
Zhang, Q., Kang, S., Kaspari, S., Li, C., Qin, D., Mayewski, P., Hou, S., 2009. Rare earth elements in an ice core from Mt. Everest: Seasonal variations and potential sources. Atmospheric Research 94, 300-312.

CHAPTER II

Ice core record of dust sources in the western United States over the last 300 years

Official citation:
Aarons, S.M., Aciego, S.M., Gabrielli, P., Delmonte, B., Koornneef, J.M., Uglietti, C., Wegner, A., Blakowski, M.A., Bouman, C., *In Preparation*. Ice core evidence for variable dust sources in the western United States over the last 300 years. Chemical Geology.

Abstract

Over the past ~5000 years, amplified dust generation and deposition in the American West has been linked to human activity. Intensified rates of agriculture and livestock grazing in recent decades have been correlated with greater dust production and deposition, detected on seasonal to annual timescales. We apply high-precision geochemical techniques to an ice core from the Upper Fremont Glacier (Wyoming, USA) to produce the first glacial dataset from the American West to serve as a survey of dust through the past 270 years. Our results demonstrate the evolving dust provenance to the Upper Fremont Glacier (UFG) from a long-range transport of mineral dust to a local source. The increased dust availability, transport, and flux response in the UFG ice core record supports satellite and sediment core data regarding the effects of anthropogenic activity upon dust sources and pathways in the American West, most notably in the rising dust input of particles smaller than 2.5 μm.

2.1. Introduction

2.1.1. Background and Motivation

Ice cores provide a continuous record of climate history and can capture a longer time period than modern, in-situ measurements and unlike lake sediments, ice cores are not contaminated with local sedimentary input derived from rivers (i.e. lake sediment studies). Midlatitude alpine glaciers are regional archives of climate providing insight into paleoclimate and paleoenvironmental conditions, as well as the high accumulation rates preserve anthropogenic pollutant input at high temporal resolution (Schuster et al., 2002; Thompson et al., 1998). Physical measurements of impurities (such as mineral dust) in the ice can provide insight into the regional and global climate conditions through time (Delmonte et al., 2004a; Fischer et al., 2007; Wolff, 2006). In addition to particle size distribution, determining the sources and transport pathways of dust involves detailed studies of the mineralogy, elemental compositions, and radiogenic isotopic composition of dust entrained within ice and potential source areas (PSAs) (Delmonte et al., 2004a; Lupker et al., 2010; Thevenon et al., 2009). Here, we attempt to isolate the contributions of different sources of dust deposited on the midlatitude Upper Fremont Glacier (Figure 2.1) in North America during the time period of 1720 A.D. to 1974 A.D. to document changes in the dust cycle throughout the increasing agricultural and industrial activity in the American West.

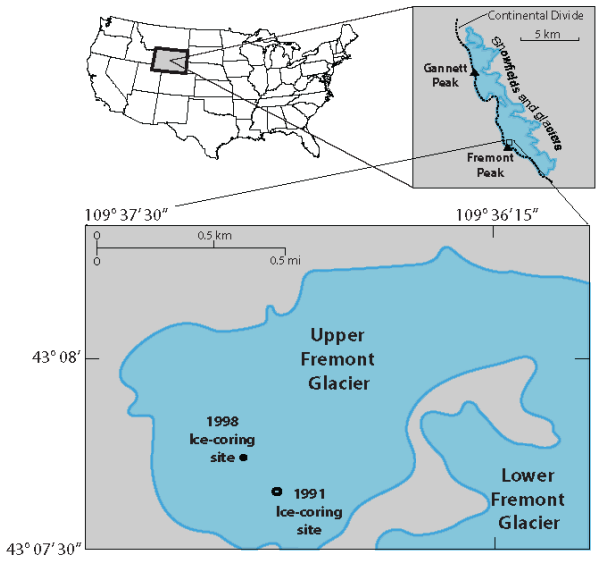

Figure 2.1. Upper Fremont Glacier (UFG) location map with 1998 and 1991 coring sites. The 1998 ice coring site (samples measured in this study) depicted by black circle. Ice coring site is located within the Wind River Range, WY, east of the continental divide.

Dust deposition can impact terrestrial ecosystems by: (1) contributing to phosphorus deposition in the western US, leading to eutrophication of inland waters (Ballantyne et al., 2011), (2) altering the energy balance in montane environments by accelerating melting rates of snow packs and alpine glaciers, and (3) shifting regional hydrological cycles due to earlier melting (Painter et al., 2007). Because the impacts of dust on ecosystems depends on the chemical compositions and thus source of the dust, understanding the dust sources and pathways in the American West is important to determine how both ecosystems and surface energy mass balance has evolved throughout time.

2.1.1.1 Global versus local inputs of dust

Dust fluxes are derived from both global (thousands of kilometers from the sink) and regional (tens to hundreds of kilometers) sources. Global sources (e.g. large deserts) are large areas up to millions of square kilometers in area, generally

arid, and have an abundance of small particles and are windy. The amount and impact of regional 'local' dust is location-dependent and, in general, is believed to be less than the global contribution, although this belief is not well quantified. Modern global dust emissions and corresponding source areas are observable via satellite (Prospero et al., 2002); major dust sources are the largest northern hemisphere deserts (North Africa, Middle East, and the high deserts of Asia). Dust is carried out of Asia eastward, with dust storm peaks in the spring (Prospero et al., 2002 and references therein). Distinguishing between global and regional local dust is important due to ongoing land-use and climate change that will likely have a larger impact on local versus global dust transport and deposition. That is, increasing agriculture or aridity due to land-use or climate change may create new sources of local dust without having a huge impact on well-characterized global dust sources (e.g. the Sahara, Gobi and Atacama deserts).

Shifts in average particle diameters can distinguish local from global dust. Far-traveled dust is typically <10 μm due to the effects of gravitational settling, and regionally sourced dust is typically >10 μm (Figure 2.2) (Delmonte et al., 2004a; Mahowald et al., 2005). The lifetime of dust particles in the atmosphere is dependent on particle size, ranging from a few hours for particles larger than 10 μm, up to several weeks for submicrometer-sized particles (Mahowald et al., 2005). The threshold friction velocity, or the friction velocity a particle must pass before movement via saltation, increases with grain size due to gravity, but also

increases for smaller particles due to particle cohesion, which results in an optimum particle size of ~60-80 μm at which the threshold friction velocity is at a minimum (Mahowald et al., 2005). Dust particles with sizes of ~70 μm are picked up most easily by winds, however, the dust transported thousands of kilometers has a modal diameter of ~2 μm (Mahowald et al., 2005; Schulz et al., 1998). Although long-range transported dust is typically small, larger dust particles (>100 μm) have been recorded to travel long distances to remote oceanic regions (Betzer et al., 1988). Increases in dust concentration and average particle diameter may result from land use changes (Figure 2.3), increased drought frequency, and higher than average wind speed, all of which culminate in greater dust emission and deposition (Ballantyne et al., 2011; Belnap and Gillette, 1997; Neff et al., 2008; Reheis and Urban, 2011).

To address the issue of increasing dust deposition related to anthropogenic activity in the western United States, several studies utilize dust particles in lake sediment cores and mountain snowpack (Brahney et al., 2014; Brahney et al., 2013; Doebbert et al., 2014; Neff et al., 2008). Dust particles in lake sediment cores are operationally defined as up to 65 μm in diameter, while dust in ice cores is generally smaller (Brahney et al., 2014; Brahney et al., 2013; Doebbert et al., 2014; Neff et al., 2008). The primary method of distinguishing between long range transported dust to a locally derived source is particle size distribution. Neff et al. (2008) defined a 37-63 μm grain size fraction as eolian derived and the >250 μm as locally eroded bedrock. Additionally, Neff et al.

(2008), measured particle-size distribution for modern dust for 5 different dust deposition events, with the results showing that 40% of dust collected occurs in the 10-37 μm class, 26% in the 37-63 μm class, and 17% in the 63-180 μm class. The authors speculated that the relatively large proportion of particles greater than 37 μm is evidence for particles that have been transported hundreds rather than thousands of kilometers (Middleton et al., 2001; Neff et al., 2008). Similarly, Ballantyne et al. (2011) studied lake sediments in two size classes: 37-60 μm and >250 μm. The smaller size class most closely resembled the particle size distribution of eolian dust, whereas the larger size class was most likely locally derived sediment (Ballantyne et al., 2011). In order to discern changes in finer dust particles from regional sources (>10 μm) versus globally sourced dust (<10 μm), we utilize the Upper Fremont Glacier ice core as a paleoclimate record that is relatively pristine and does not contain riverine sediment input.

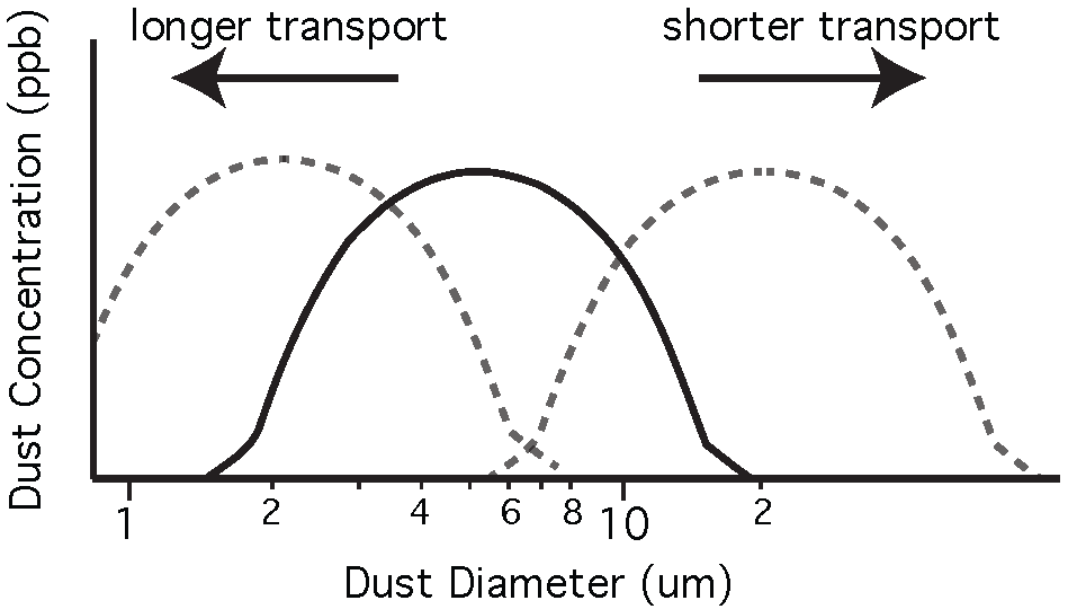

Figure 2.2. Schematic of dust particle size distribution as an indicator of transport distance. Note that smaller (larger) dust particle diameters are indicative of longer (shorter) transport distance.

Regionally, the largest modern, documented dust sources in North America lie between the Sierra Nevada Mountains to the west, and the Rocky Mountains to the east (Prospero et al., 2002). There is seasonal variability in the export of dust from these regions, with dust transport generally highest from April through September. Human activity has variable impact in dust sources over time (Grayson, 1993; Reheis, 1997), and the number and magnitude of dust sources in the American West region has increased as a result of anthropogenic activities. While the Great Plains was a significant dust source during the 'Dust Bowl,' modern observations do not show this region as a significant dust emitter compared to natural or other human-caused sources of dust in North America (Prospero et al., 2002).

2.1.1.2. Anthropogenic influence on dust cycle

In areas with low precipitation rates, agriculture and livestock grazing disturb soils and vegetation, leaving soils more susceptible to wind erosion during drought periods (Prospero and Lamb, 2003). Increased human activity (i.e. agriculture and livestock grazing) in the American southwest and the Colorado Plateau during the past several decades has been correlated with greater dust production and deposition, which has been detected on mountain snow cover on seasonal to annual timescales (Neff et al., 2008; Painter et al., 2007; Reynolds et al., 2001). We would expect to observe higher concentrations of larger dust particles (>10 μm in diameter) in the ice core record as agriculture and livestock

grazing increases due to amplified dust generation and availability for transport. On longer timescales, the magnified impact of evolving agricultural practices (industrialization, soil conservation and increased cultivation area) on the dust cycle across North America has not yet been explored using ice core records. Land use dramatically changed from the time of initial European exploration, immigration, and agricultural cultivation as waves of immigrants settled the Great Plains and the American southwest (California, Nevada and Arizona). From the 1700s to the present, the expanse of cultivated cropland across the US has increased by several orders of magnitude (Figure 2.3). Soil conservation efforts throughout the US following the Dust Bowl in the 1930s should result in a diminishing presence of large diameter dust particles in the ice core record, as coarser (sandy) particles are more susceptible to wind erosion than finer (silt and clay) particles (Lyles, 1985).

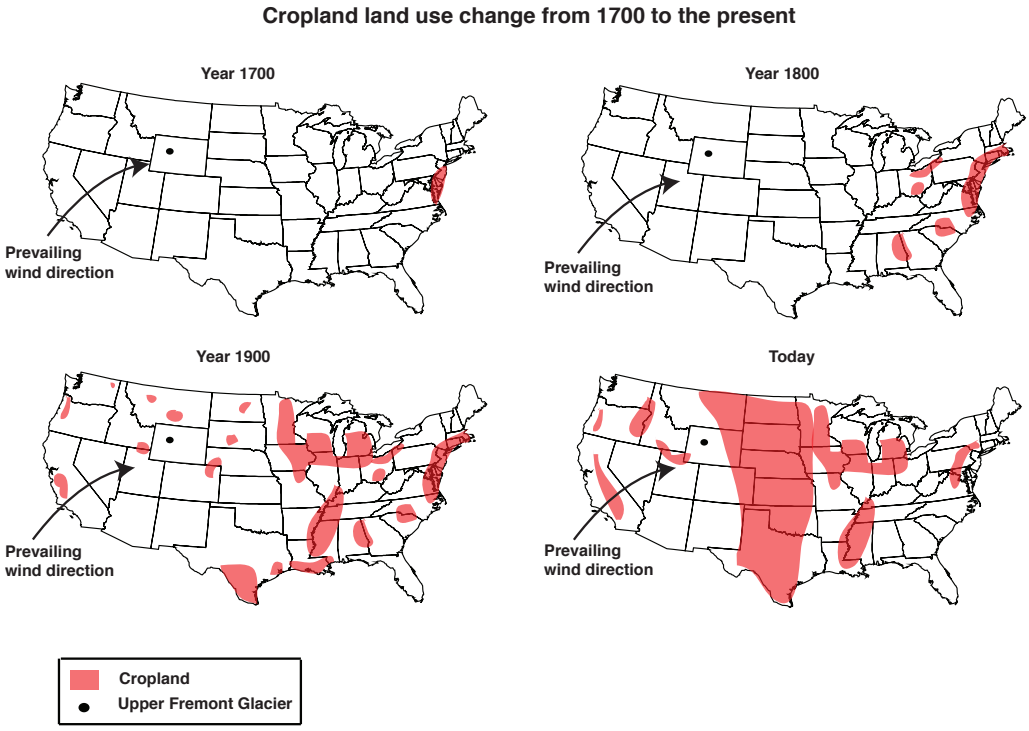

Figure 2.3. Historical land use maps for the United States during the time periods of 1700, 1800, 1900 and today (adapted from (Goldewijk, 2001)). Also shown are the prevailing wind direction and location of the Upper Fremont Glacier.

During the period of pre-Industrial and pre-expansion into the American West (1720-1820 A.D.), natural changes in dust concentration and size distribution should coincide with regional droughts. Dry, arid conditions lead to higher dust availability, which combined with a mechanism for transport (wind), will lead to dustier conditions. Larger dust particles (>10 μm) are likely regionally sourced dust, whereas smaller dust particles (<10 μm) are far traveled dust transported in the upper troposphere (Figure 2.2). During the Second Industrial Revolution (1860-1910 A.D.) and the westward expansion (~1869 A.D.), intensive grazing in certain parts of the West increased, and we would therefore expect to see increases in dust concentration and average dust particle diameter as the dust is

regionally source. During the Dust Bowl (~1930 A.D.), severe drought combined with little to no crop rotation would result in an increase of transportable dust. Dust deposited during the dust bowl has been observed in the Greenland ice core record (Donarummo Jr. et al., 2003), and should be in the diameter range of 1.2-4 μm, consistent with a soil-derived source (Patterson and Gillette, 1977). The droughts that affected North America during 1950 A.D. and the late 1980s A.D. combined with higher wind speeds during the spring would likely cause an increase in coarse-grained particles transported to sinks in close proximity (e.g. lakes, mountain glaciers). From 1970 A.D. onward, increased activity such as agriculture and livestock grazing in the American southwest and Colorado Plateau would result in greater dust production and a shift in dust provenance to these regions.

Recent work (Brahney et al., 2014; Brahney et al., 2013; Doebbert et al., 2014; Neff et al., 2008; Painter et al., 2007) has indicated that agriculture development and water diversion has resulted in larger, local dust emissions from the Colorado Plateau and Green River Basin. Because of the growing interest in using ice cores from alpine glaciers to reconstruct records of dust sources and deposition, we must also consider changes in rock exposure due to the advance or retreat of glaciers over time. For example, at the UFG site, fresh moraine or outwash material could be an increasing local source over time due to the retreat of the seven glaciers in the Wind River Range since the Little Ice Age (LIA).

These moraines are essentially devoid of vegetation; thus, if up-glacier winds are strong enough, they could pick up glacier flour particles from these moraines.

2.1.1.3 Satellite observations of dust transport

In tracking modern dust emissions and modeling transport for the purposes of determining air quality, dust source activations (DSAs) are well defined (Schepanski et al., 2007; Schepanski et al., 2009). However, in paleoclimate literature DSAs are not known but hypothesized, and are therefore referred to as potential source areas (PSAs) (Basile et al., 1997; Biscaye et al., 1997; Delmonte et al., 2010; Delmonte et al., 2004a; Mahowald et al., 1999). In order to narrow the possibilities of PSAs globally and regionally, we used the web-based version of the NOAA HYSPLIT model (HYbrid Single-Particle Lagrangian Integrated Trajectory Model, 1997, http://www.arl.noaa.gov/ready/hysplit4.html) to illustrate the range in isentropic backward air trajectories terminating at the ice core site on the UFG (Figure 2.4). Seven-day back trajectories were performed using known meteorological conditions for the second week in April, June, August, October, and December 1963, 1967 and 1974 A.D., respectively. Even with these fifteen model runs, it is apparent that air masses from all modern dust emission sources in North America can be transported to the UFG site. Because back trajectory models require meteorological conditions to run, it is not possible to determine trajectories during the time period of ice preservation (except for 1963, 1967, and 1974 A.D.), and so we use these for illustrative purposes to show monthly and annual variability.

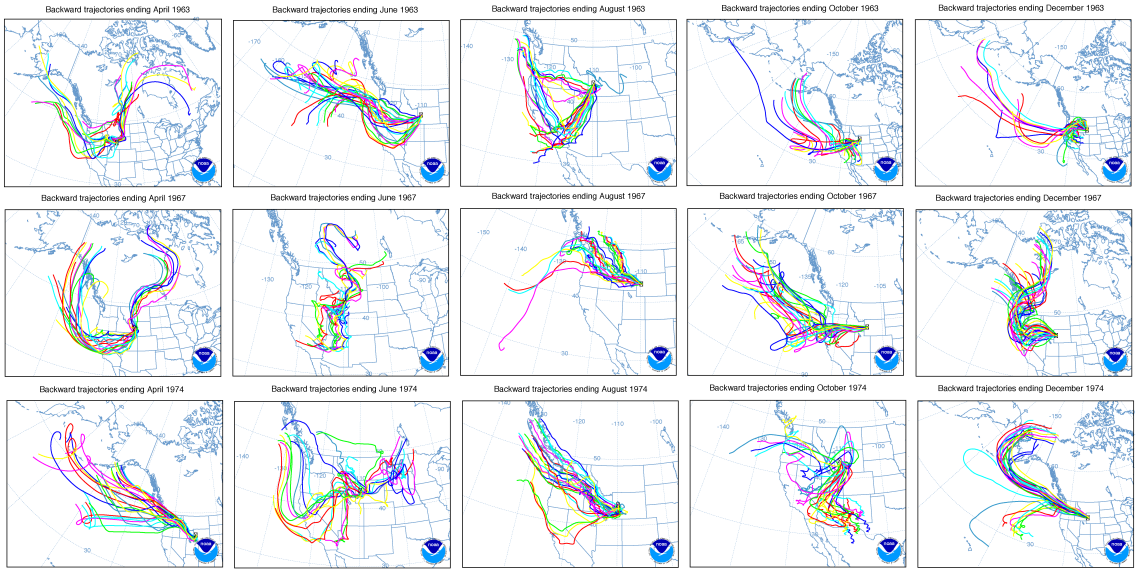

Figure 2.4. NOAA HYSPLIT air parcel backward trajectory model for UFG coring site. Back trajectory model at 4000 m elevation and meteorological conditions for April, June, August, and December 1963, 1967, and 1974 A.D. respectively (Draxler and Hess, 1998); these model conditions reveal backward trajectories from a wider sector of western North America, including CO, NM, and AZ, and western Arctic Alaska and Canada. Figure generated using NOAA Hybrid Single-Particle Lagrangian Integrated Trajectory (HYSPLIT) model, which computes air parcel trajectories to demonstrate dispersion and deposition pathways (Draxler and Hess, 1998).

2.1.2. Upper Fremont Glacier site description

The glaciers of the WRR experience generally lower solar radiation and predominantly westerly winds due to the easterly orientation (Fryxell, 1935). The average annual precipitation from 1971-2000 at the WRR is 1,143 mm/year (Curtis and Grimes, 2004), with the majority of precipitation occurring as snow during the winter. Wyoming has experienced both higher annual temperatures and precipitation on a decadal basis since 1966 (Curtis and Grimes, 2004), and reconstructed air temperatures from UFG ice core data indicate an increase in average air temperature of ~5^{o} C from the end of the LIA to the early 1990s (Naftz et al., 2002). Two ~160-m long ice cores were drilled in 1991 and 1998 at the UFG, providing the first successful reconstruction of paleoclimate from a south-central North American ice core (Naftz et al., 1996). These records include

stable oxygen isotopes in precipitation, nitrate and tritium concentrations, and carbon-14 concentration from grasshopper leg parts entrained in the ice, sulfate, chloride, and electrical conductivity measurements, and Hg concentrations (Naftz et al., 1996; Schuster et al., 2002; Schuster et al., 2000). Thus far, these records show the impact of warming climate and industrialization as the precipitation trends toward heavier oxygen isotopic values and higher atmospheric concentrations of Hg are observed over the time encompassed by the ice core. For this study, we used the UFG core drilled in 1998, as the 1991 UFG core was almost entirely consumed for previous work. The 1998 UFG core drilling location is within 200 m of the 1991 core, and encompasses the same time period; the age/depth relationship is slightly different between the two cores, but not systematically over the entire records. Uncertainty in the age scale is as high as 95 years at the base, and 10 years at the surface.

2.2. Materials and Methods

We analyzed 13 samples from the UFG ice core (FRE 98-4 ice core, 43°07’37’’ N, 109°36’54’’ W, 4000 m a.s.l.), located in the Wind River Range, Wyoming, USA (Figure 2.1). Ice core samples from the UFG were delivered from the National Ice Core Laboratory (NICL). The ice core samples measured during this study spanned a depth of ~158-70 meters below the surface. The ice core section was cut longitudinally into 3 subsamples: the outer portion for radiogenic isotopic composition measurement, another for dust concentration and size distribution measurements, and the last for TE concentration measurement.

Hereafter, the procedure for processing the radiogenic samples varied from the processing for the dust concentration and size distribution and TE samples using previously published methods (Koornneef et al., 2014).

2.2.1. Initial processing and decontamination of the UFG ice core

Each ice core sample was cut longitudinally into three subsamples, all of which were 40 cm long: the outer portion was reserved for radiogenic isotopic composition measurement (weighing approximately 314 g), along with one section for dust concentration and size distribution measurements (weighing approximately 73 g), and one for TE concentration measurement (weighing approximately 73 g). The latter two samples were split into three subsamples: a, b, and c (each weighing approximately 24 g), with subsample “a” being the portion of the core closest to the surface of the glacier. See Figure 2.5 for a schematic of the ice core cutting diagram. Tools for decontaminating and processing the ice core were made of PFA Teflon and acid washed prior to use; we used PFA Teflon chisels impregnated with quartz to scrape the outermost layer of the ice. All initial processing and chemistry was performed in a class 10,000 clean room, under class 100 laminar flow hoods.

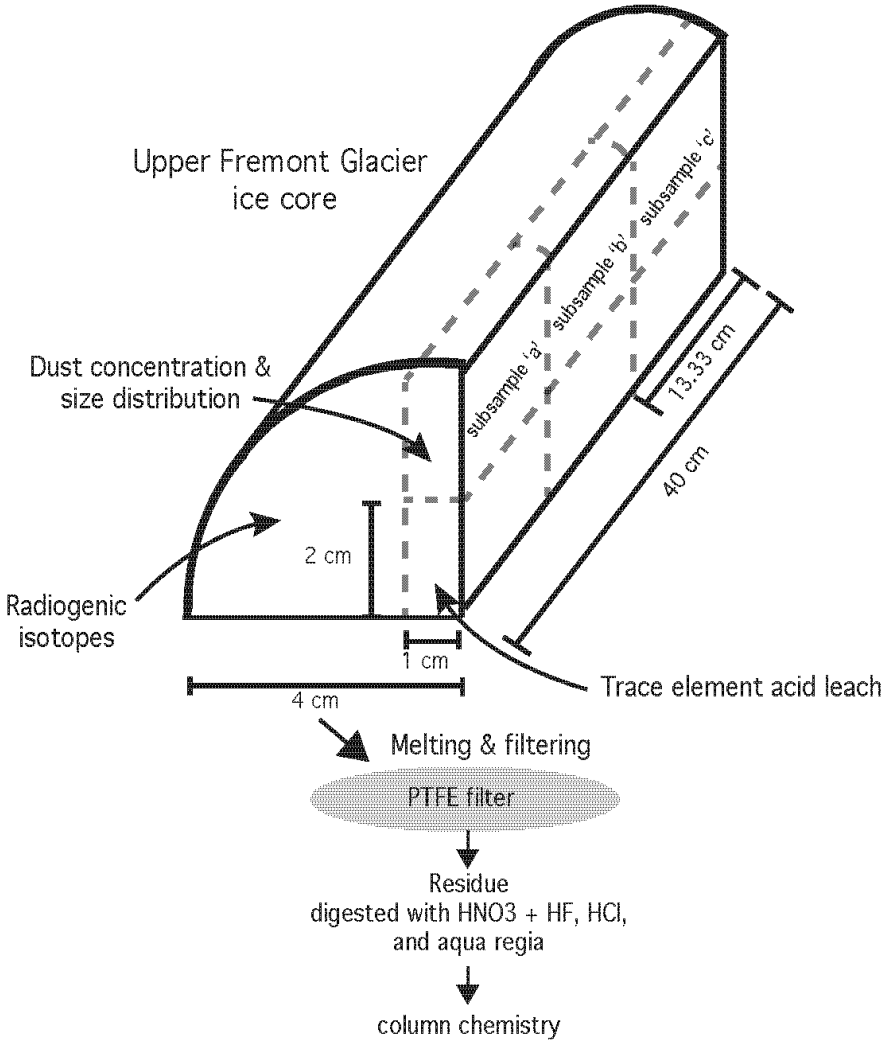

Figure 2.5. Schematic of ice core sample preparation. Samples are split for radiogenic isotope, dust concentration and size distribution, and rare earth and trace element analysis of UFG ice core.

2.2.2. Processing of the radiogenic isotope portion of the UFG ice core

Each ice core sample for the radiogenic portion was decontaminated using a three-step procedure. First, while the ice core sections were still cold (-25° C), the outer most 2 mm were scraped with the PFA chisels and then rinsed with distilled ethanol. After allowing the ice cores to warm up for ~10 min, the cores were again scraped another 1-2 mm with a new, clean PFA chisel, and rinsed with MilliQ water. The core sections were then melted while buffered to a neutral pH with ultra-pure ammonia, and the resulting liquid was immediately filtered

through 2 acid pre-cleaned 0.2 μm and 30 μm Teflon filters. The dust fraction was dissolved and digested off the filters for elemental separations using column chemistry procedures described in Lupker et al. (2010). Large Sr and Nd fractions of the dust in UFG ice were analyzed using a Thermo Scientific Triton PLUS Thermal Ionization Mass Spectrometer (TIMS) equipped with 10^{11} Ohm resistors at the University of Michigan, while the small Nd fractions were analyzed using a Thermo Scientific Triton PLUS TIMS equipped with 10^{13} Ohm resistors at VU Amsterdam using procedures described by Koornneef et al. (2014). All Sr isotopic compositions were normalized to $^{88}Sr/^{86}Sr=8.375209$ to correct for mass bias, and the Sr isotopic standard SRM987 (10 ng) was also measured at $^{87}Sr/^{86}Sr= 0.710269+/- 5$ (2σ SD, n=5) on the University of Michigan Thermo Scientific Triton PLUS. The USGS reference material BCR-2 (10 ng) measured at the same time as the samples averaged 0.705035 +/- 7 (2σ SD, n=1). Neodymium isotopic compositions were normalized to $^{146}Nd/^{144}Nd = 0.7219$ using the exponential law and mass 149 was monitored for Sm interference. The To ensure accuracy, Nd isotopic standard JNdi-1 (10 ng) was measured at $^{143}Nd/^{144}Nd=0.512102 +/- 22$ (2σ SD, n=4).

We measured two size fractions (fine filter: 0.2-30 μm, and coarse filter: 30-60 μm) of particulates collected from the filtered and buffered meltwater of 13 discrete samples from the 1998 UFG ice core for Sr and Nd isotopic composition. Next, we performed bulk analysis of dust concentration and size distribution and TE concentrations on three longitudinal subsamples for each primary sample to

assess short term (< 1 year) variability. Melted ice core samples were analyzed for dust concentration and size distribution by Coulter® Counter.

2.2.3. Processing of the trace element portion of the UFG ice core

Samples reserved for trace element concentration analysis were triple-rinsed with MilliQ water using acid-washed LDPE calipers, and melted in pre-cleaned LDPE Nalgene bottles following procedures established by Boutron et al. (1990). The melted samples were immediately acidified in 1% HNO3 (ultra-pure) and left to sit for approximately 1 month prior to analysis. Trace element concentrations were determined at The Ohio State University on a Thermo Element2 Inductively Coupled Plasma Sector Field Mass Spectrometer (ICP SFMS) coupled with a micro-flow nebulizer and a desolvation system (Apex Q). This system allows for TE detection down to the sub-pg g^{-1} levels (Uglietti et al., 2014). Low resolution (LR) mode was used for the detection of ^{85}Rb, ^{95}Mo, ^{109}Ag, ^{111}Cd, ^{120}Sn, ^{121}Sb, ^{205}Tl, ^{208}Pb, ^{209}Bi, and ^{238}U, medium resolution (MR) mode for ^{27}Al, ^{48}Ti, ^{51}V, ^{52}Cr, ^{55}Mn, ^{56}Fe, ^{59}Co, ^{63}Cu, and ^{64}Zn, and high resolution mode for ^{75}As.

2.2.4. Processing of the dust concentration and size distribution portion of the UFG ice core

The dust concentration and size distribution samples were triple rinsed with MilliQ water using acid pre-cleaned LDPE calipers and stored in triple rinsed PFTE centrifuge tubes frozen until just prior to analysis following the procedures described in Delmonte et al. (Delmonte et al., 2004a). For each dust concentration and size distribution subsample ~20 ml was available for Coulter®

Counter microparticle concentration and size distribution measurements in the range of 1.006-29.83 μm. Five consecutive measurements were performed on each sample to ensure the accuracy of the results. The reproducibility is very good for concentrated samples (typically <2% for 50,000 particles/g) whereas some scattering occurs with low concentration samples (~20% for 1000/g) (Delmonte et al., 2002). The blank levels were negligible.

2.2.5. Uncertainty in age scale between 1991 and 1998 UFG ice core

Two ice cores from the Upper Fremont Glacier were retrieved from two different sampling locations in 1991 and 1998 A.D., respectively (Figure 2.6). We apply the age scale of the 1991 core to the 1998 core for this study, as the 1998 core possesses oxygen isotope data only for the depths of 16 - 60 meters. Previous work (Schuster et al., 2002) utilized both the 1991 and 1998 ice cores to produce a single atmospheric mercury deposition record in North America from ~1720-1993 A.D. The continuity of the Hg record suggests that the chronology displacement of the records is sub decadal. Annual dust layers in the UFG are not always present, making visual layer counting as a method of age dating impossible. The chronology of the 1991 UFG was determined using chemical and isotopic age dating techniques. The 1963 tritium (Naftz et al., 1996) and 1958 chlorine-36 peaks (Cecil and Vogt, 1997; Naftz et al., 2002) were located at depths of 28 and 32 meters, respectively. A carbon-14 value obtained from a grasshopper leg entrained in ice at 152 meters yielded an age of 221 ± 95 years (Naftz et al., 1996). These dates, along with the estimated snow

accumulation and ablation values (Naftz, 1993), were used to establish a low-resolution age scale for the UFG cores.

Additional time markers for the ice cores were established at depths of 88 and 123 meters using electrical conductivity measurements, which improved the ice-core chronology to prediction limits of ± 10 years (90% confidence level) (Schuster et al., 2000). The lack of concrete chemical age-markers below the depth of 32 meters suggests that the age scale for the 1991 core possesses a potential error, which may be significant with increasing depth (Figure 2.7). This has implications for samples at higher depths, and highlights the necessity of accurately determining the 1998 UFG ice core age scale. The tritium peak in the 1998 ice core is ~1.5 meters deeper than the tritium peak in the 1991 ice core (Naftz et al., 2002), most likely due to additional snow deposited on the UFG between the 1991 and 1998 ice core retrievals and small-scale variations in snow accumulation and retention between the two sites. There is no evidence for overturning in ice and the upper 60 meters of the 1998 ice core are well dated. Although seasonal isotopic signatures should not be preserved, long-term trends in climate are visible, which is sufficient for describing changes in dust provenance over the time record.

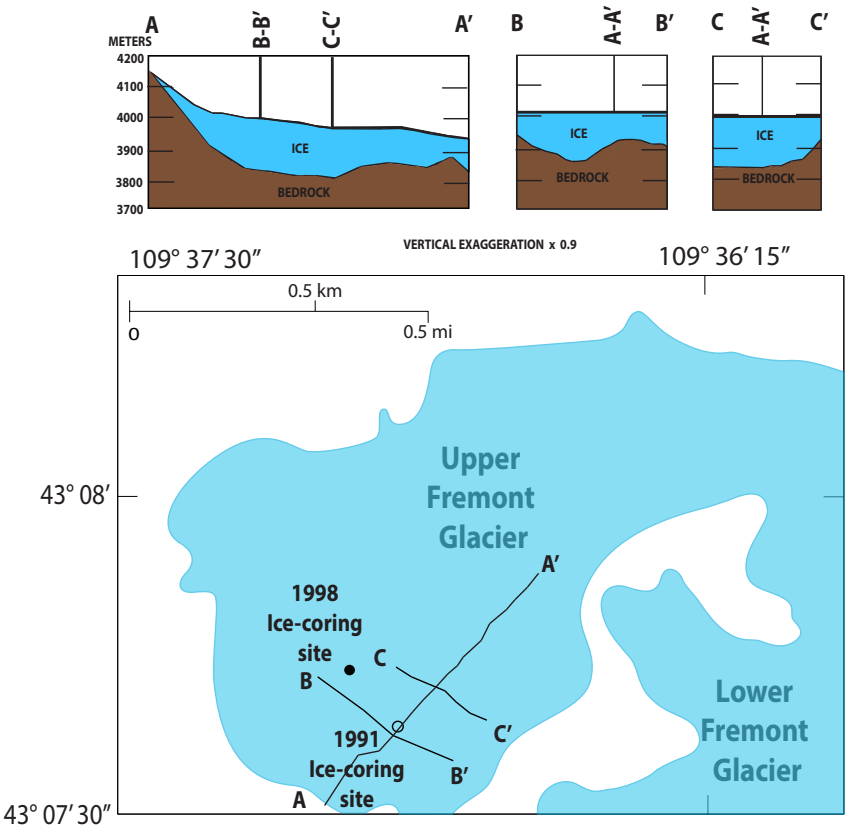

Figure 2.6. Ice thickness cross sections. Ice thickness along three transects on the Upper Fremont Glacier, Wyoming. Also shown are ice core locations in 1991 (open black circle) and 1998 (closed black circle) respectively (Figure adapted from Naftz et al. (1996).

The 1991 UFG ice core is ~160 m long with ~270 years of paleoclimate record, suggesting an average accumulation rate of more than 0.5 m/year. Based upon the accumulation rate and the possibility of ice thinning of the relatively shallow alpine glacier, the timescale difference between the 1991 and 1998 ice cores are likely sub-decadal. Each sample measured in this study was ~0.4 m in length, representing at least one year and even more at greater depths depending on the subsequent ice thinning. However, despite the possibility of a sub-decadal difference in age, the overall age scale should be similar enough for the purposes of investigating changes over 250 years.

In this work, we also incorporate the ice thickness of three transects of the UFG determined using radio-echo sounding (Figure 2.6). The two ice core locations from 1991 and 1998 are in close proximity to the transect B-B', demonstrating that the two ice cores retrieved are of similar thickness (~160 m), and are situated close to the accumulation area without any major bedrock anomalies that would result in a major disturbance to the age-scale relationship between the two ice cores (see transect A-A') (Figure 2.6). Chronological refinement on the age-depth relationship of the 1991 UFG ice core utilized volcanic events, and isotope and chemical data (Schuster et al., 2000). A best-fit polynomial line was fitted to this data and plotted (Figure 2.7), and the age equation (Schuster et al., 2000) is:

$$\text{Age in years: } 0.00738(D)^2 + 0.5558(D)$$

We applied this age-depth relationship equation to determine the approximate age of samples from the 1998 UFG ice core, and based upon the proximity of the two drilling locations, the maximum offset between the two ice core records should be less than 10 meters; according to the age equation, this maximum offset corresponds to ~6.3 years, or less than one decade. Conversely, a combination of ice core and snow pit data suggest that the average ice equivalent accumulation rate at the UFG is 0.7 m/year (Schuster et al., 2000). Thus, if we assume that that maximum depth offset between the two ice cores is 10 meters, and that the 1991 age scale equation is correct, then the age offset would be less than 14.3 years between the two ice cores, which is insignificant in terms of the interpretation discussed here.

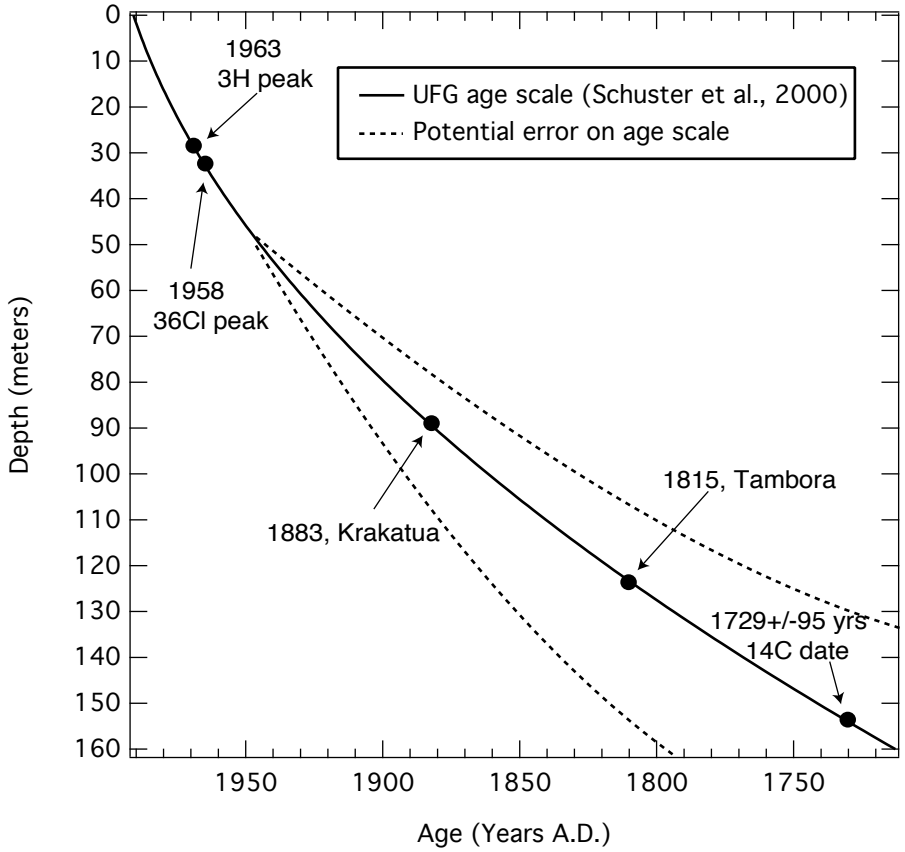

Figure 2.7. Age-depth profile. 1991 UFG ice core age and depth relationship based upon chemical and volcanic tie points. Solid black line represents the polynomial fit for the age-depth profile (Figure adapted from Schuster et al. (Schuster et al., 2000)), dashed black lines represent potential error of age-depth relationship.

2.3. Results and Discussion

2.3.1. Dust particle concentration and size distribution

Dust particle concentrations and size distributions are summarized in Figures 2.8, 2.9, and 2.10b, respectively. Average dust concentration increases from ~15 to 17 ppb from 1815 to 1974 A.D., indicating amplified dust availability and/or dust events during that time period (Figure 2.8) (Ballantyne et al., 2011; Belnap and Gillette, 1997; Delmonte et al., 2004a; Neff et al., 2008; Reheis and Urban, 2011). We observe the highest dust concentration (>1600 ppb) at an ice depth of ~120 meters below surface (~1815 A.D.), while the dust concentration is >1200 ppb at a depth of ~20 meters below surface (~1974 A.D.) (Figure 2.9, 2.10b). The large average dust particle diameter of 5 μm (Figure 2.8) associated with the

high dust concentration observed in ~1974 A.D. suggests that this dust could not be transported over large distances. Thus, we expect that this dust originated from a local dust event near the UFG. Spikes in dust concentration are in the >5 μm dust fraction (Figure 2.10b), and combined with the larger average size of dust recorded and analyzed in lacustrine systems (Ballantyne et al., 2011; Neff et al., 2008), this data highlights the relevance of evaluating dust size fractions up to 60 μm when investigating continental dust records. When comparing older (1815 A.D.) to younger (1974 A.D.) samples, the average diameter of dust particles increases from ~2 μm to 5 μm (Figure 2.8), suggesting either a shift to a closer dust source or increasing wind strength. The full record of dust particle size distribution with respect to dust concentration is shown in Figure 2.9, illustrating the variable physical dust composition over the time period of interest.

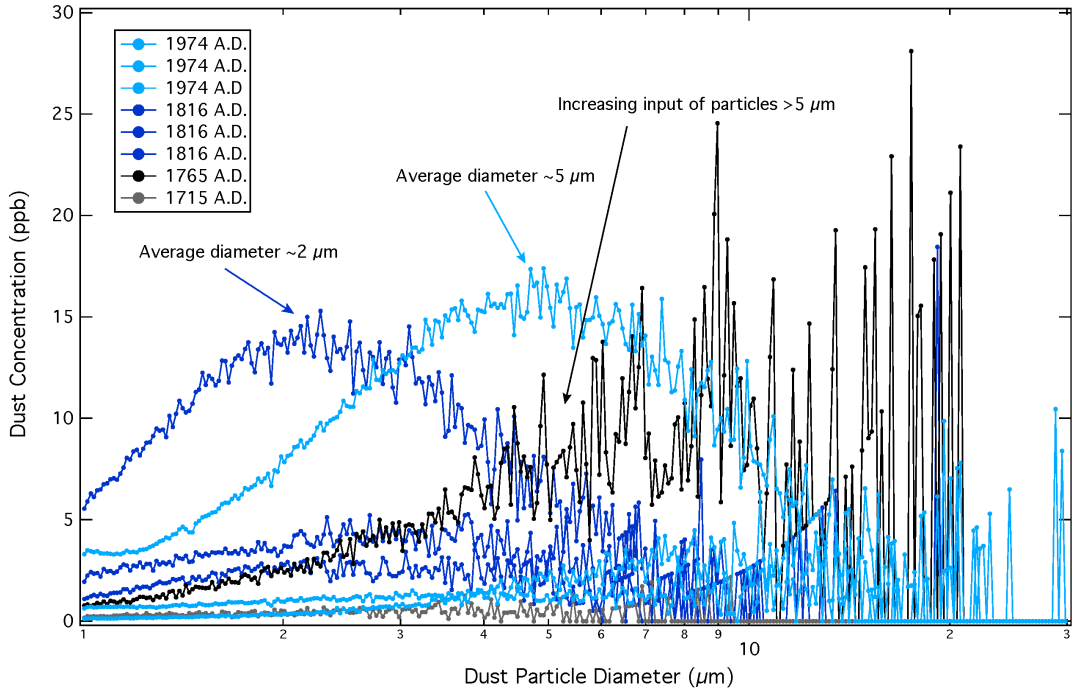

Figure 2.8. Dust particle size distribution of select samples of UFG ice core. Dust concentration (ppb) with respect to dust particle diameter (μm) for samples from time periods of 1715, 1765, 1815, and 1974 A.D.

2.3.2 Increasing input of $PM_{2.5}$

There is no clear trend in dust particle diameter size over time; however, several of the younger samples (1926, 1963, and 1967 AD) display distributions with the possibility of increasing input of particulate matter (PM) smaller than 2.5 μm ($PM_{2.5}$) (Figure 2.9). The majority of dust mass deposited during these time periods is in the larger dust diameter size (>4 μm), suggesting increased levels of local dust input (i.e. larger particle diameter size), though the small spikes in $PM_{2.5}$ are clearly visible in the dust particle size distributions (Figure 2.9). Primary production of fine and ultrafine PM are both natural and anthropogenic in origin, and sources of particulate pollution may be from factories, power plants, refuse incinerators, motor vehicles, construction activity, fires and windblown mineral dust (Kampa and Castanas, 2008). Fine particles less than 2.5 μm in diameter may be damaging to human health through inhalation and accumulation in the respiratory system (Kampa and Castanas, 2008). The increasing abundance of particles less than $PM_{2.5}$ (in this case the rising abundance of small PM is ~1.5 μm) could be attributed to an increase in anthropogenic pollutants.

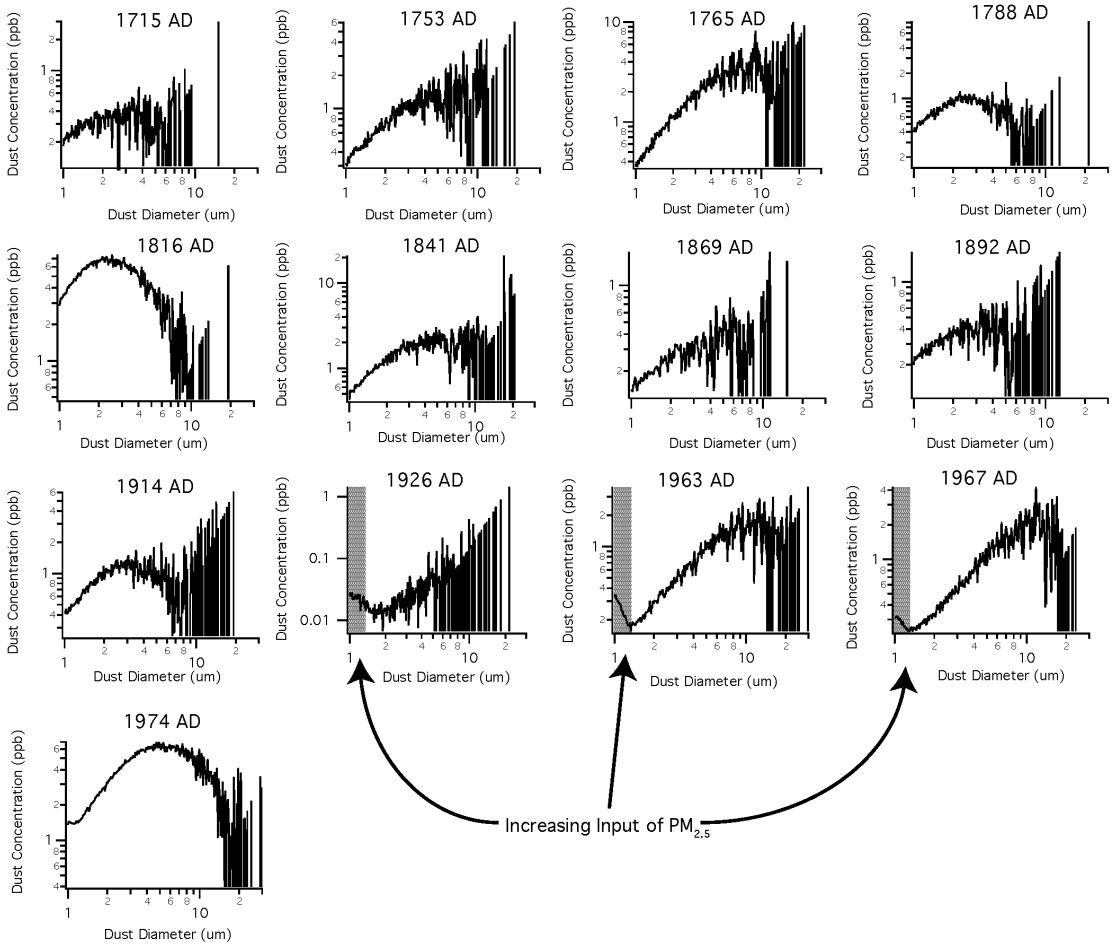

Figure 2.9. Dust particle size distribution. Dust concentration (ppb) with respect to dust particle diameter (μm) for all samples from Upper Fremont Glacier. Note the shaded area in samples 1926, 1963, and 1967 A.D. highlights the increasing input of particles less than 2.5 μm.

2.3.3. Trace element concentrations indicate anthropogenic influence

The crustal enrichment factor (EF) is defined here as the concentration ratio of a particular element relative to that of Al (which serves as an indicator for rock and soil dust) in the ice, normalized to the same concentration ratio found in the upper continental crust. For example, the EF for Pb is:

$$EF_c = ([Pb]_{ice}/[Al]_{ice})/ ([Pb]_{crust}/[Al]_{crust})$$

The trace metal (Cr, As, Cd, Pb, Cu, and Zn) EF is represented in Figure 2.10c, with a large portion of the samples displaying EFs greater than 100 (Cr was the

only trace metal with an EF measured at or below 4.6, see Table 2.1). Enrichment Factors close to one (or up to ~5) indicate the elements originate from rock and soil dust, and values significantly greater than one indicate a large contribution from another natural source (Gabrielli et al., 2005). The very high crustal EFs in the samples may be attributed to interactions of insoluble dust with anthropogenic emissions as dust particles can scavenge pollutants during atmospheric transport and subsequently deposit them in terrestrial or aquatic ecosystems or upon ice sheets and glaciers (Erel et al., 2006; Reheis et al., 2009). We observe the highest crustal EFs for Pb and Cd most notably during 1753, 1765, and 1926 A.D. Following the Clean Air Act of 1963, our observed crustal EFs are slightly lower, possibly a result of reduced air pollution emissions (Figure 2.10c, see Table 2.S1 for full trace element concentrations).

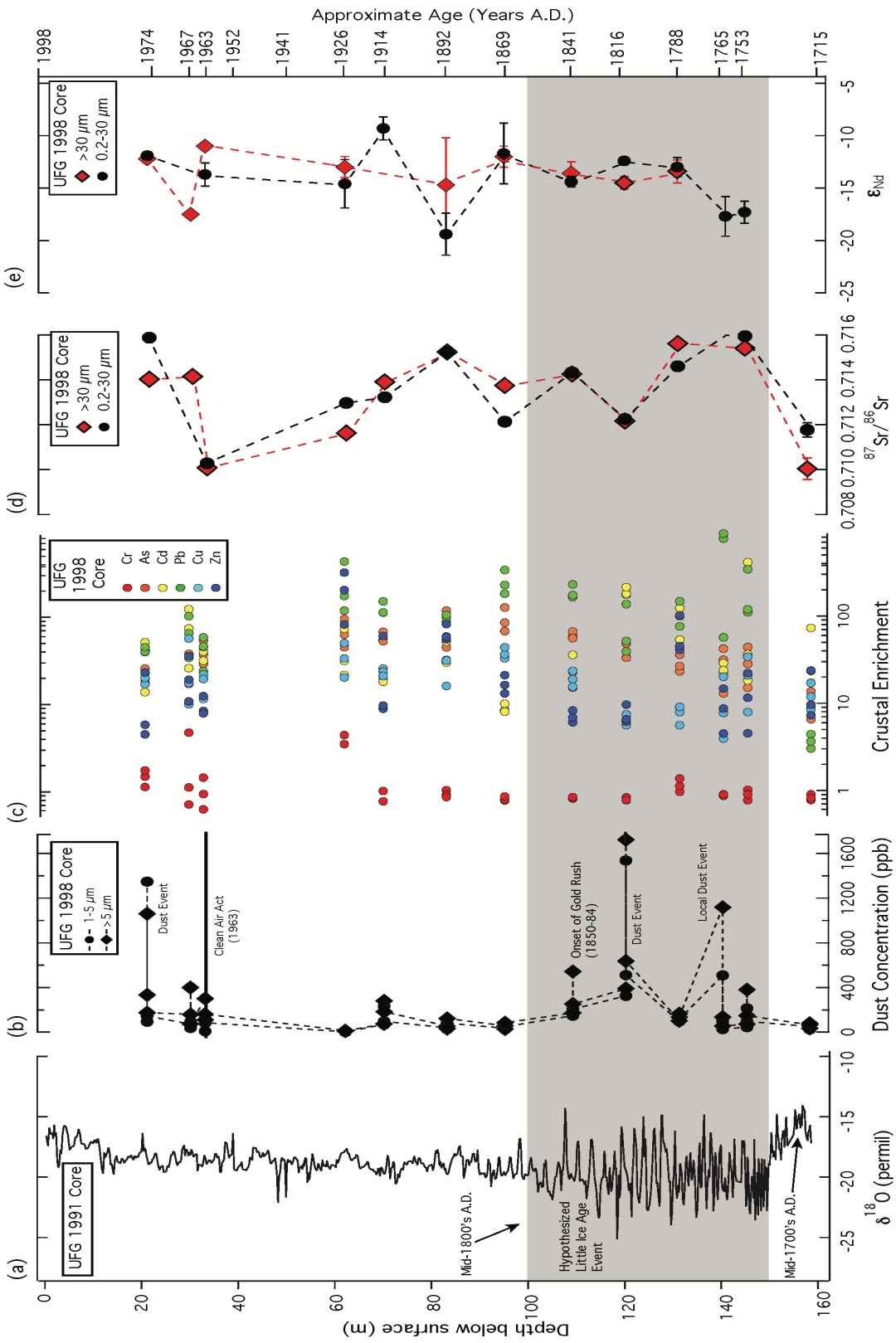
Approximate Age (Years A.D.)
1998
1974
1967
1963
1952
1941
1926
1914
1892
1869
1841
1816
1788
1765
1753
1715
(a)
UFG 1991 Core
Mid-1800's A.D.
Hypothesized Little Ice Age Event
Mid-1700's A.D.
Depth below surface (m)
δ18O (permil)
(b)
UFG 1998 Core
1-5 μm
>5 μm
Dust Event
Clean Air Act (1963)
Onset of Gold Rush (1850-84)
Dust Event
Local Dust Event
Dust Concentration (ppb)
(c)
UFG 1998 Core
Cr
As
Cd
Pb
Cu
Zn
Crustal Enrichment
(d)
UFG 1998 Core
>30 μm
0.2-30 μm
87Sr/86Sr
(e)
UFG 1998 Core
>30 μm
0.2-30 μm
εNd

Figure 2.10. Isotope, dust concentration and trace element records. a) $\delta^{18}O$ from 1991 UFG ice core meltwater (Naftz et al., 1996). b) Dust concentration from FRE 98-4 separated into 1-5 (black circles) and >5 μm (black diamonds). c) Crustal enrichment of FRE 98-4 meltwater for the trace metals Cr, As, Cd, Pb, Cu and Zn, common industrial pollutants (circles distinguished by color, see legend; see table 2.S1 for concentrations of all trace elements analyzed). d) $^{87}Sr/^{86}Sr$ and e) ε_{Nd} for 0.2-30 μm (black circles) and >30 μm (red diamonds) insoluble dust.

Top Depth (m)	~Age (yrs A.D.)	Sample ID	Cr EF	As EF	Cd EF	Pb EF	Cu EF	Zn EF
20.29	1974	21a	1.4	24.9	22.3	5.7	17.0	40.8
20.29	1974	21b	1.1	19.2	13.4	4.4	16.5	39.1
20.29	1974	21c	1.7	38.7	49.9	22.5	19.6	43.9
29.81	1967	30a	1.1	36.8	71.9	10.5	17.0	63.4
29.81	1967	30b	0.7	16.6	25.2	18.6	9.7	33.2
29.81	1967	30c	4.6	71.6	119.6	34.8	55.2	99.6
33.36	1963	33a	1.4	52.3	39.1	8.1	21.3	56.9
33.36	1963	33b	0.6	28.2	30.7	7.6	11.2	23.3
33.36	1963	33c	0.9	36.1	44.2	12.1	19.0	44.9
62.36	1926	62a	4.3	43.9	21.1	79.8	19.8	115.5
62.36	1926	62b	3.4	92.2	30.6	314.9	32.6	420.1
62.36	1926	62c	4.3	61.3	71.5	198.0	48.9	169.5
70.25	1914	70a	0.7	65.7	19.0	146.8	24.8	8.6
70.25	1914	70b	0.7	53.5	19.0	109.5	22.9	9.4
70.25	1914	70c	1.0	51.3	17.6	110.0	20.5	59.0
84.42	1892	83a	1.0	43.6	29.8	58.0	15.8	80.8
84.42	1892	83b	0.9	85.6	50.7	95.8	31.4	53.9
84.42	1892	83c	0.8	115.3	29.3	103.2	30.9	57.4
95.87	1869	95a	0.8	125.3	8.4	336.2	32.7	21.0
95.87	1869	95b	0.8	84.1	8.0	226.7	36.3	16.2
95.87	1869	95c	0.9	67.1	9.9	180.3	43.7	12.9
109.16	1841	109a	0.8	58.1	35.8	230.2	23.5	8.3
109.16	1841	109b	0.8	66.3	15.1	164.0	18.9	6.1
109.16	1841	109c	0.8	55.7	22.9	173.3	15.5	6.9
120.33	1816	120a	0.8	48.2	175.5	136.6	7.4	9.6
120.33	1816	120b	0.8	33.5	180.8	39.2	6.2	6.2
120.33	1816	120c	0.8	33.3	213.9	51.7	5.6	6.5
131.95	1788	131a	1.0	23.2	123.5	76.1	5.6	40.9
131.95	1788	131b	1.1	26.6	53.6	99.2	7.9	45.3
131.95	1788	131c	1.4	35.9	44.5	147.5	9.1	101.7
140.67	1765	140a	0.9	13.0	28.8	56.9	3.9	4.5
140.67	1765	140b	0.9	31.5	22.0	771.6	7.7	8.7
140.67	1765	140c	0.9	42.3	23.9	880.2	20.1	14.7
145.40	1753	145a	0.8	44.1	36.3	342.7	20.9	11.6
145.40	1753	145b	1.0	28.2	18.3	110.1	7.9	4.5
145.40	1753	145c	0.9	15.0	413.4	119.1	34.1	22.1
158.74	1715	158a	0.8	6.5	23.5	3.0	8.4	9.6
158.74	1715	158b	0.9	13.6	73.0	4.4	17.0	23.7
158.74	1715	158c	0.8	8.8	17.1	3.7	11.9	7.3

Table 2.1 Trace element enrichment factors. Enrichment factors (EF) of trace metals from UFG ice sample meltwater.

2.3.4. Sr-Nd isotopic compositions as a tracer of variable dust provenance

Varying age and geologic history of continental crust results in unique Sr-Nd isotopic compositions for the source rock and resulting weathered material

available for aeolian transport; these radiogenic isotopes are a powerful tool for determining dust provenance (Aarons et al., 2013; Lupker et al., 2010). The Sr and Nd isotopic compositions of dust from the UFG ice, local potential dust material from the Wind River Range, PSAs, and dust records from other American West regions are reported in Figures 2.10d,e and 2.11 (See Table 2.2 and S2 for dust in ice and PSA isotope compositions respectively). Upper Fremont Glacier samples display a range of $^{87}Sr/^{86}Sr$ ratios: 0.71009 to 0.71630, and ε_{Nd} compositions: -9.3 to -19.4. These radiogenic isotope data variations are large compared to ice core records from Greenland and Antarctica (variability of $^{87}Sr/^{86}Sr$ < 0.005 and ε_{Nd} < 3 in any single ice core record (Delmonte et al., 2004a; Lupker et al., 2010). It is possible that each sample may represent < 1 year, and if this is indeed the case, the fluctuating radiogenic data indicates dust provenance varied significantly over the last 300 years.

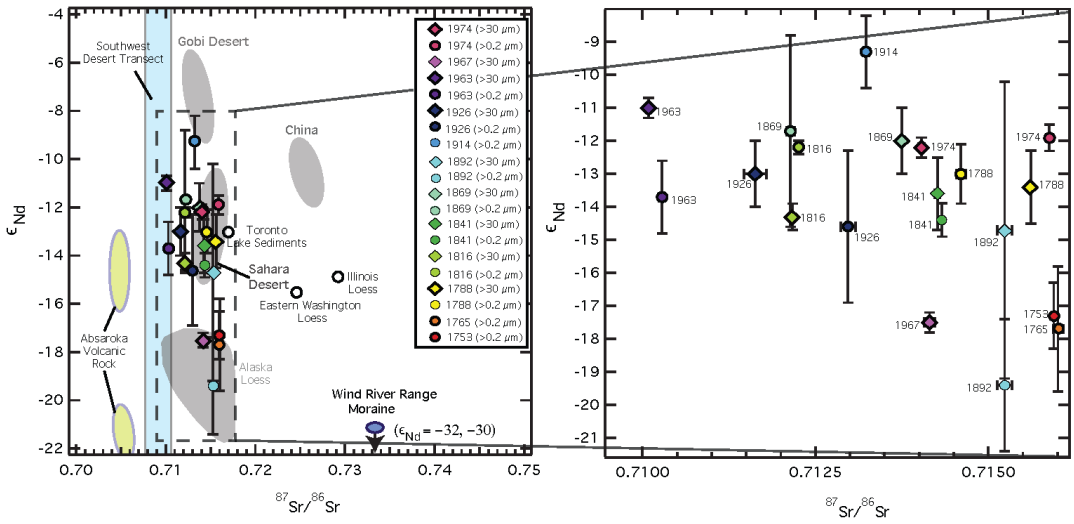

Figure 2.11 Combined radiogenic strontium and neodymium compositions of dust within UFG ice and potential source areas of dust. ε_{Nd} and $^{87}Sr/^{86}Sr$ for dust within UFG ice (symbols) and for potential sources of dust to UFG (labeled symbols and colored areas, (Ballantyne et al., 2011; Biscaye et al., 1997; Goldstein et al., 2008; Lawrence et al., 2011; Neff et al., 2008; Painter et al.,

2007). For $^{87}Sr/^{86}Sr$ analytical errors are smaller than the graph symbols. Right graph is zoomed in plot of ε_{Nd} and $^{87}Sr/^{86}Sr$ isotope compositions of dust.

Samples with good agreement between the fine and coarse fraction in both Sr and Nd isotopic composition suggest a uniform, local dust source. Samples possessing uniform fine and coarse Nd isotopic compositions, but a fine fraction displaying more radiogenic Sr isotopic compositions is consistent with a long range dust source; $^{87}Sr/^{86}Sr$ of dust particles is highly dependent upon the dust particle diameter and degree of weathering (Aarons et al., 2013). The $^{87}Sr/^{86}Sr$ and ε_{Nd} isotopic compositions of measured fine and coarse dust samples suggest potential mixing between dust originating primarily from the Colorado Plateau and American southwest deserts and another dust source with similar Sr compositions and more radiogenic ε_{Nd} (Figure 2.11). The combined Sr and Nd isotopic compositions of dust from the UFG are not in agreement with two separate Wind River Range moraine samples, indicating that local input of dust from a recently exposed Little Ice Age moraine material is unlikely (Figure 2.11).

Sample ID	Top Depth (m)	Approximate Age (yrs A.D.)	$^{87}Sr/^{86}Sr \pm 2\sigma\ 10^{-6}$	$^{143}Nd/^{144}Nd \pm 2\sigma\ 10^{-6}$	$\varepsilon_{Nd} \pm 2\sigma\ 10^{-6}$
21C	20.29	1974	0.714033 (40)	0.512015 (17)	-12.2 (0.3)
21F	20.29	1974	0.715880 (14)	0.512028 (21)	-11.9 (0.4)
30C	29.81	1967	0.714149 (79)	0.511742 (18)	-17.5 (0.3)
30F	29.81	1967	n.d.	n.d.	n.d.
33C	33.36	1963	0.710085 (24)	0.512076 (16)	-11.0 (0.3)
33F	33.36	1963	0.710283 (41)	0.511936 (58)	-13.7 (1.1)
62C	62.36	1926	0.711625 (164)	0.511974 (51)	-13.0 (1.0)
62F	62.36	1926	0.712970 (106)	0.511889 (115)	-14.6 (2.3)
70C	70.25	1914	0.713908 (38)	n.d.	n.d.
70F*	70.25	1914	0.713227 (42)	0.512164 (57)	-9.3 (1.1)
83C*	84.42	1892	0.716304 (168)	0.511883 (230)	-14.7 (4.5)
83F*	84.42	1892	0.715235 (108)	0.511646 (101)	-19.4 (2.0)
95C*	95.87	1869	0.713745 (21)	0.512025 (52)	-12.0 (1.0)
95F*	95.87	1869	0.712136 (58)	0.512040 (146)	-11.7 (2.9)
109C*	109.16	1841	0.714262 (38)	0.511938 (54)	-13.6 (1.1)
109F*	109.16	1841	0.714331 (17)	0.511902 (26)	-14.4 (0.5)
120C*	120.33	1816	0.712169 (16)	0.511906 (20)	-14.3 (0.4)
120F*	120.33	1816	0.712255 (19)	0.512014 (9)	-12.2 (0.2)
131C*	131.95	1788	0.715613 (23)	0.511951 (54)	-13.4 (1.1)
131F*	131.95	1788	0.714601 (67)	0.511970 (48)	-13.0 (0.9)
141C	140.67	1765	n.d.	n.d.	n.d.
141F*	140.67	1765	0.716006 (71)	0.511730 (98)	-17.7 (1.9)
145C	145.40	1753	0.715410 (191)	n.d.	n.d.
145F	145.40	1753	0.715946 (21)	0.511750 (50)	-17.3 (1.0)
158C	158.74	1715	0.710039 (481)	n.d.	n.d.
158F	158.74	1715	0.711767 (322)	n.d.	n.d.
BCR-2	-	-	0.705035 (7)	0.512642 (14)	0.1 (0.3)
BCR-2*	-	-	0.705035 (7)	0.512634 (32)	-0.1 (0.6)

Table 2.2. Radiogenic isotopic compositions of UFG dust. ε_{Nd} and $^{87}Sr/^{86}Sr$ isotopic compositions of insoluble particle fraction extracted from UFG ice samples. F and C denote fine and coarse grained samples respectively. (* denotes Nd measurements performed by TIMS equipped with 10^{13} Ohm resistors). Numbers in parenthesis represent internal standard error.

The isotopic compositions suggest that the globally significant upwind northern hemisphere dust sources (e.g. deserts of China, Alaska loess) are not the dominant dust source to this sector of the American West. Further, dust in these ice core samples have different isotopic compositions from dust deposited in the San Juan Mountains sourced from the Colorado Plateau (Figure 2.11). The average $^{87}Sr/^{86}Sr$ and ε_{Nd} dust isotopic compositions from modern dust collectors in the WRR are 0.713 and -15, respectively (Brahney et al., 2014), closely resembling the isotopic values of many younger UFG dust samples. Sr isotope data for ancient Green River basin lake sediments have $^{87}Sr/^{86}Sr$ ratios ranging from 0.710 to 0.715, values that are well within the boundaries of Sr isotopic composition measured here (Doebbert et al., 2014), although no published

literature data is available for Nd compositions. Large increases in dust originating from the semi-arid portion of the Green River basin have occurred in the western US in the past few decades, including in the Wind River Range, where dust deposition has doubled in the last decade (Brahney et al., 2013). Younger samples from the UFG appear to be close in isotopic composition to one data point from the Green River basin, whereas the deeper, older samples originate from an uncharacterized source (Figure 2.10d, 2.11). The oldest sample (158 meters depth, ~1715 A.D.) has the lowest dust concentration and Sr isotopic composition, and one of the lowest crustal EF, which we would expect during a time period with low anthropogenic influence.

Combining radiogenic isotopic compositions with dust particle diameter is a complementary method of classifying variations in dust source and transport distance. Air masses may originate from Alaska, but it is unlikely that the coarse dust fraction is derived from such long-range sources. Depending on the wind speed (on average ranging from 3-12 m/s), gravitational settling should remove all of the 30 μm dust size fraction within 3000 km of the dust source (Aarons et al., 2013). Combined with observed isotopic similarities of the coarse and fine-fraction material, we conclude that the dust within the UFG ice is sourced primarily from the continental US. The exception may be several deeper/older samples (1753, 1765 and 1892 A.D., fine fraction), displaying the most unradiogenic Nd compositions. The more contemporary and coarse fraction samples measure closer to the southwest desert and Colorado Plateau PSAs

and modern dust measured in the Wind River Range. Thus, our combined physical characterization-isotopic composition dataset hints at a temporal shift in dust provenance to a more local source, although additional data is necessary to assess the statistical significance. This chemical proxy supports observational records indicating that over the last 100 years, changes in land use practices combined with cyclical droughts have resulted in dust transported thousands of kilometers across North America (Dean, 1997; Mahowald et al., 2005).

2.4. Conclusions

This work provides the first radiogenic isotope measurements of dust entrained in a midlatitude North American glacier. Our results serve as a preliminary survey of dust deposited on the UFG throughout the timescale in question, and provide evidence of a transition to relatively local dust input as the average dust particle diameter increased from ~2 to ~5 μm between 1815-1974 A.D. The dust available for radiogenic isotope analysis in the UFG ice is two orders of magnitude less (e.g. < 1 ng Nd) than dust measured in modern dust and lake sediment core studies, emphasizing the utility of applying new analytical techniques (10^{13} Ω resistors on TIMS) to small samples. The results presented here demonstrate the variable provenance of dust transported to this sector of the American West. This radiogenic isotopic composition dataset highlights the incomplete reference database of Sr-Nd isotopic measurements from PSAs in North America, which must be addressed before further source-to-sink analyses of aeolian dust.

2.5. References

Aarons, S.M., Aciego, S.M., Gleason, J.D., 2013. Variable Hf-Sr-Nd radiogenic isotopic compositions in a Saharan dust storm over the Atlantic: Implications for dust flux to oceans, ice sheets and the terrestrial biosphere. Chemical Geology 349-350, 18-26.

Ballantyne, A., Brahney, J., Fernandez, D., Lawrence, C., Saros, J., Neff, J., 2011. Biogeochemical response of alpine lakes to a recent increase in dust deposition in the Southwestern US. Biogeosciences 8, 2689-2706.

Basile, I., Grousset, F.E., Revel, M., Petit, J.R., Biscaye, P.E., Barkov, N.I., 1997. Patagonian origin of glacial dust deposited in East Antarctica (Vostok and Dome C) during glacial stages 2, 4 and 6. Earth and Planetary Science Letters 146, 573-589.

Belnap, J., Gillette, D.A., 1997. Disturbance of biological soil crusts: Impacts on potential wind erodibility of sandy desert soils in southeastern Utah. Land Degrad. Dev. 8, 355-362.

Betzer, P.R., Carder, K.L., Duce, R.A., Merrill, J.T., Tindale, N.W., Uematsu, M., Costello, D.K., Young, R.W., Feely, R.A., Breland, J.A., Bernstein, R.E., Greco, A.M., 1988. A pulse of Asian dust to the Central North Pacific: Long range transport of giant mineral aerosol particles. Nature 314, 84-86.

Biscaye, P., Grousset, F., Revel, M., Van der Gaast, S., Zielinski, G., Vaars, A., Kukla, G., 1997. Asian provenance of glacial dust (stage 2) in the Greenland Ice Sheet project 2 ice core, Summit, Greenland. Journal of Geophysical Research 102, 765-781.

Boutron, C.F., Patterson, C.C., Barkov, N.I. , 1990. The occurrence of zinc in Antarctic ancient ice and recent snow. Earth and Planetary Science Letters 101, 248-259.

Brahney, J., Ballantyne, A.P., Kociolek, P., Spaulding, S., Otu, M., Porwoll, T., Neff, J.C., 2014. Dust mediated transfer of phosphorus to alpine lake ecosystems of the Wind River Range, Wyoming, USA. Biogeochemistry 120, 259-278.

Brahney, J., Ballantyne, A.P., Sievers, C., Neff, J.C., 2013. Increasing Ca2+ deposition in the western US: The role of mineral aerosols. Aeolian Research 10, 77-87.

Cecil, L.D., Vogt, S., 1997. Identification of bomb-produced chlorine-36 in mid-latitude glacial ice of North America. Nuclear Instruments & Methods in Physics Research Section B-Beam Interactions with Materials and Atoms 123, 287-289.

Curtis, J., Grimes, K., 2004. Wyoming climate atlas.

Dean, W.E., 1997. Rates, timing, and cyclicity of Holocene eolian activity in north-central United States: Evidence from varved lake sediments. Geology 25, 331-334.

Delmonte, B., Baroni, C., Andersson, P.S., Schoberg, H., Hansson, M., Aciego, S., Petit, J.R., Albani, S., Mazzola, C., Maggi, V., Frezzotti, M., 2010. Aeolian dust in the Talos Dome ice core (East Antarctica, Pacific/Ross Sea sector): Victoria Land versus remote sources over the last two climate cycles. Journal of Quaternary Science 25, 1327-1337.

Delmonte, B., Basile-Doelsch, I., Petit, J., Maggi, V., Revel-Rolland, M., Michard, A., Jagoutz, E., Grousset, F., 2004a. Comparing the EPICA and Vostok dust records during the last 220,000 years: stratigraphical correlation and provenance in glacial periods. Earth-Science Reviews 66, 63-87.
Delmonte, B., Petit, J.R., Maggi, V., 2002. Glacial to Holocene implications of the new 27000-year dust record from the EPICA Dome C (East Antarctica) ice core. Climate Dynamics 18, 647-660.
Doebbert, A.C., Johnson, C.M., Carroll, A.R., Beard, B.L., Pietras, J.T., Carson, M.R., Norsted, B., Throckmorton, L.A., 2014. Controls on Sr isotopic evolution in lacustrine systems: Eocene green river formation, Wyoming. Chemical Geology 380, 172-189.
Donarummo Jr., J., Ram, M., Stoermer, E.F., 2003. Possible deposit of soil dust from the 1930's U.S. dust bowl identified in Greenland ice. Geophysical Research Letters 30.
Draxler, R.R., Hess, G.D., 1998. An overview of the HYSPLIT 4 modelling system for trajectories, dispersion, and deposition. Aust. Meteorol. Mag. 47, 295-308.
Erel, Y., Dayan, U., Rabi, R., Rudich, Y., Stein, M., 2006. Trans Boundary Transport of Pollutants by Atmospheric Mineral Dust. Environmental Science and Technology 40.
Fischer, H., Siggaard-Andersen, M.-L., Ruth, U., Rothlisberger, R., Wolff, E., 2007. Glacial/interglacial changes in mineral dust and sea-salt records in polar ice cores: sources, transport and deposition. Reviews of Geophysics 45.
Fryxell, F., 1935. Glaciers of the Grand Teton National Park of Wyoming. Journal of Geology 43, 381-397.
Gabrielli, P., Planchon, F.A.M., Hong, S., Lee, K.H., Hur, S.D., Barbante, C., Ferrari, C.P., Petit, J.R., Lipenkov, V.Y., Cescon, P., Boutron, C.F., 2005. Trace elements in Vostok Antarctic ice during the last four climatic cycles. Earth and Planetary Science Letters 234, 249-259.
Goldewijk, K., 2001. Estimating global land use change over the past 300 years: The hyde database. Global Biogeochemical Cycles 15, 417-433.
Goldstein, H., Reynolds, R., Reheis, M., Yount, J., Neff, J., 2008. Compositional trends in aeolian dust along a transect across the southwestern United States. Journal of Geophysical Research-Atmospheres 113.
Grayson, D.K., 1993. The Desert's Past: A Natural Prehistory of the Great Basin. Smithsonian Institute Press, Washington, D.C.
Kampa, M., Castanas, E., 2008. Human health effects of air pollution. Environmental Pollution 151, 362-367.
Koornneef, J.M., Bouman, C., Schwieters, J.B., Davies, G.R., 2014. Measurement of small ion beams by thermal ionisation mass spectrometry using new 10^13 Ohm resistors. Analytica Chimica Acta 819, 49-55.
Lawrence, C., Neff, J., Farmer, G., 2011. The accretion of aeolian dust in soils of the San Juan Mountains, Colorado, USA. Journal of Geophysical Research-Atmospheres 116.
Lupker, M., Aciego, S.M., Bourdon, B., Schwander, J., Stocker, T.F., 2010. Isotopic tracing (Sr, Nd, U and Hf) of continental and marine aerosols in an 18th

century section of the Dye-3 ice core (Greenland). Earth and Planetary Science Letters 295, 277-286.
Lyles, L., 1985. Predicting and Controlling Wind Erosion. Agricultural History 59, 205-214.
Mahowald, N., Kohfeld, K., Hansson, M., Balkanski, Y., Harrison, S.P., Prentice, I.C., Schulz, M., Rodhe, H., 1999. Dust sources and deposition during the last glacial maximum and current climate: A comparison of model results with paleodata from ice cores and marine sediments. Journal of Geophysical Research-Atmospheres 104, 15895-15916.
Mahowald, N.M., Baker, A.R., Bergametti, G., Brooks, N., Duce, R.A., Jickells, T.D., Kubilay, N., Prospero, J.M., Tegen, I., 2005. Atmospheric global dust cycle and iron inputs to the ocean. Global Biogeochemical Cycles 19.
Middleton, N.D., Betzer, P.R., Bull, P.A., 2001. Long-range transport of 'giant' aeolian quartz grains: linkage with discrete sedimentary sources and implications for protective particle transfer. Marine Geology 177, 411-417.
Naftz, D., Klusman, R., Michel, R., Schuster, P., Reddy, M., Taylor, H., Yanosky, T., McConnaughey, E., 1996. Little Ice Age evidence from a south-central North American ice core, U.S.A. Arctic and Alpine Research 28, 35-41.
Naftz, D.L., 1993. Ice-Core Records of the Chemical Quality of Atmospheric Deposition and Climate from Mid-Latitude Glaciers, Wind River Range, Wyoming, Geology. Colorado School of Mines, Golden, CO, p. 220.
Naftz, D.L., Susong, D.D., Schuster, P.F., Cecil, L.D., Dettinger, M.D., Michel, R.L., Kendall, C., 2002. Ice core evidence of rapid air temperature increases since 1960 in alpine areas of the Wind River Range, Wyoming, United States. Journal of Geophysical Research-Atmospheres 107.
Neff, J.C., Ballantyne, A.P., Farmer, G.L., Mahowald, N.M., Conroy, J.L., Landry, C.C., Overpeck, J.T., Painter, T.H., Lawrence, C.R., Reynolds, R.L., 2008. Increasing eolian dust deposition in the western United States linked to human activity. Nature Geoscience 1, 189-195.
Painter, T., Barrett, A., Landry, C., Neff, J., Cassidy, M., Lawrence, C., McBride, K., Farmer, G., 2007. Impact of disturbed desert soils on duration of mountain snow cover. Geophysical Research Letters 34.
Patterson, E.M., Gillette, D.A., 1977. Commonalities in measured size distributions for aerosols having a soil-derived component. J. Geophys. Res. 82, 2074-2082.
Prospero, J.M., Ginoux, P., Torres, O., Nicholson, S.E., Gill, T.E., 2002. Environmental characterization of global sources of atmospheric soil dust identified with the Nimbus 7 Total Ozone Mapping Spectrometer (TOMS) absorbing aerosol product. Reviews of Geophysics 40.
Prospero, J.M., Lamb, P.J., 2003. African Droughts and Dust Transport to the Caribbean: Climate Change Implications. Science 302, 1024-1027.
Reheis, M.C., 1997. Dust deposition downwind of Owens (dry) Lake, 1991-1994: Preliminary findings. Journal of Geophysical Research-Atmospheres 102, 25999-26008.

Reheis, M.C., Budahn, J.R., Lamothe, P.J., Reynolds, R.L., 2009. Compositions of modern dust and surface sediments in the Desert Southwest, United States. Journal of Geophysical Research 114.
Reheis, M.C., Urban, F.E., 2011. Regional and Climatic controls on seasonal dust deposition in the southwestern U.S. Aeolian Research 3, 3-21.
Reynolds, R., Belnap, J., Reheis, M., Lamothe, P., Luiszer, F., 2001. Aeolian dust in Colorado Plateau soils: Nutrient inputs and recent change in source. Proceedings of the National Academy of Sciences of the United States of America 98, 7123-7127.
Schepanski, K., Tegen, I., Laurent, B., Heinold, B., Macke, A., 2007. A new Saharan dust source activation frequency map derived from MSG-SEVIRI IR-channels. Geophysical Research Letters 34.
Schepanski, K., Tegen, I., Todd, M.C., Heinold, B., Bonisch, G., Laurent, B., Macke, A., 2009. Meteorological processes forcing Saharan dust emission inferred from MSG-SEVIRI observations of subdaily dust source activation and numerical models. Journal of Geophysical Research-Atmospheres 114.
Schulz, M., Balkanski, Y., Guelle, W., Dulac, F., 1998. Role of aerosol size distribution and source location in a three-dimensional simulation of a Saharan dust episode tested against satellite derived optical thickness. Journal of Geophysical Research 103, 10,579-510,592.
Schuster, P., Krabbenhoft, D., Naftz, D., Cecil, L., Olson, M., Dewild, J., Susong, D., Green, J., Abbott, M., 2002. Atmospheric mercury deposition during the last 270 years: A glacial ice core record of natural and anthropogenic sources. Environmental Science and Technology 36, 2303-2310.
Schuster, P., White, D., Naftz, D., Cecil, L., 2000. Chronological refinement of an ice core record at Upper Fremont Glacier in south central North America. Journal of Geophysical Research-Atmospheres 105, 4657-4666.
Thevenon, F., Anselmetti, F., Bernasconi, S., Schwikowski, M., 2009. Mineral dust and elemental black carbon records from an Alpine ice core (Colle Gnifetti glacier) over the last millennium. Journal of Geophysical Research-Atmospheres 114.
Thompson, L., Davis, M., Mosley-Thompson, E., Sowers, T., Henderson, K., Zagorodnov, V., Lin, P., Mikhalenko, V., Campen, R., Bolzan, J., Cole-Dai, J., Francou, B., 1998. A 25,000-year tropical climate history from Bolivian ice cores. Science 282, 1858-1864.
Uglietti, C., Gabrielli, P., Olesik, J.W., Lutton, A., Thompson, L.G., 2014. Large variability of trace element mass fractions determined by ICP-SFMS in ice core samples from worldwide high altitude glaciers. Applied Geochemistry 47, 109-121.
Wolff, E.W., et al., 2006. Southern Ocean sea ice, DMS production and iron flux over the last eight glacial cycles. Nature 440, 491-496.

CHAPTER III

The impact of glacier retreat from the Ross Sea on local climate: characterization of mineral dust in the Taylor Dome ice core, East Antarctica

Official citation:
S.M. Aarons, S.M. Aciego, P. Gabrielli, B. Delmonte, J.M. Koornneef, A. Wegner, and M.A. Blakowski, 2016. The impact of glacier retreat from the Ross Sea on local climate: characterization of mineral dust in the Taylor Dome ice core, East Antarctica. Earth and Planetary Science Letters. *In Press.* Reproduced within author's rights.

(Accepted as an article in Earth and Planetary Science Letters, 2016)

Abstract

Recent declines in ice shelf and sea ice extent experienced in polar regions highlight the importance of evaluating variations in local weather patterns in response to climate change. Airborne mineral particles (dust) transported through the atmosphere and deposited on ice sheets and glaciers in Antarctica and Greenland can provide a robust set of tools for resolving the evolution of climatic systems through time. Here we present the first high time resolution radiogenic isotope (strontium and neodymium) data for Holocene dust in a coastal East Antarctic ice core, accompanied by rare earth element composition, dust concentration, and particle size distribution during the last deglaciation. We aim to use these combined ice core data to determine dust provenance, with variations indicative of shifts in either dust production, sources, and/or transport pathways. We analyzed a series of 17 samples from the Taylor Dome (77°47'47'' S, 158°43'26'' E) ice core, 113-391 m in depth from 1.1-31.4 ka. Radiogenic

isotopic and rare earth element compositions of dust during the last glacial period are in good agreement with previously measured East Antarctic ice core dust records. In contrast, the Holocene dust dataset displays a broad range in isotopic and rare earth element compositions, suggesting a shift from long-range transported dust to a more variable, local input that may be linked to the retreat of the Ross Ice Shelf during the last deglaciation. Observed changes in the dust cycle inferred from a coastal East Antarctic ice core can thus be used to infer an evolving local climate.

1. Introduction

Fluctuations in the amount and/or extent of sea ice and ice shelves alter wind speed and direction, as well as local storm trajectories (Francis et al., 2009; Vihma, 2014). Modeling the interaction between ice sheets and local climate demonstrates that air is cooled locally over an ice sheet, affecting the atmospheric flow response (Liakka and Nilsson, 2010). The high albedo and altitude of ice sheets can induce zonal anomalies in surface temperature, which can modify large-scale atmospheric circulation (Beghin et al., 2014; Cook and Held, 1988). Furthermore, several studies have implied that an ice sheet is capable of changing the position of the subtropical jet, in turn altering storm trajectories (Hall et al., 1996; Kageyama and Valdes, 2000; Laîné et al., 2008; Rivière et al., 2010). The change in storm trajectories will undoubtedly result in changes in precipitation pathways and the ice accumulation rates over ice sheets

(Beghin et al., 2014). It is possible that variations in the extent of glaciation, sea-ice and ice shelves are capable of driving significant atmospheric climatic variations on seasonal, decadal, millennial and glacial-interglacial cycles.

Ice cores from the Antarctic ice sheet provide records of past climate extending over hundreds of thousands of years (Jouzel et al., 1995; Petit et al., 1999). Chemical and mineralogical characterization of dust particles transported through the atmosphere and deposited on ice sheets and glaciers allow for the reconstruction of regional and global climate patterns. The dust concentration and composition of long timescale ice cores varies with air temperature as recorded by stable isotopes: previous studies have established that dust concentration is one-to-two orders of magnitude greater during glacial versus interglacial periods. The increased dust deposition may be attributed to higher dust availability at source areas and higher wind speeds caused by a stronger equator to pole temperature gradient (Delmonte et al., 2004a; Hammer et al., 1985), or stronger wind gusts in dust source regions during periods of steepened meridonal temperature gradients (McGee et al., 2010). Provenance of dust deposited in ice can be characterized using radiogenic isotopes, including strontium ($^{87}Sr/^{86}Sr$), neodymium ($^{143}Nd/^{144}Nd$), hafnium ($^{176}Hf/^{177}Hf$) (Basile et al., 1997; Delmonte et al., 2008; Delmonte et al., 2004a; Delmonte et al., 2004b; Grousset and Biscaye, 2005; Lupker et al., 2010), and REE concentration (Wegner et al., 2012). The isotopic composition of ice core dust compared to Potential Source Areas (PSAs) of windborne material indicate variations in the

dust provenance (Delmonte et al., 2004a; Wolff et al., 2006), which may be used to resolve past climate changes. The longest timescale ice core records are from interior East Antarctica (Petit et al., 1999), yet ice cores from coastal East Antarctic sites (i.e. Talos Dome) are capable of providing undisturbed, detailed records of the last climatic cycle in a region of the East Antarctic ice sheet with distinctive climate conditions (Delmonte et al., 2010).

Previous work on central and coastal east Antarctic ice cores identify southern South America (SSA) as the most likely source of windblown mineral dust during late Quaternary glacial periods. The size distribution and chemical composition of dust from interglacial periods is more variable and in coastal ice cores may potentially originate from local sources, although analytical limitations have made correlating interglacial ice core dust to source area challenging (Delmonte et al., 2010; Delmonte et al., 2007; Gabrielli, 2010).

In 1992, a ~554 m deep ice core was retrieved at Taylor Dome (TYD) (M3C1 ice core, 77°47’47’’ S; 158°43’26’’ E, 2365 m a.s.l.), a local ice-accumulation area for the Taylor Glacier. TYD is located on the eastern margin of the East Antarctic ice sheet (Figure 3.1), in close proximity to the current position of the Ross Ice Shelf and seasonal sea ice of the Ross Sea. The TYD core was the third ice core (following Vostok and the first Dome C core) to provide a stratigraphically intact record of the Holocene through the last glacial cycle, going back to ~130 ka (Grootes et al., 1994; Steig, 2000).

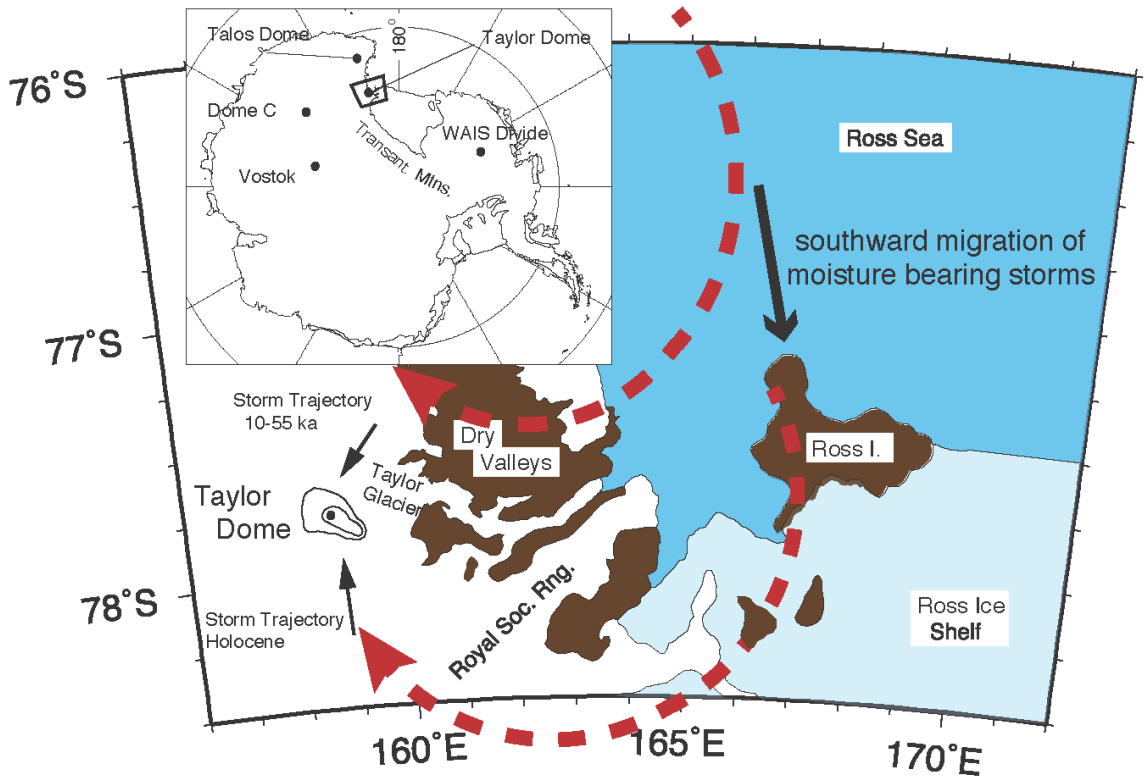

Figure 3.1. Map of Taylor Dome and surrounding area in East Antarctica. Major ice core drilling sites and the hypothesized Last Glacial Maximum (top dashed arrow) and current Holocene (bottom dashed arrow) storm trajectory (Figure adapted from Morse et al., 1998).

Katabatic-driven movements of cold interior Antarctica air masses approaching from the southwest largely influences the weather at TYD (Morse et al., 1998), whereas warmer, precipitation-laden air masses approach TYD from the south (Morse, 1997). The latter air masses are linked to cyclones originating near Marie Byrd Land (Figure 3.1), traveling over the Ross Ice Shelf and across the Transantarctic Mountains before deposition at TYD (Harris, 1992).

During the Last Glacial Maximum (LGM), the accumulation rate at TYD drastically decreased, suggesting a change in atmospheric circulation during the

late ice age period (Morse et al., 1998b). Morse et al. (1998) hypothesized that moisture-bearing storms arrived at TYD from the north (rather than the south as they do presently), a result of changing ice cover in the Ross Embayment. The elevated topography in the Ross Embayment (e.g. from the Ice Shelf or Ross 'Ice Sheet') and northward displacement of the Ross Low combined to displace the storm tracks northward through the Transantarctic Mountains north of the Royal Society Range (Morse et al., 1998b) (Figure 1). Terrestrial and marine geological evidence indicates that grounded ice advanced far into the Ross Sea during the LGP, reaching its greatest thickness and extent between 12.8-18.7 ka (Hall et al., 1996). The recession of the ice sheet began about 12.8 ka, and it retreated from the McMurdo Sound area over the period 11.5-6 ka (Anderson et al., 1992; Licht et al., 1996), aligned with the proposed timeline for southerly storm trajectories.

We utilize the TYD ice core dust record to examine the changes in local weather and storm trajectories during and following the retreat of the Ross Ice Shelf during the last deglaciation. Dry and windy conditions throughout the LGP are likely to have established the dominance of dry-deposited dust on TYD, as opposed to sea-salt aerosol. The dust accumulation rates should have decreased throughout the last deglaciation, and the sources and transport pathways of dust may have remained similar to those from the LGP (Hinkley and Matsumoto, 2001) or alternatively could have been completely restructured due to the major climate shift. The retreat of the Ross Ice Shelf, 11.5-6 ka, should have had a significant impact upon the dust record, consistent with the dust

record at Talos Dome (Delmonte et al., 2010) as hypothetically, storm trajectories and dominant winds would migrate southward to approach TYD from the southeast (Figure 1).

Sea salt aerosol, is yet another indicator of sea ice and ice shelf extent (Lupker et al., 2010; Wolff et al., 2006); it originates from sea ice covered with brine, frost flowers and bubble bursting over seawater. Here we measure the isotopic and elemental characteristics of the soluble fraction (<0.2 μm) of the TYD ice core for comparison to the insoluble fraction, which is comprised of dust between 0.2 and 30 μm in diameter. Particles larger than 30 μm in diameter were not measured due to the low dust availability and instrumental detection limitations.

This work presents the first detailed Sr and Nd isotopic dataset of coastal Antarctic ice core dust during the last deglaciation. We employ a newly developed mass spectrometry technique utilizing 10^{13} Ohm resistors which can effectively measure variations in Nd isotope composition of extremely small samples to the fourth decimal place (Koornneef et al., 2014). The goals of the study are: (1) to provide the first high-resolution record of dust deposited in East Antarctica during the last deglaciation and into the Holocene, (2) identify and compare the geochemical (radiogenic isotope compositions and rare earth element concentrations) and physical characteristics (dust concentration and particle size) of ice core dust to PSAs from Southern South America (SSA) and the Ross Sea sector (e.g. McMurdo Dry Valleys), (3) explore the effects of the

retreating Ross Ice Shelf upon regional storm trajectories using the dust record preserved in the TYD ice core, and (4) establish the likely sources of dust to TYD during the LGP and the Holocene.

2. Materials and Methods

2.1 Ice core processing

A series of 17 ice core samples from the TYD ice core (M3C1) were selected between 113 and 391 m depth (see Table 3.1 for depths and ages). The samples measured here encompass a time period of ~1.1 to ~31.4 ka before 1950 A.D. Synchronization of the CO_2 concentration record to EPICA Dome C (EDC) and Dronning Maud Land (EDML) ice cores provided chronological refinement of the TYD ice core to approximately 20 ka (Monnin et al., 2004). Recent work has refined the TYD age-scale (Baggenstos, 2015) based on combining the work of Monnin et al. (2004) to 20 ka, and Ahn and Brook (2007) to 60 ka. The updated age scale of Baggenstos (2015) is indistinguishable from the original Brook et al. (2000) age scale for 20-40 ka, the time period encompassing the oldest sample in this study. We use the Monnin et al. (2004) timescale for 1-20 ka and Brook et al. (2000) for 20-60 ka.

Each sample is approximately 660 g and 22 cm long and spans between ~3 and ~30 years. The ice was cut into 3 longitudinal samples for radiogenic isotope, REE, and dust concentration and size distribution analysis, respectively. The

REE and dust concentration and size distribution samples were cut latitudinally into two subsamples (labeled ‘a’ and ‘b’, see Table 3.S1-S4) to obtain a higher temporal resolution. Decontamination and melting occurred in class 10 laminar flow hoods at the University of Michigan. To remove the outer layer and potential contamination each ice sample was scraped using acid-cleaned PFA chisels. The sample was then rinsed using ultra-pure distilled ethanol (Acros Organics) and subsequently rinsed twice with MilliQ water.

2.1.1 REE sample preparation

The traditional “acid leach” REE portion of each sample was triple rinsed with MilliQ water using acid pre-cleaned LDPE calipers and melted in pre-cleaned LDPE Nalgene bottles following procedures established by Boutron (1990). The meltwater was immediately acidified in 1% HNO_3 (ultra-pure) for approximately 1 month prior to analysis. The “full digestion” REE portion consisted of 100 µL taken from each insoluble and soluble sample digested and dissolved in 1 ml of 6M HCl. The samples were subsequently dried down and acidified in 1% v/v HNO_3 for comparison to the traditional “acid leach” REE portion of ice core samples.

The dust concentration and size distribution samples were triple rinsed with MilliQ water using acid pre-cleaned LDPE calipers and stored frozen in triple rinsed PFTE centrifuge tubes until just prior to analysis following the procedures described in Delmonte et al. (2004a).

2.1.2 Radiogenic isotope sample preparation

Ice core sections for radiogenic isotope analysis were buffered to neutral pH during melting with ultra-pure optima grade ammonia (Fischer Scientific) to prevent the dissolution of mineral particles (Aciego et al., 2009). Immediately afterwards, melted samples were filtered through pre-cleaned 0.2 μm and 30 μm filters (particles greater than 30 μm were not measured due to dust availability and analytical limitations). The filtered water (we operatively define as the "soluble fraction" and denote as 'W') was collected in a pre-cleaned Teflon beaker for analysis.

Insoluble fractions (denoted as 'F') were dissolved directly off the 0.2 μm filters using ultra-pure HCl, aqua regia, and HNO_3-HF acid for "total digestion" portions, whereas the soluble fraction was dried under nitrogen flow and infrared radiation before dissolution in ultra-pure 9M HCl acid for chemistry (Aciego et al., 2009).

Finally, aliquots of both soluble and insoluble fractions (denoted as 'W' and 'F' respectively) were also chemically separated using ion-exchange columns and Eichrom resins following established procedures of Aciego et al. (2009) and Aarons et al. (2013) for Sr and Nd isotopic analysis. For a full description of sample preparation see Figure 3.2.

2.2 PSA sample processing

We use PSA samples from the East Antarctic ice sheet margin for source to sink analyses of TYD ice core dust to PSA dust from the Ross Sea Region. The Ross Sea Region PSAs were selected from the fine fraction of regolith, exposed glacial deposits, and sediments below the surficial deflation eolic pavement (1-3 cm) (Blakowski et al., In Press). Approximately 10 mg of each sample were digested in concentrated HF in a Savillex Teflon beaker inside a steel-jacketed Parr acid digestion bomb at 220° C for 48 hours. The insoluble PSA samples were then dried down and immersed in 6 M HCl at 180° C for 12-24 hours, dried down, and dissolved in 1 mL of 9M HCl. Sample aliquots of 100 µL were extracted and dried down prior to being re-acidified in 1% HNO_3. The acid leach method for the ice samples is: acidification in 1% HNO3 (ultra-pure) for approximately 1 month prior to analysis consistent with the methods from Uglietti et al. (2014).

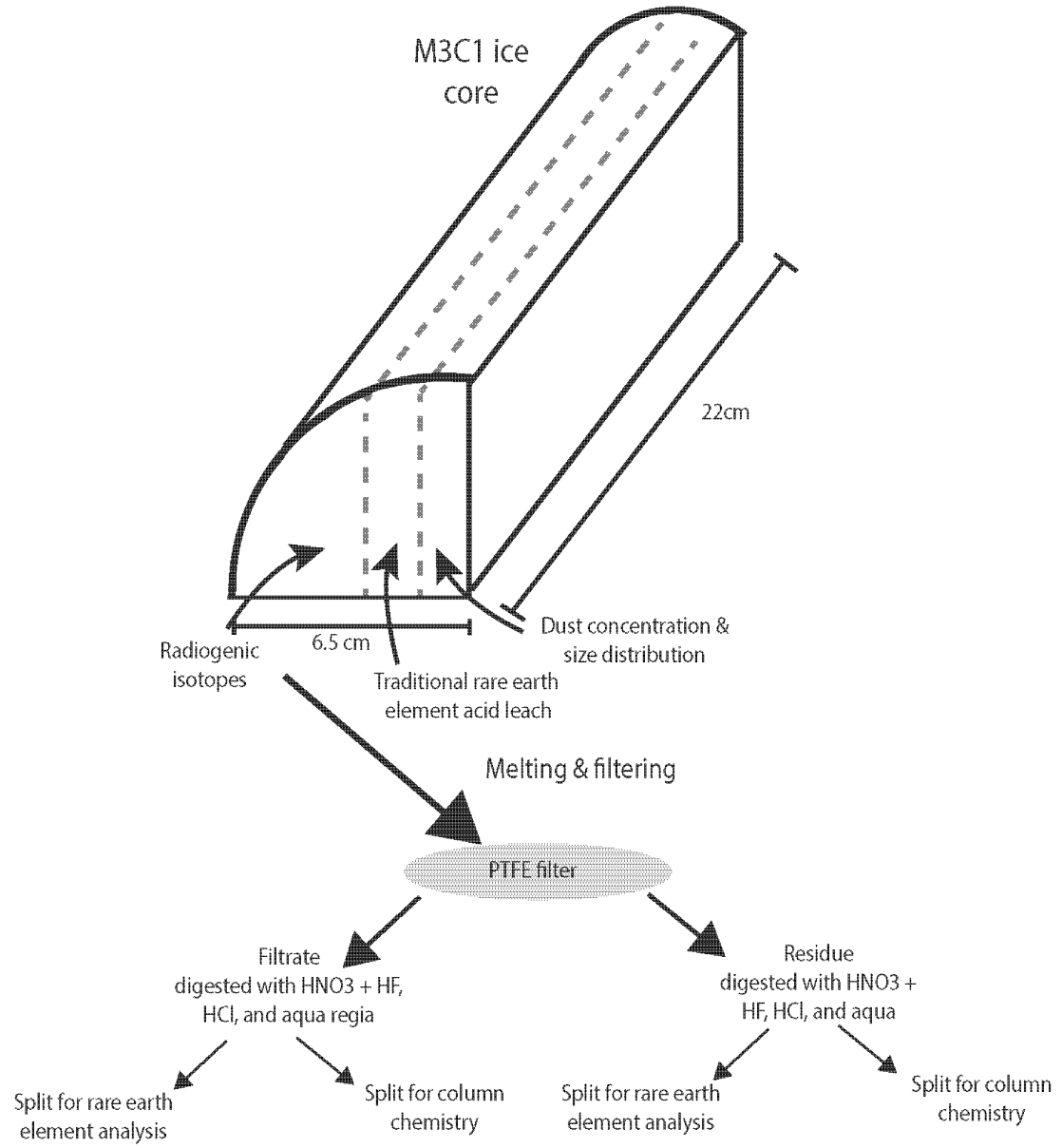

Figure 3.2. Schematic of ice core sample preparation for radiogenic isotope and rare earth element analysis of insoluble and soluble portion of TYD ice core. *Insoluble portion of ice core is mineral dust and soluble portion is filtered ice, denoted as 'F' and 'W' respectively.

2.3 REE concentration analysis

The REE concentrations of TYD ice were measured using ICP-SFMS (Element 2, Thermo Scientific) coupled with a micro-flow nebulizer and desolvation system (Apex Q) in the clean laboratory at the Byrd Polar and Climate Research Center

at The Ohio State University following the procedures in Gabrielli et al. (2006) and Gabrielli (2010). REE detection is at the sub-pg g^{-1} levels (Gabrielli et al., 2006), with procedural blanks concentrations 61 and 7.5 times smaller than sample concentrations for the traditional leaching and full acid digestion method respectively (see Table 3.S2).

2.4 Dust concentration and size distribution analysis

Dust concentration and size distribution measurements were conducted by Coulter® Counter at the University of Milan as in Delmonte et al. (2002) and kept frozen until analysis. For each dust concentration and size distribution subsample ~20 ml was available for Coulter® Counter microparticle concentration and size distribution measurements in the range of 1.006-29.83 μm.

2.5 Strontium and neodymium isotope analyses

Chemically separated Sr and Nd were measured using thermal ionization mass spectrometry (TIMS) equipped with 10^{11} Ohm resistors for $^{87}Sr/^{86}Sr$ ratios and 10^{13} Ohm resistors for $^{143}Nd/^{144}Nd$ ratios. Sr isotopic compositions were measured on the University of Michigan Thermo Scientific Triton Plus TIMS and normalized to $^{88}Sr/^{86}Sr=8.375209$ to account for mass bias. The Sr isotopic standard NBS987 (100 ng) long-term average is $^{87}Sr/^{86}Sr=0.710245 \pm 17$ (2σ SD, n=268). The USGS reference material BCR-2 (10 ng) measured concurrently with samples averaged 0.705002 ± 37 (2σ SD, n=3), which agrees with published

BCR-2 values (0.705013, 0.705000; Aciego et al. (2009) and Jweda et al. (2015) respectively).

The majority of Nd isotopic compositions were measured on a Thermo Scientific Triton *Plus* TIMS using low-noise 10^{13} Ohm resistors at the Vrije Universiteit in Amsterdam and normalized to $^{146}Nd/^{144}Nd=0.7219$ using the exponential law and mass 147 was monitored to detect any Sm interference (Koornneef et al., 2014). USGS reference material BCR-2 (1 ng) measured concurrently with the samples averaged 0.512634 ± 32 (2σ SD, n=2), in agreement with measured values in Jweda et al. (2015) of $^{143}Nd/^{144}Nd=0.512637$. The $^{143}Nd/^{144}Nd$ ratio of isotopic standard CIGO (100 pg) was measured simultaneously at $^{143}Nd/^{144}Nd=0.511344$ ± 49 (2σ SD, n=5), close to the long-term average value of $^{143}Nd/^{144}Nd=0.511334$ ± 10 (2σ SD, n=28) (Koornneef et al., 2014), demonstrating that 10^{13} Ohm resistors can effectively measure variations in $^{143}Nd/^{144}Nd$ to the fourth decimal place for samples as small as 100 pg. Two LGP samples (381 and 383) were measured on a Thermo Scientific Triton *Plus* TIMS using standard 10^{11} Ohm resistors at the University of Michigan and normalized to $^{146}Nd/^{144}Nd=0.7219$ using the exponential law and mass 149 was monitored to detect any Sm interference. BCR-2 (10 ng) measured concurrently with the samples averaged 0.512642 ± 42 (2σ SD, n=4), similar to measured values (Jweda et al., 2015). The long-term average for JNdi-1 is 0.512101 ± 12 (2σ SD, n=110).

3. Results

The dust concentration and size distribution, REE, Na and Sr concentrations of the fifteen ice core sections are summarized in Table 3.S1, S3, and S4 respectively.. Sr and Nd isotopic composition of the TYD dust and ice samples are summarized in Table 3.1.

Sample ID	Top Depth (m)	Ice Age (ka)	$^{87}Sr/^{86}Sr \pm 2\sigma\ 10^{-6}$	$^{143}Nd/^{144}Nd \pm 2\sigma\ 10^{-6}$	$\varepsilon_{Nd} \pm 2\sigma\ 10^{-6}$
113F	113.12	1.1	0.712856 (227)	0.512296 (129)	-6.7 (2.5)
113W	113.12	1.1	0.710033 (65)	0.512286 (191)	-6.9 (3.7)
136F	136.12	1.5	0.708418 (540)	-	-
136W	136.12	1.5	0.710078 (86)	0.511948 (126)	-13.5 (2.5)
176F	176.10	2.2	0.708323 (297)	-	-
176W	176.10	2.2	-	0.512297 (130)	-6.7 (2.5)
208F	208.13	3.1	0. 714972 (115)	0.512436 (191)	-3.9 (3.7)
208W	208.13	3.1	0.709012 (50)	0.512111 (277)	-10.3 (5.4)
266F	264.80	4.8	0.705428 (33)	0.512446 (163)	-3.8 (3.2)
266W	264.80	4.8	0.705152 (33)	0.512368 (137)	-5.3 (2.7)
281F	279.48	5.3	0.716308 (259)	0.512273 (75)	-7.1 (1.5)
281W	279.48	5.3	0.705353 (21)	0.512360 (84)	-5.4 (1.6)
296F	294.68	6 .0	0.706593 (46)	-	-
296W	294.68	6. 0	0.710128 (33)	0.512242 (89)	-7.7 (1.7)
299F	297.50	6.1	0.709332 (178)	-	-
299W	297.50	6. 1	0.710383 (57)	0.512282 (74)	-6.9 (1.4)
308F	306.50	6.5	0.710751 (244)	0.512594 (170)	-0.9 (3.3)
308W	306.50	6.5	0.707023 (38)	0.512347 (62)	-5.7 (1.2)
323F	321.5	7.3	0.709708 (168)	0.512550 (87)	-1.7 (1.7)
323W	321.5	7.3	0.709522 (75)	0.512333 (93)	-6.0 (1.8)
340F	339.14	9.4	0.713616 (229)	0.512509 (132)	-2.5 (2.6)
340W	339.14	9.4	0.710054 (64)	0.512496 (71)	-2.8 (1.4)
349F	347.6	10.5	-	-	-
349W	347.6	10.5	0.709885 (38)	0.512227 (86)	-8.0 (1.7)
366F	364.60	13.0	0.712416 (98)	0.512398 (194)	-4.7 (3.8)
366W	364.60	13.0	0.709389 (72)	0.512588 (165)	-1.0 (1.4)
376F	374.70	15.5	0.705225 (28)	0.512544 (47)	-1.8 (0.9)
376W	374.70	15.5	0.708497 (74)	0.512595 (54)	-0.8 (1.1)
381F	380.3	19.7	0.710116 (24)	0.512505 (8)	-2.6 (0.15)
381W	380.3	19.7	0.709255 (39)	0.512427 (53)	-4.1 (1.0)
383F	381.5	20.7	0.708974 (9)	0.512459 (62)	-3.5 (1.2)
383W	381.5	20.7	0.710059 (5)	0.512583 (25)	-1.1 (0.5)
392F	391.12	31.4	0.708714 (35)	0.512591 (71)	-0.9 (1.4)
392W	391.12	31.4	0.708950 (77)	0.512605 (47)	-0.6 (0.9)

Table 3.1. Radiogenic isotope compositions of Taylor Dome ice samples. ε_{Nd} and $^{87}Sr/^{86}Sr$ isotopic compositions of ice core samples measured in this study, top depth and age are noted. Ages are based upon synchronization of CO_2 record in TYD, EDC and EDML ice cores (Monnin et al., 2004). *'F' and 'W' are insoluble and soluble portions.

3.1 Dust concentration and size distribution

Dust concentrations are >500 and <15 ppb during glacial and interglacial periods respectively (Figure 3.S1), which is similar to dust concentrations observed in interior Antarctic ice cores (Delmonte et al., 2008; Delmonte et al., 2004a; Delmonte et al., 2007; Delmonte et al., 2002). In the 1-5 μm, 1-10 μm, and 1-20 μm dust diameter size range, the dust concentrations range from ~9-537 ppb, 14-541 ppb, and 14-544 ppb respectively.

The mean mass TYD dust particle diameter calculated using volume distribution increases with decreasing depositional age (Table 3.S1). Our measured mean mass TYD Holocene dust particle diameter (~3 μm) is larger than the glacial dust particle diameter (~1.8 μm). The two oldest glacial samples, from ~31.4-15.5 ka are lognormally distributed with a modal value of ~2 μm, consistent with the long-range transported dust observed in the Talos Dome ice core (Albani et al., 2012; Delmonte et al., 2010). To explore the difference in grain size distributions further, we use the proportion of fine particles (fine particle percentage, or FPP) and coarse particles (coarse particle percentage, or CPP) with respect to the total mass as defined in Delmonte et al. (2004b). Samples from the Holocene (~1.1-10.5 ka) on average have a high CPP greater than 2 μm (~85%) than older samples (~13-31.4 ka) with a CPP of ~69% (Table 3.S1).

Larger dust particle diameters observed during the Holocene is also observed at Talos Dome, a coastal ice core in East Antarctica (Albani et al., 2012) and the West Antarctic Ice Sheet (WAIS) Divide deep ice core (Koffman et al., 2014). The

dust input at TYD, Talos Dome and WAIS Divide during the Holocene is dominated by larger dust particles whereas the dust concentration during the LGP is attributed to finer dusts.

The dust flux rates at TYD are determined using the variable water equivalent accumulation rates (calculated from ice equivalent) for each time period (Morse et al., 1998b) and dust concentration (this study) (Figure 3.4). On average, the flux of dust particles between 1-20 μm during the LGP was ~3.9 mg m^{-2} yr^{-1} compared to ~2.3 mg m^{-2} yr^{-1} during the Holocene. The average flux of dust particles between 1-5 μm and 1-10 μm was ~3.6 and ~3.7 mg m^{-2} yr^{-1} during the LGP and decreased to ~1.1 and ~1.5 mg m^{-2} yr^{-1} during the Holocene. The dust flux record of fine particles (1-5 μm) at TYD follows a similar pattern observed at EDC, however the change in TYD dust flux across the termination of the LGP is smaller (Figure 3.4). The flux of larger dust particles (up to 20 μm) is significantly higher during the Holocene compared to the LGP (Figure 3.4). The difference in dust flux between the TYD and EDC ice cores is substantial, however the overall trend is similar (Figure 3.4). The dust flux in the most recent portion of the TYD record is comparable to WAIS Divide ice core (Koffman et al., 2014), however comparison to older sections is not yet available. When compared to the Talos Dome record (Albani et al., 2012), the dust flux is slightly higher in the TYD record during the Holocene, but the difference in dust flux from the two ice cores between the LGP and Holocene is distinctive, most notably in the coarse dust particle portion.

3.2 Rare Earth Element concentrations

3.2.1 REE concentrations of TYD insoluble fraction

REEs serve as a valuable tool for characterizing mineral dust in Antarctic ice, and we differentiate between light REEs (LREEs: La, Ce, Pr, Nd), medium REEs (MREEs: Sm, Eu, Gd, Tb, Dy, Ho), and heavy REEs (HREEs: Er, Tm, Yb, Lu). The REE concentrations of the TYD ice were normalized to the mean upper continental crustal abundance of each element (Wedepohl, 1995) (Figure 3.3). Comparable shapes of REE patterns could indicate uniform dust sources (or uniform mixing of sources); whereas departures from a constant pattern could indicate a change in dust source(s). The REE concentrations of the TYD samples follow the dust concentrations for glacial/interglacial REE concentrations in other Antarctic ice cores (Gabrielli, 2010; Wegner et al., 2012). Higher input of continental dust during glacial periods results in higher REE concentrations observed in glacial samples compared to interglacial samples. All of the samples from the Holocene display a unique positive Eu anomaly (Figure 3.5b), which is not found in Holocene samples in ice cores from the interior East Antarctic ice sheet (Gabrielli, 2010; Wegner et al., 2012).

3.2.2 REE concentrations of TYD soluble fraction

The REE concentrations of the full-digestion soluble and insoluble fractions follow similar but not identical patterns (Figure 3.S4). REE concentrations of the

LGP ice samples are higher than the majority of the Holocene samples and have a unique positive Eu anomaly. Another sample (1.1 ka, sample 113) has a pronounced enrichment in Pr not observed in any other soluble samples (Figure 3.6). We would expect the REE composition of the soluble fraction of TYD ice to be similar to seawater, however only Antarctic Bottom water REE data exists in current literature (Kawabe et al., 1998). The REE composition of the soluble fraction of TYD ice and Antarctic Bottom water do not match (Figure 3.6).

3.2.3 REE concentrations of potential source area dust

We include 76 PSA dust samples from the Ross Sea Sector (Baroni et al., 2008; Delmonte et al., 2010) from 17 locations along the north-central Transantarctic Mountains, the ice-free valleys and nunataks of Victoria Land and nearby McMurdo Sound sector for source-to-sink comparison. The bedrock ranges from late Proterozoic to early Paleozoic granites and gneisses, Devonian to Triassic Beacon Supergroup sedimentary rocks and the sills of the Jurassic Ferrar dolerite (Blakowski et al., In Press; Stump and Fitzgerald, 1992). The sampled material ranges from regolith, glacial dunes, lacustrine sand, and volcanic material. See Supplementary Table 3.S5 for more detailed information on the sample geologic history, geographic surroundings, climate and collection. The REE concentrations of the PSA dust from the Ross Sea Sector display a uniform crustal pattern (Figure 3.3c), with a slight enrichment of heavy REE with respect to light REE.

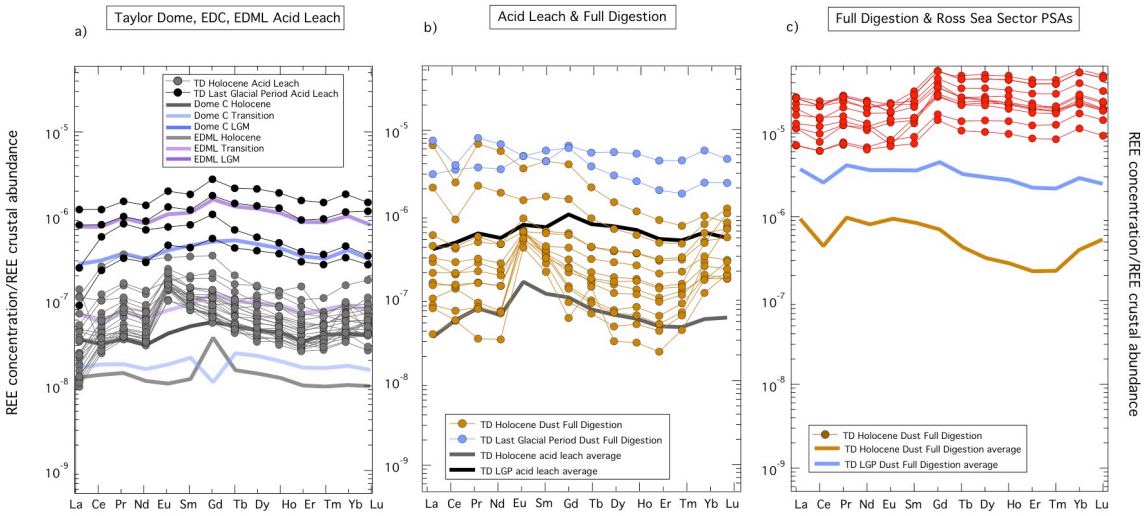

Figure 3.3. Rare earth element concentrations of TYD dust in ice. a) Normalized REE concentrations with respect to the mean crustal abundance (Wedepohl, 1995) in the 13 LGP and Holocene acid leached TYD ice samples with REE normalized concentrations of ice from EDC, and EDML also separated by time periods (Gabrielli et al., 2010; Wegner et al, 2012). b) Comparison of average acid leached and fully digested TYD ice. c) Comparison of average fully digested TYD ice to Ross Sea sector potential source area dust (Blakowski et al., In Press).

3.3 Sr and Nd isotopic compositions

We use the radiogenic isotopic composition of dust entrained in TYD ice to discern the shifts in provenance during the time period studied. The isotope variability in the glacial samples is large: $^{87}Sr/^{86}Sr$= 0.7052 to 0.7101 and ε_{Nd}= -3.5 to -0.9, whereas Holocene dust displays an even broader range: $^{87}Sr/^{86}Sr$= 0.7054 to 0.7163 and ε_{Nd}= -7.1 to -0.9. We observe significant variations in the ε_{Nd} compositions of the Holocene soluble fraction; the insoluble and soluble fractions from a single sample are not coupled and suggest that the variable soluble ε_{Nd} compositions are not a result of leaching from the insoluble fraction (Figure 3.4). The majority of soluble samples measure close to the established $^{87}Sr/^{86}Sr$ seawater composition of 0.70917 (Hodell et al., 1990) with the

exception of samples from ~4.7, 5.3, and 6.5 ka (0.705152, 0.705353, and 0.707023 respectively). Most of the insoluble samples possess a higher Sr radiogenic isotope composition than the water-soluble fraction (Figure 3.4).

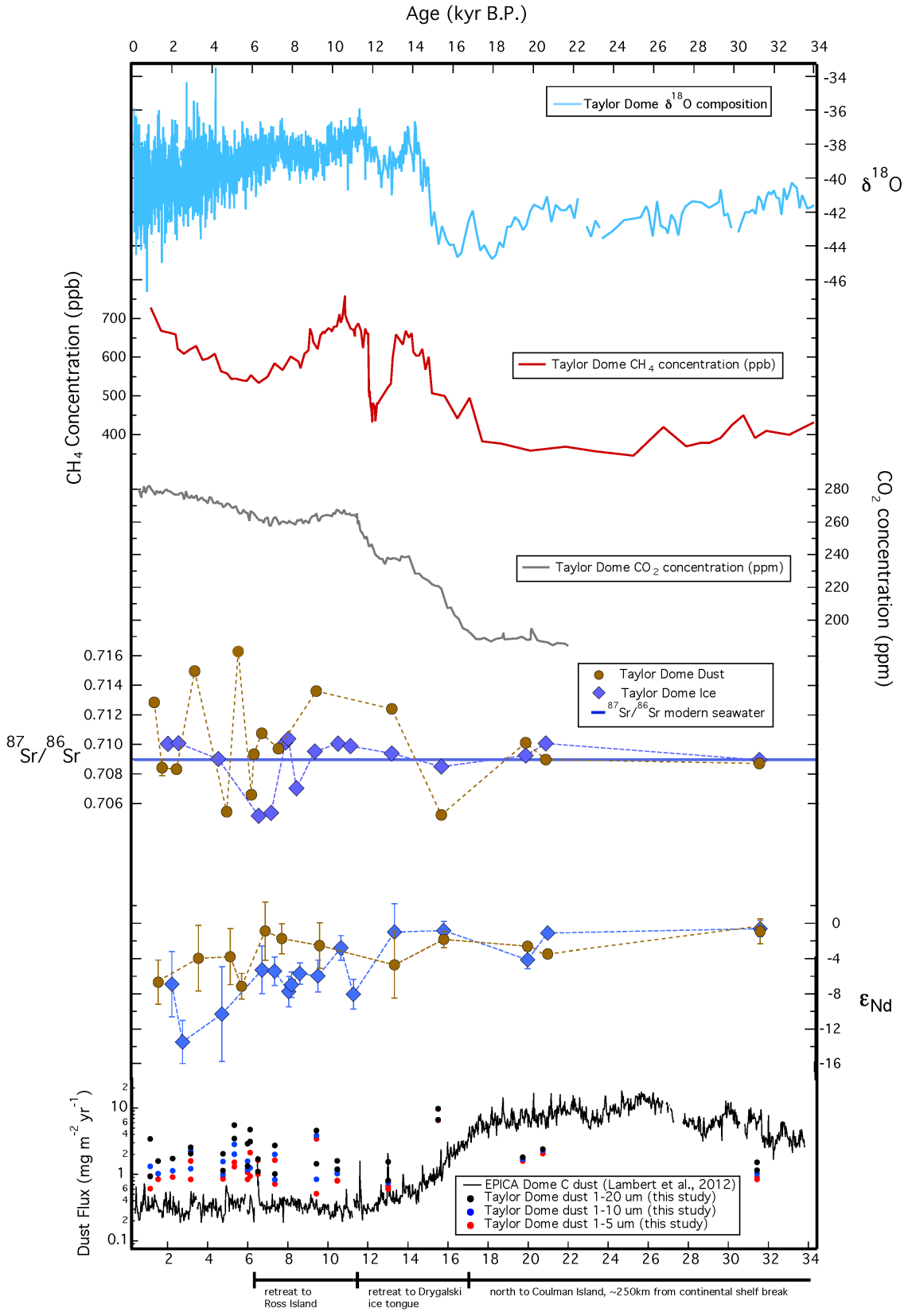
Age (kyr B.P.)
Taylor Dome δ18O composition
δ18O
Taylor Dome CH4 concentration (ppb)
CH4 Concentration (ppb)
Taylor Dome CO2 concentration (ppm)
CO2 concentration (ppm)
Taylor Dome Dust
Taylor Dome Ice
87Sr/86Sr modern seawater
87Sr/86Sr
εNd
Dust Flux (mg m-2 yr-1)
EPICA Dome C dust (Lambert et al., 2012)
Taylor Dome dust 1-20 um (this study)
Taylor Dome dust 1-10 um (this study)
Taylor Dome dust 1-5 um (this study)
retreat to Ross Island
retreat to Drygalski ice tongue
north to Coulman Island, ~250km from continental shelf break

Figure 3.4. Thirty-two-thousand-year climate history of the Ross Sector of East Antarctica. TYD ice core $\delta^{18}O$ isotope profile (blue line; (Steig, 2000)), CH_4 concentration (red line; (Brook et al., 2000)), CO_2 concentration (grey line; (Monnin et al., 2004)), Sr and Nd isotopic compositions (brown circles=dust fraction, blue diamonds=ice fraction) and the Sr isotopic composition of modern seawater (solid blue line) (Hodell et al., 1990). TYD dust flux record for three different size fractions (red circles=1-5 μm, blue circles=1-10 μm, and black circles=1-20 μm, this work) with EDC dust flux (black line;(Lambert et al., 2008)).

The TYD insoluble portion spans a broad range of Sr and Nd isotopic compositions (Figure 3.5). The majority of the Holocene samples are more radiogenic with respect to Sr (average Holocene=0.710573 versus average LGP=0.708257), and plot closer to the regional Ross Sea Region patterns (colored areas, Figure 3.5). However, at least 3 of the Holocene samples plot within the SSA source area. The glacial samples plot further away from the Ross Sea Region source area pattern (with the exception of a sample from ~13 ka, which may be a result of the deglacial transition), also observed in dust from a previously measured East Antarctic ice core (Delmonte et al., 2008; Delmonte et al., 2004a).

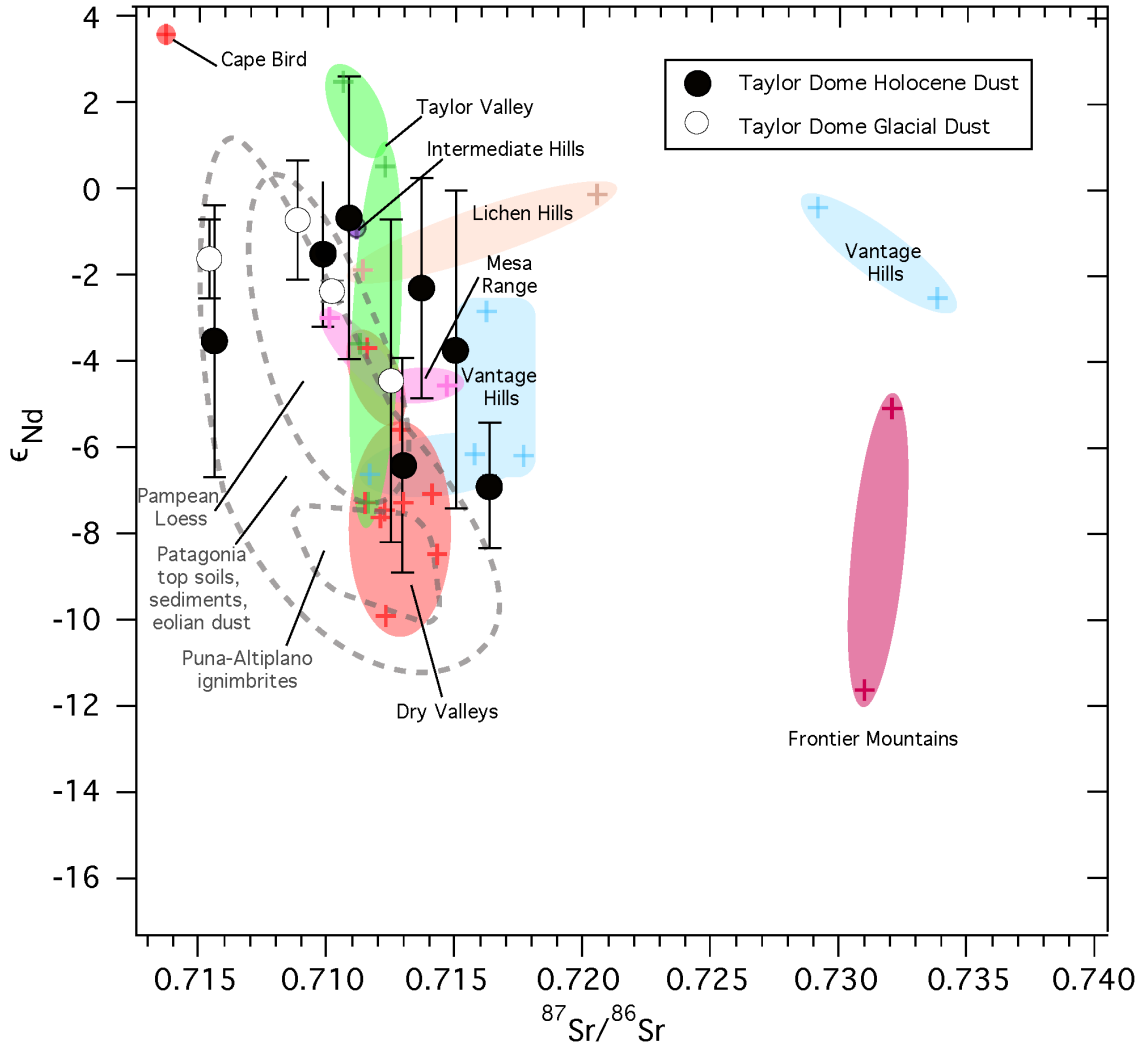

Figure 3.5. Radiogenic isotopic compositions of Taylor Dome ice core dust and regional Potential Source Areas. Sr and Nd isotopic compositions of Taylor Dome ice core Holocene (black circles) and Glacial dust (white circles) with regional Potential Source Areas plotted in various colors (colored crosses are individual data points) (Blakowski et al., In Press; Delmonte et al., 2013; Delmonte et al., 2010) and long range Potential Source Area of Southern South America plotted within dashed gray line (Delmonte et al., 2004a; Gaiero, 2007).

4. Discussion

4.1 Dust concentration, flux and size distribution: evidence of a changing regional climate

Long-term variations in dust concentration and flux have been noted in records from the EDC ice core from interior East Antarctica (Lambert et al., 2008). The EDC ice core records a drastic drop (an order of magnitude) in dust flux (Figure 3.4) and dust concentration (Figure 3.S2) following the termination of the LGP (Delmonte et al., 2004a). Similarly, the flux, concentration and size distribution of TYD ice core dust changes dramatically from the LGP to the Holocene, with larger dust particles more prevalent during the Holocene. The higher total Holocene dust flux was also observed in the Talos Dome ice core (Albani et al., 2012). This higher input of large dust particles suggests more local input of dust, which can be attributed to an alteration in storm trajectories and dominant weather pathways (Morse et al., 1998b). The ice-free terrains of Victorialand and the nearby Transantarctic Mountains during the last glacial period rule out the possibility of increased large dust particle concentration due to a reduction of land ice cover and resulting exposure of local dust sources (Delmonte et al., 2010).

The difference in dust flux between the TYD and EDC ice cores is significant (Figure 3.4). The overall trends of dust flux in both ice cores are similar: higher (lower) proportion of fine particle flux during LGP (Holocene), though the magnitude of difference is less in the TYD core most likely due to the proximity to unglaciated terrains. However, due to the discontinuous record of the TYD core,

it is difficult to speculate as to the underlying causes of the dust flux differences between the TYD and EDC ice cores.

The measurement of size variations of dust particles entrained in ice cores has proven useful for inferring changes in dust transport pathways and atmospheric circulation (Delmonte et al., 2004b). The modal diameter in the TYD glacial samples is ~2 μm, consistent with previous results obtained from another coastal East Antarctic ice core (Talos Dome) (Albani et al., 2012), as well as interior East Antarctic ice cores (Vostok, EDC) (Delmonte et al., 2004a; Petit et al., 1999). The small dust diameters observed in ice cores across East Antarctica during the LGP are indicative of long-range sourced dust that was most likely deposited congruently throughout East Antarctica (Albani et al., 2012; Delmonte et al., 2004a; Petit et al., 1999).

The modal diameter of Holocene dust in the TYD ice core is larger at ~3 μm, and the samples are not log-normally distributed—most likely due to poor size-sorting during transport and deposition. In contrast, ice cores from interior East Antarctica (Dome B, Komsomolskaia, EDC) during the time period of 12 ka have smaller average dust particle diameters ranging from 1.8, 1.9, and 2.2 μm respectively (Delmonte et al., 2004b). Talos Dome, a coastal ice core, is characterized by poor size sorting during the Holocene and the presence of dust particles in the size range of 5-10 μm is strong evidence of local input (Albani et al., 2012). Analysis of the TYD dust size distribution in three size fractions (1-5,

1-10, and 1-20 μm respectively) highlights the shift in average dust particle diameter between the LGP and the Holocene (Figure 3.S2).

4.2 Rare Earth Element signatures of Taylor Dome ice

The REE patterns normalized to upper continental crustal abundance are consistent with input of dust from continental sources (Figure 3.5a). The normalization is applied to the samples and results in a characteristic REE profile with a clear positive Eu anomaly for Holocene samples (Figure 3.3). Any deviations from this pattern would be indicative of a change in source area, which is best determined by comparing these results to the REE profiles of soil and rock from hypothesized source areas (see Figure 3.3c).

The REE patterns (both the acid leached and fully digested samples) for the TYD ice core display a similar, temporally unchanging profile throughout the LGP. There is a distinct change (positive Eu anomaly) for samples younger than ~15.5 ka (sample 376), although a Holocene sample (~6.1 ka, sample 299) displays a pattern similar to LGP samples (Figure 3.3). The positive Eu anomaly observed in the TYD Holocene samples (Figure 3.3a, b) is also observed in young volcanic PSA dust from Patagonia (Gaiero, 2004), however it is unlikely that the TYD Holocene dust is originating from Patagonia as the isotopic compositions are not in agreement (Figure 3.S7). The comparison of the results of the two REE methods is described below.

4.2.1 Comparison of traditional acid leaching to full acid digestion

The results of different sample methodology for REE and trace element analysis is an important topic still under consideration (Koffman et al., 2014; Rhodes et al., 2011). Previous work highlighted the importance of sample methodology upon the measured trace element and REE concentrations; different laboratories may use varying methods for sample preparation and subsequent analysis which may result in incorrect or misleading measured concentrations due to incongruent elemental dissolution of trace and REEs (Koffman et al., 2014; Rhodes et al., 2011; Uglietti et al., 2014). Previous work using three separate preparations (acid leached, pre-filtered then acid leached, and full digestion) of Antarctic ice-core samples to determine REE concentrations demonstrated that glacial-interglacial variations of the REE patterns emerge and are significant if the method adopted is consistently used for all the samples analyzed (Gabrielli, 2010). In our study, the REE patterns of the acid leached and fully digested TYD samples vary from one another: the LREE patterns in the higher concentrated samples (LGP) are distinctively different, whereas the lower concentrated samples (Holocene) all display the positive Eu anomaly (Figure 3.3b).

When using the trace element concentrations to discern changes in atmospheric trace elements due to anthropogenic pollution and/or land use changes, the sample preparation method becomes more important for comparing ice core

records (Koffman et al., 2014; Uglietti et al., 2014). The results of these studies emphasize the importance of allowing melted acidified ice core samples to sit for at least one month prior to analysis, and that incomplete dissolution of minerals and/or incongruent leaching is an issue that can be resolved by full acid digestion using HF. To discern the effects of acid leaching versus full acid digestions on our TYD ice core samples we used both techniques (Figure 3.3b). Our results demonstrate that full acid digestion results in higher REE concentrations than the acid leaching method by nearly one order of magnitude (as described above in methods), and comparison of both techniques yielded varying REE concentration patterns (Figure 3.3), which also occurred in earlier work measuring trace element concentration (Koffman et al., 2014). The full digestion Holocene TYD samples all display a unique Eu enrichment anomaly, with the exception of the sample from the time period of ~6.1 ka (sample 299). The fully digested LGP TYD samples do not have this positive Eu anomaly, supporting the hypothesis that dust deposited on TYD during the dust origin during the LGP is different than during the Holocene. Prior work comparing the acid leaching method to the full acid digestion method determined that the traditional acid leaching method overestimates the LREE concentrations with respect to the MREE and HREE concentrations (Gabrielli, 2010). In contrast, the leached TYD samples possess lower normalized La concentrations compared to the fully digested samples (Figure 3.3b). The results presented here demonstrate that the sample methodology of traditional acid leaching versus full acid digestion produces distinctly different REE concentrations.

4.2.2 REE comparison of Taylor Dome dust to PSAs

Reconstruction of dust sources and pathways through time is possible through the comparison of REE patterns in ice cores to those measured in PSAs (Wegner et al., 2012). We compare the fully digested acid leach data of TYD dust to Ross Sea sector PSA dust samples as both sets of data were processed the same. The REE concentrations of TYD LGP samples are distinctly different from the REE patterns of the Ross Sea sector PSA samples (Figure 3.3c). The Holocene TYD ice has a significant positive Eu anomaly not observed in the Ross Sea sector PSA samples; however, both sets of samples have a similar HREE pattern with the exception of the sample from ~6.1 ka (sample 299) (Figure 3.3c). Based on the REE pattern during the Holocene, we hypothesize that the source of dust to TYD during this time period is a consistent mix of dust from PSAs in the Ross Sea Sector and a small but constant input of long-range transported dust. The REE pattern of dust deposited in Antarctic ice throughout the last deglaciation suggests an input of a mixed long-range transported dust or input from a baseline source such as SSA (Gabrielli, 2010; Wegner et al., 2012). The Holocene REE patterns of EDC and EDML ice differs significantly (high enrichment in Gd) from those of the Ross Sea sector PSAs and the Holocene TYD samples, implying that the source of dust to East Antarctica during the Holocene changes based upon the proximity to the coast (Bertler and al., 2005; Delmonte et al., 2013) (Figure 3.3c). The Holocene TYD REE pattern remains relatively uniform and constant, and may be a reflection of dust input from a local

unrecognized (unmeasured) source. The current Holocene storm trajectory approaching TYD from the southeast crosses the Royal Society Range, which has not been sampled for chemical characterization of the PSA and therefore cannot be ruled out as a potential contributor of dust to TYD (Figure 3.1).

We evaluate the possibility of dust contribution from both the Ross Sea sector and SSA PSAs with a simple two-component mixing model of REE concentrations in increments of 10% (i.e. 90% SSA dust input and 10% Ross Sea sector dust input) (Figure 3.S5). The HREE enrichment of Ross Sea sector and SSA PSAs is not observed in the average measured Holocene REE concentrations or the modeled mixtures of SSA and Ross Sea sector REE concentrations (Figure 3.S5). The discrepancy between the observed average TYD Holocene REE concentrations and the PSAs from the Ross Sea sector and SSA may be attributed to dust input from an uncharacterized source or fractionation of REEs during long-range transport. Changes in the mineral composition may occur during eolian transport due to gravitational sorting: heavy minerals settle out of the atmosphere closer to the source, leaving behind suspended particles depleted in HREE, Zr and Hf (Aarons et al., 2013; Gaiero, 2007).

4.2.3 REE concentration of TYD soluble portion

As a first hypothesis, the higher REE concentrations observed during the LGP compared to the Holocene may be attributed to the increased formation, transport and deposition of sea-salt aerosol originating from sea ice, as is the

case for other Antarctic ice core records (Petit et al., 1999; Wolff, 2006). We would expect the REE pattern of the soluble LGP samples to most closely resemble the REE pattern of Antarctic seawater, represented by a solid black line in Figure 3.6. This is not the case. So it is possible that aerosol mineral dust and unbufferable minerals smaller than 0.2 μm may be present in the soluble portion of the TYD ice core (as the melted ice core was filtered to a size of 0.2 μm) along with oceanic derived aerosols (dissolved sea salt), and leached elements from the dust fraction during transport and ice core sample processing (Lupker et al., 2010). To explore the relative contribution of sea salt versus mineral dust to the soluble REE patterns observed in the TYD ice core record, a two-component mixing model in increments of 10% (i.e. 90% mineral dust and 10% sea salt contribution), is utilized (Figure 3.S6). This two-component model does not produce the measured REE concentration pattern, which suggests that other processes are occurring during either transport or ice formation that may fractionate REE patterns. Further, this modeling confirms that leaching from mineral dust is unlikely after deposition.

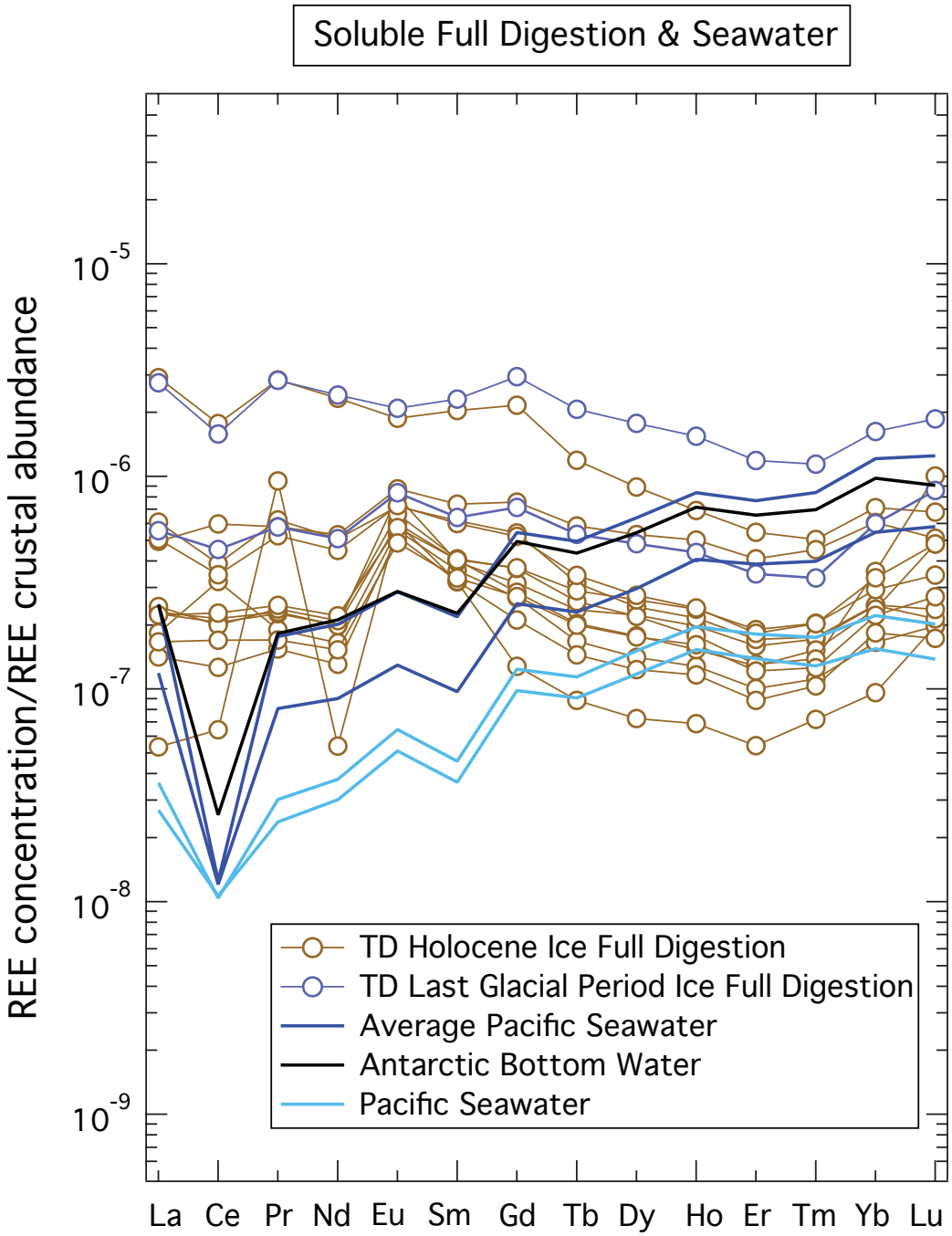

Figure 3.6. Rare earth element concentrations of Taylor Dome ice soluble portion (full digestion) in comparison to REE concentrations in seawater (Kawabe et al., 1998). Hollow brown and blue circles are Holocene and Last Glacial Period fully digested samples. Solid dark blue, black and light blue lines are average Pacific seawater, Antarctic bottom water, and unique Pacific seawater samples respectively (Kawabe et al., 1998).

4.3 Isotopic signature of Taylor Dome and East Antarctic dust

Previous work utilizing Sr isotopes as a tracer of aerosol mineral dust highlighted the importance of separating soluble and insoluble portions of samples to accurately interpret dust provenance (Aarons et al., 2013). The measured trace element (TE) concentrations of TYD ice are another indicator of changes in sea salt contribution and we use the Na/Sr ratio to serve as a proxy (Table 3.S3). The average insoluble and soluble TYD Na/Sr ratios are 191 and 1034 respectively (Figure 3.S3). The average upper continental crust and seawater Na/Sr ratio is 81 (Wedepohl, 1995) and 1358 (Riley and Tongudai, 1967) respectively, which supports the conclusion that the higher soluble Na/Sr ratio in the TYD samples is attributable to sea salt acting as the primary constituent (Figure 3.S3). It is likely that sea salt originating from nearby seasonal sea ice in the Ross Sea is a large contributor to the soluble Sr in the TYD ice, and we therefore interpret our radiogenic isotope data separately as the soluble and insoluble portions.

4.3.1 Radiogenic isotopic composition of soluble portion

The water-soluble portions of the TYD ice core plot close to the modern $^{87}Sr/^{86}Sr$ composition of seawater, and the highest variability occurs between ~8-4 ka (Figure 3.4). It is unclear why three water-soluble samples are not in agreement with the established $^{87}Sr/^{86}Sr$ composition of seawater (0.70917, Hodell et al., 1990). However, the variable ε_{Nd} compositions of Holocene soluble samples

could be attributed to oceanic processes, the Southern Ocean ε_{Nd} composition close to the Ross Sea ranges from -11.3 to -8.4 (Albarède et al., 1997). Aerosols originating from seasonal sea ice with frost flowers during warmer, interglacial conditions may cause the transition from uniform to variable ε_{Nd} values (Figure 3.4).

4.3.2 Radiogenic isotopic composition of insoluble portion

The Sr and Nd isotopic compositions of TYD dust indicate a shift provenance from a relatively constant long-range input to a more variable proximal source following the deglaciation, as the Holocene isotopic compositions trend more towards the PSAs from the Ross Sea sector. In general, the Holocene samples span a larger range of $^{87}Sr/^{86}Sr$ and ε_{Nd} isotope values, and appear to be comprised of a combination of Ross Sea sector PSAs. The hypothesized Holocene storm trajectory crosses the Royal Society Range (Figure 3.1), and it has not been sampled or analyzed for $^{87}Sr/^{86}Sr$ and ε_{Nd} isotopic compositions. The unsampled and unmeasured Royal Society Range along with additional unidentified proximal sources cannot be ruled out as the predominant source of Holocene dust. The dust from the LGP however, appears to be less radiogenic with respect to Nd, and lies closer to the SSA source area (Basile et al., 1997) as concluded by previous studies (Delmonte et al., 2010; Delmonte et al., 2004a).

4.3.3 Synthesis of physical and chemical characteristics of mineral dust

The dust size distribution in TYD ice transitions from fine to coarse during the last deglaciation, signifying a transition from distal to local dust sources. The REE concentrations clearly distinguish different dust sources during the LGP and Holocene, and the presence of a distinct positive Eu anomaly in almost all of the Holocene samples suggest that the interglacial samples are originating from a similar source area with congruent bedrock geology. Finally, the radiogenic isotope measurements also imply that the dust sources to TYD during the Holocene are similar to local sources (Figure 3.5), and are most likely a combination between isotopically characterized and uncharacterized areas in the Ross Sea Sector. During the LGP we observe isotopic compositions similar to dust from SSA, which supports a shift from long-range transported dust to a local source. The change in dust sources may be attributed to a change of dominant storm trajectories, and is consistent with the hypothesis that the moisture-bearing storms approaching TYD have shifted from the north to the southeast following the last deglaciation.

4.3.4 Retreat of Ross ice shelf reflected in dust record

Glaciological studies (Hinkley and Matsumoto, 2001; Morse et al., 1998a) suggest that the Ross Ice Shelf retreat discernable in paleo-records caused a shift in the local storm trajectories and the composition of aerosols delivered to the region. Geochemical records of spelothems in northern Europe provide evidence for movement in predominant storm trajectories as a result of shifting Late-Pleistocene Northern Hemisphere ice shelf extents (Luetscher et al., 2015),

thereby confirming that geochemical evaluation of paleoclimate proxies may reveal small-scale shifts in climate (e.g. storm tracks). Major and rare earth element concentrations of TYD ice indicate that total impurities were at their highest and dust deposition was greater than sea salt during the LGP (Hinkley and Matsumoto, 2001), perhaps a result of increased dust availability in South America (Basile et al., 1997; Delmonte et al., 2010; Delmonte et al., 2004a; Gabrielli, 2010; Wegner et al., 2012). The sea salt concentration increased in the dust-salt mixture at the termination of the LGP (Hinkley and Matsumoto, 2001), suggesting an increase in new sea ice (covered in brine and frost flowers) extent but unchanged wind strength and patterns as the dust composition remained uniform. A reversal in the dust-sea salt concentrations indicates that the sea ice extent briefly returned to LGP conditions between 10-11 ka, before a final retreat and subsequent change to sea-salt dominance of aerosol composition. Synthesizing the work of Morse et al. (1998) and Hinkley and Matsumoto (2001) confirms that the Ross Ice Shelf retreat had a profound impact on the local climate – changing both storm trajectories and the composition of aerosols deposited on the local surroundings, which is supported by the data presented here.

The broad range of radiogenic isotopic compositions of dust from Holocene ice demonstrates the variable sources of dust to TYD during this time period. It is possible that the sources of dust to TYD during the LGP originated from more

than one distal source, however it appears that during the Holocene the dust provenance and dust transport pathways are more variable.

5. Conclusions

We present geochemical and physical measurements of dust in the TYD ice core record spanning the LGP, the deglaciation and the Holocene. In addition to providing the first high time resolution radiogenic isotope compositions of dust in an East Antarctic ice core, we also utilize and compare two methods of REE sample processing (acid leach and full digest). The results presented here demonstrate that the two sample methodologies produce distinctly different REE concentrations, which has implications for studies comparing and contrasting REE concentrations in ice core records. The geographic location of TYD relative to the Ross Ice Shelf provides an ideal study site to explore local shifts in storm trajectories related to the rapid retreat of the Ross Ice Shelf during the last deglaciation. Our data supports an alteration in local circulation following the termination of the LGP and the subsequent transition into the Holocene as evidenced by the shifts in dust particle diameters, REE concentrations, and radiogenic isotope compositions. The systematic shift in radiogenic isotope composition combined with an increase in dust particle diameter during the Holocene suggests that the dust transported to Taylor Dome is originating from a local source. These observations are consistent with previous studies of a coastal East Antarctic ice core (Albani et al., 2012; Delmonte et al., 2010). We

attribute this modification in dominant weather pathways to the retreat of the Ross Ice Shelf, as first proposed by Morse et al (1998).

6. References

Aarons, S.M., Aciego, S.M., Gleason, J.D., 2013. Variable Hf-Sr-Nd radiogenic isotopic compositions in a Saharan dust storm over the Atlantic: Implications for dust flux to oceans, ice sheets and the terrestrial biosphere. Chemical Geology 349-350, 18-26.

Aciego, S.M., Bourdon, B., Lupker, M., Rickli, J., 2009. A new procedure for separating and measuring radiogenic isotopes (U, Th, Pa, Ra, Sr, Nd, Hf) in ice cores. Chemical Geology 266, 194-204.

Ahn, J., Brook, E.J., 2007. Atmospheric CO2 and climate from 65 to 30 ka B.P. Geophysical Research Letters 34.

Albani, S., Delmonte, B., Maggi, V., Baroni, C., Petit, J.R., Stenni, B., Mazzola, C., Frezzotti, M., 2012. Interpreting last glacial to Holocene dust changes at Talos Dome (East Antarctica): implications for atmospheric variations from regional to hemispheric scales. Climate of the Past 8, 741-750.

Albarède, F., Goldstein, S.L., Dautel, D., 1997. The neodymium isotopic composition of manganese nodules from the Southern and Indian oceans, the global oceanic nedymium budget, and their bearing on deep ocean circulation. Geochimica Et Cosmochimica Acta 61, 1277-1291.

Anderson, J.B., Shipp, S.S., Bartek, L.R., Reid, D.E., 1992. Evidence for a grounded ice sheet on the Ross Sea continental shelf during the late Pleistocene and preliminary paleodrainage reconstruction. American Geophysical Union, Washington D.C.

Baggenstos, D., 2015. Taylor Glacier as an archive of ancient ice for large-volume samples: Chronology, gases, dust, and climate, Earth Sciences. University of California, San Diego, Ann Arbor, MI, p. 148.

Baroni, C., Fasano, F., Giorgetti, G., Salvatore, M.C., Ribecai, C., 2008. The Ricker Hills Tillite provides evidence of Oligocene warm-based glaciation in Victoria Land, Antarctica. Global and Planetary Change 60, 457-470.

Basile, I., Grousset, F.E., Revel, M., Petit, J.R., Biscaye, P.E., Barkov, N.I., 1997. Patagonian origin of glacial dust deposited in East Antarctica (Vostok and Dome C) during glacial stages 2, 4 and 6. Earth and Planetary Science Letters 146, 573-589.

Beghin, P., Charbit, S., Dumas, C., Kageyama, M., Roche, D.M., Ritz, C., 2014. Interdependence of the growth of the Northern Hemisphere ice sheets during the last glaciation: the role of atmospheric circulation. Climate of the Past 10, 345-358.

Bertler, N., al., e., 2005. Snow Chemistry across Antarctica. Annals of Glaciology 41, 167-179.

Blakowski, M.A., Aciego, S.M., Delmonte, B., Baroni, C., Salvatore, M.C., Sims, K.W.W., In Press. Sr-Nd-Hf isotope characterization of dust source areas in Victoria Land and the McMurdo Sound sector of Antarctica. Quaternary Science Reviews.

Boutron, C.F., Patterson, C.C., Barkov, N.I. , 1990. The occurrence of zinc in Antarctic ancient ice and recent snow. Earth and Planetary Science Letters 101, 248-259.
Brook, E.J., Harder, S., Severinghaus, J.P., Steig, E.J., Sucher, C.M., 2000. On the origin and timing of rapid changes in atmospheric methane during the last glacial period. Global Biogeochemical Cycles 14, 559-572.
Cook, K.H., Held, I.M., 1988. Stationary waves of the ice age climate. Journal of Climate 1, 807-819.
Delmonte, B., Andersson, P., Hansson, M., Schoberg, H., Petit, J.-R., Basile-Doelsch, I., Maggi, V., 2008. Aeolian dust in East Antarctica (EPICA - Dome C and Vostok): Provenance during glacial ages over the last 800 kyr. Geophysical Research Letters 35.
Delmonte, B., Baroni, C., Andersson, P.S., Narcisi, B., Salvatore, M.C., Petit, J.-R., Scarchilli, C., Frezzotti, M., Albani, S., Maggi, V., 2013. Modern and Holocene aeolian dust variability from Talos Dome (Northern Victoria Land) to the interior of the Antarctic ice sheet. Quaternary Science Reviews 64, 76-89.
Delmonte, B., Baroni, C., Andersson, P.S., Schoberg, H., Hansson, M., Aciego, S., Petit, J.R., Albani, S., Mazzola, C., Maggi, V., Frezzotti, M., 2010. Aeolian dust in the Talos Dome ice core (East Antarctica, Pacific/Ross Sea sector): Victoria Land versus remote sources over the last two climate cycles. Journal of Quaternary Science 25, 1327-1337.
Delmonte, B., Basile-Doelsch, I., Petit, J., Maggi, V., Revel-Rolland, M., Michard, A., Jagoutz, E., Grousset, F., 2004a. Comparing the EPICA and Vostok dust records during the last 220,000 years: stratigraphical correlation and provenance in glacial periods. Earth-Science Reviews 66, 63-87.
Delmonte, B., Petit, J.R., Andersen, K.K., Basile-Doelsch, I., Maggi, V., Ya Lipenkov, V., 2004b. Dust size evidence for opposite regional atmospheric circulation changes over east Antarctica during the last climatic transition. Climate Dynamics 23, 427-438.
Delmonte, B., Petit, J.R., Basile-Doelsch, I., Jagoutz, E., Maggi, V., 2007. Late quaternary interglacials in East Antarctica from ice-core dust records. Developments in Quaternary Sciences 7, 53-73.
Delmonte, B., Petit, J.R., Maggi, V., 2002. Glacial to Holocene implications of the new 27000-year dust record from the EPICA Dome C (East Antarctica) ice core. Climate Dynamics 18, 647-660.
Francis, J.A., Chan, W., Leathers, D.J., Miller, J.R., Veron, D.E., 2009. Winter Northern Hemisphere weather patterns remember summer Arctic sea-ice extent. Geophys. Res. Lett. 36.
Gabrielli, P., Barbante, C., Turetta, C., Marteel, A., Boutron, C., Cozzi, G., Cairns, W., Ferrari, C., Cescon, P., 2006. Direct determination of rare earth elements at the subpicogram per gram level in antarctic ice by ICP-SFMS using a desolvation system. Analytical Chemistry.
Gabrielli, P., et al., 2010. A major glacial-interglacial change in aeolian dust composition inferred from Rare Earth Elements in Antarctic ice. Quaternary Science Reviews 29, 265-273.

Gaiero, D.M., 2004. The signature of river-and wind-borne materials exported from Patagonia to the southern latitudes: A view from REEs and implications for paleoclimatic interpretations. Earth and Planetary Science Letters 219, 357-376.
Gaiero, D.M., 2007. Dust provenance in Antarctic ice during glacial periods: from where in southern South America? Geophysical Research Letters 34.
Grootes, P.M., Steig, E.J., Stuiver, M., Waddington, E.D., Morse, D.L., 1994. A new ice core record from Taylor Dome, Antarctica. Eos, Transactions, American Geophysical Union 75, 225.
Grousset, F.E., Biscaye, P.E., 2005. Tracing dust sources and transport patterns using Sr, Nd and Pb isotopes. Chemical Geology 222, 149-167.
Hall, N.M.J., Valdes, P.J., Dong, B., 1996. The Maintenance of the Last Great Ice Sheets: A UGAMP GCM Study. Journal of Climate 9, 1004-1019.
Hammer, C., Clausen, H., Dansgaard, W., Neftel, A., Kristinsdottir, P., Johnson, E., 1985. Continuous impurity analysis along the Dye-3 deep core. Geophys. Monog. Series. 33, 90-94.
Harris, J.M., 1992. An analysis of 5 day midtropospheric flow patterns for the South Pole. Tellus Series B 20, 115-120.
Hinkley, T.K., Matsumoto, A., 2001. Atmospheric regime of dust and salt through 75,000 years of Taylor Dome ice core: Refinement by measurement of major, minor, and trace metal suites. Journal of Geophysical Research 106, 18,487-418,493.
Hodell, D.A., Mead, G.A., Mueller, P.A., 1990. Variation in the strontium isotopic composition of seawater (8 Ma to present): Implications for chemical weathering rates and dissolved fluxes to the oceans. Chemical Geology 80, 291-307.
Jouzel, J., Vaikmae, R., Petit, J.R., Martin, M., Duclos, Y., Stievenard, M., Lorius, C., Toots, M., Melieres, M.A., Burckle, L.H., Barkov, N.I., Kotyakov, V.M., 1995. The two-step shape and timing of the last deglaciation in Antarctica. Climate Dynamics 11, 151-161.
Jweda, J., Bolge, L., Class, C., Goldstein, S.L., 2015. High Precision Sr-Nd-Hf-Pb Isotopic Compositions of USGS Reference Material BCR-2. Geostandards and Geoanalytical Research.
Kageyama, M., Valdes, P.J., 2000. Impact of the North American ice-sheet orography on the Last Glacial Maximum eddies and snowfall. Geophysical Research Letters 27, 1515.
Kawabe, I., Toriumi, T., Ohta, A., Miura, N., 1998. Monoisotopic REE abundances in seawater and the origin of seawater tetrad effect. Geochemical Journal 32, 213-229.
Koffman, B.G., Handley, M.J., Osterberg, E.C., Wells, M.L., Kreutz, K.J., 2014. Dependence of ice-core relative trace-element concentration on acidification. Journal of Glaciology 60, 103-112.
Koornneef, J.M., Bouman, C., Schwieters, J.B., Davies, G.R., 2014. Measurement of small ion beams by thermal ionisation mass spectrometry using new 10^13 Ohm resistors. Analytica Chimica Acta 819, 49-55.
Laîné, A., Kageyama, M., Salas-Mélia, D., Voldoire, A., Rivière, G., Ramstein, G., Planton, S., Tyteca, S., Peterschmitt, J.Y., 2008. Northern hemisphere storm tracks during the last glacial maximum in the PMIP2 ocean-atmosphere coupled

models: energetic study, seasonal cycle, precipitation. Climate Dynamics 32, 593-614.
Lambert, F., Delmonte, B., Petit, J.R., Bigler, M., Kaufmann, P.R., Hutterli, M.A., Stocker, T.F., Ruth, U., Steffensen, J.P., Maggi, V., 2008. Dust-climate couplings over the past 800,000 years from the EPICA Dome C ice core. Nature 452, 616-619.
Liakka, J., Nilsson, J., 2010. The impact of topographically forced stationary waves on local ice-sheet climate. Journal of Glaciology 56, 534-544.
Licht, K.J., Jennings, A.E., Andrews, J.T., Williams, K.M., 1996. Chronology of late Wisconsin ice retreat from the western Ross Sea, Antarctica. Geology 24, 223-226.
Luetscher, M., Boch, R., Sodemann, H., Spotl, C., Cheng, H., Edwards, R.L., Frisia, S., Hof, F., Muller, W., 2015. North Atlantic storm track changes during the Last Glacial Maximum recorded by Alpine spelothems. Nature Communications 6.
Lupker, M., Aciego, S.M., Bourdon, B., Schwander, J., Stocker, T.F., 2010. Isotopic tracing (Sr, Nd, U and Hf) of continental and marine aerosols in an 18th century section of the Dye-3 ice core (Greenland). Earth and Planetary Science Letters 295, 277-286.
McGee, D., Broecker, W.S., Winckler, G., 2010. Gustiness: The driver of glacial dustiness? Quaternary Science Reviews 29, 2340-2350.
Monnin, E., Steig, E.J., Siegenthaler, U., Kawamura, K., Schwander, J., Stauffer, B., Stocker, T.F., Morse, D.L., Barnola, J.M., Bellier, B., Raynaud, D., Fischer, H., 2004. Evidence for substantial accumulation rate variability in Antarctica during the Holocene, through synchronization of CO2 in the Taylor Dome, Dome C and DML ice cores. Earth and Planetary Science Letters 224, 45-54.
Morse, D.L., 1997. Glacier Geophysics at Taylor Dome, Antarctica. University of Washington.
Morse, D.L., Waddington, E.D., Steig, E.J., 1998a. Ice age storm trajectories inferred from radar stratigraphy at Taylor Dome, Antarctica. Geophysical Research Letters 25, 3383-3386.
Morse, D.L., Waddington, E.D., Steig, E.J., 1998b. Ice age storm trajectories inferred from radar stratigraphy at Taylor Dome, Antarctica. Geophysical Research Letters 25, 3383-3386.
Petit, J.R., Jouzel, J., Raynaud, D., Barkov, N.I., Barnola, J.-M., Basile, I., Bender, M., Chappellaz, J., Davis, M., Delaygue, G., Delmotte, M., Kotlyakov, V.M., Legrand, M., Lipenkov, V.Y., Lorius, C., Pepin, L., Ritz, C., Saltzman, E., Stievenard, M., 1999. Climate and atmospheric history of the past 420,000 years from the Vostok ice core, Antarctica. Nature 399, 429-436.
Rhodes, R.H., Baker, J.A., Millet, M.-A., Bertler, N.A.N., 2011. Experimental investigation of the effects of mineral dust on the reproducibility and accuracy of ice core trace element analyses. Chemical Geology 286, 207-221.
Riley, J.P., Tongudai, M., 1967. The major cation/chlorinity ratios in sea water. Chemical Geology 2, 263-269.
Rivière, G., Laîné, A., Lapeyre, G., Salas-Mélia, D., Kageyama, M., 2010. Links between Rossby wave breaking and the North Atlantic Oscillation-Arctic

Oscillation in present-day and Last Glacial Maximum climate simulations. Journal of Climate 23, 2987-3008.
Steig, E.J., et al., 2000. Wisconsinan and Holocene climate history from an ice core at Taylor Dome, western Ross Embayment, Antarctica. Geographical Annals 82A, 213-235.
Stump, E., Fitzgerald, P.G., 1992. Episodic uplift of the Transantarctic Mountains. Geology 20, 161-164.
Uglietti, C., Gabrielli, P., Olesik, J.W., Lutton, A., Thompson, L.G., 2014. Large variability of trace element mass fractions determined by ICP-SFMS in ice core samples from worldwide high altitude glaciers. Applied Geochemistry 47, 109-121.
Vihma, T., 2014. Effects of Arctic Sea Ice Decline on Weather and Climate: A Review. Survey of Geophysics 35, 1175-1214.
Wedepohl, K.H., 1995. The composition of the continental crust. Geochimica Et Cosmochimica Acta 59, 1217-1232.
Wegner, A., Gabrielli, P., Wilhelms-Dick, D., Ruth, U., Kriews, M., De Deckker, P., Barbante, C., Cozzi, G., Delmonte, B., Fischer, H., 2012. Change in dust variability in the Atlantic sector of Antarctica at the end of the last deglaciation. Climate of the Past 8, 135-147.
Wolff, E.W., et al., 2006. Southern Ocean sea ice, DMS production and iron flux over the last eight glacial cycles. Nature 440, 491-496.
Wolff, E.W., Fischer, H., Fundel, F., Ruth, U., Twarloh, B., Littot, G.C., Mulvaney, R., Rothlisberger, R., de Angelis, M., Boutron, C.F., Hansson, M., Jonsell, U., Hutterli, M.A., Lambert, F., Kaufmann, P., Stauffer, B., Stocker, T.F., Steffensen, J.P., Bigler, M., Siggaard-Andersen, M.L., Udisti, R., Becagli, S., Castellano, E., Severi, M., Wagenbach, D., Barbante, C., Gabrielli, P., Gaspari, V., 2006. Southern Ocean sea-ice extent, productivity and iron flux over the past eight glacial cycles. Nature 440, 491-496.

7. Supplementary Materials

7.1. Introduction

This supporting information file contains additional figures describing the physical and chemical characteristics of the Taylor Dome (TYD) samples measured in this study, a mixing model describing potential contributions of Ross Sea Sector potential source area dust and Southern South America potential source area dust compared to the average rare earth element (REE) composition of Holocene dust in the TYD ice core, and a mixing model describing potential contributions of Antarctic Bottom Water (AABW) and mineral dust to the observed REE composition of a single sample (366) with a brief description of the model. Figure 3.S1 displays the dust size distribution and concentration data for each sample, Figure 3.S2 is the dust concentration of the TYD ice core along with Talos Dome and EPICA Dome C ice core records, Figure 3.S3 is the Na/Sr ratio with respect to age, Figure 3.S4 compares the soluble and insoluble rare earth element concentrations of fully digested samples, Figure 3.S5 is a simple two-component mixing model of REE concentrations of a combined input of dust from the Ross Sea Sector and Southern South America, Figure 3.S6 is the modeled REE concentration (normalized to mean crustal abundance) of one sample using a two-component mixing model, and Figure 3.S7 is the strontium and neodymium isotopic compositions of potential source areas of dust in the Southern Hemisphere.

Table 3.S1 contains the dust concentration and size distribution data, Table 3.S2 is the rare earth element concentrations, Table 3.S3 is the sodium and strontium

trace element concentrations, and table 3.S4 is the detailed sample information regarding the Ross Sea Sector potential source area dust discussed in this study.

7.2 Supporting Results

To evaluate the possibility of combined dust input from the Ross Sea Sector and Southern South America, we use a simple two-component mixing model of REE concentrations in increments of 10% (i.e. 90% Southern South America dust input and 10% Ross Sea Sector dust input) (Figure 3.S5). We compare the modeled results to the average TYD Holocene dust in an attempt to identify the relative contribution of dust from these source areas. The discrepancy between the observed average TYD Holocene dust and the modeled input from the two potential source areas of dust can be a result of dust input from an uncharacterized source area or the fractionation of REEs during long-range atmospheric transport.

To explore the relative contribution of sea salt versus mineral dust to the soluble REE patterns observed in the TYD ice core record, a simple two-component mixing model is utilized (Figure 3.S6). We calculated the relative contribution of AABW and mineral dust leaching to the REE composition of the soluble portion of samples in increments of 10% (i.e. 10% AABW contribution and 90% mineral dust contribution). It is apparent that the REE concentration cannot be modeled using a two-component mixing (Figure 3.S6), suggesting that another more

complex process is occurring during either transport or ice formation to cause the observed REE patterns, or the difference in REE patterns between the TYD soluble portion and seawater implies that the sources of REE to Antarctic coastal regions are mixed. The two-component mixing model confirms that leaching from mineral dust is unlikely after deposition.

7.2.1 Tables

Sample	Top Depth (m)	Ice Age (ka)	Dust concentration 1-5 micron (ppb)	Dust concentration 1-10 micron (ppb)	Dust concentration 1-20 micron (ppb)
113a	113.12	1.12	9.335	14.185	14.185
136a	113.12	1.12	14.455	20.215	52.185
136b	136.12	1.52	13.64	16.545	25.54
176a	176.1	2.24	-	-	-
176b	176.1	2.24	15	18.68	28.615
208a	208.13	3.15	26.225	37.315	42.15
208b	208.13	3.15	13.885	20.045	33.945
266a	264.8	4.76	13.6	15.825	18.155
266b	264.8	4.76	14.33	24.84	32.39
281a	279.48	5.33	20.825	31.99	55.045
281b	279.48	5.33	24.14	45.1	87.94
296a	294.68	5.99	13.005	18.24	20.725
296b	294.68	5.99	16.575	24.385	44.925
299a	297.5	6.11	14.91	19.965	49.765
299b	297.5	6.11	33.91	49.4	75.18
308a	306.5	6.51	28.9667	29.9158	29.9158
308b	306.5	6.51	17.865	19.5047	19.5047
323a	321.5	7.35	31.3692	38.3396	52.4118
323b	321.5	7.35	13.745	15.9797	19.4659
340a	339.14	9.43	76.47	85.205	101.565
340b	339.14	9.43	11.415	18.775	32.225
349a	347.6	10.47	19.68	28.2	39.54
349b	347.6	10.47	20.055	25.44	29.655
366a	364.6	13.01	29.5559	33.318	36.0252
366b	364.6	13.01	26.7307	35.6922	68.976
376a	374.7	15.51	363.405	370.348	370.348
376b	374.7	15.51	537.116	541.404	544.625
392a	391.12	31.44	93.73	115.24	128.6
392b	391.12	31.44	99.64	113.565	169.09

Table 3.S1. Dust particle concentration of Taylor Dome ice core with respect to dust particle diameter (1-5, 1-10, 1-20 μm) and age.

Sample ID	Top Depth (m)	Ice Age (ka)	La 139 (ppt)	Ce 140 (ppt)	Pr 141 (ppt)	Nd 144 (ppt)	Eu 151 (ppt)	Sm 152 (ppt)	Gd 158 (ppt)	Tb 159 (ppt)	Dy 164 (ppt)	Ho 165 (ppt)	Er 166 (ppt)	Tm 169 (ppt)	Yb 174 (ppt)	Lu 175 (ppt)
Traditional Acid Leach																
113a	113.12	1.12	0.704	3.659	0.487	1.658	0.140	0.483	0.310	0.042	0.190	0.039	0.101	0.016	0.094	0.019
113b	113.12	1.12	0.964	4.618	0.613	2.022	0.125	0.533	0.294	0.036	0.181	0.033	0.088	0.015	0.067	0.014
136b	136.12	1.52	4.038	1.751	0.244	0.928	0.129	0.377	0.194	0.027	0.132	0.026	0.080	0.011	0.061	0.015
176a	176.1	2.24	0.280	1.535	0.215	0.748	0.124	0.357	0.185	0.022	0.102	0.022	0.056	0.010	0.056	0.011
176b	176.1	2.24	0.342	1.841	0.250	0.875	0.143	0.382	0.188	0.021	0.132	0.022	0.059	0.011	0.067	0.015
208a	208.13	3.15	0.620	2.639	0.251	0.909	0.138	0.381	0.179	0.024	0.108	0.021	0.057	0.010	0.064	0.011
208b	208.13	3.15	0.314	1.650	0.230	0.828	0.141	0.394	0.166	0.023	0.093	0.020	0.053	0.009	0.052	0.011
266a	264.8	4.76	0.522	2.971	0.607	1.316	0.157	0.496	0.272	0.033	0.154	0.031	0.081	0.013	0.069	0.012
266b	264.8	4.76	0.492	2.763	0.397	1.341	0.132	0.552	0.248	0.032	0.176	0.032	0.093	0.014	0.082	0.016
281a	279.48	5.33	0.431	2.373	0.284	1.035	0.132	0.429	0.198	0.026	0.125	0.026	0.064	0.010	0.062	0.014
281b	279.48	5.33	0.644	3.254	0.452	1.555	0.159	0.545	0.326	0.042	0.188	0.037	0.094	0.016	0.085	0.014
296a	294.68	5.99	1.329	6.507	0.943	3.057	0.224	0.853	0.511	0.063	0.274	0.051	0.138	0.022	0.121	0.022
296b	294.68	5.99	0.371	2.020	0.278	0.952	0.153	0.426	0.201	0.027	0.131	0.029	0.062	0.011	0.063	0.011
299a	297.5	6.11	3.339	16.535	2.212	7.715	0.307	1.556	0.950	0.099	0.419	0.070	0.178	0.021	0.130	0.024
299b	297.5	6.11	0.706	3.682	0.520	1.919	0.187	0.652	0.344	0.046	0.208	0.039	0.109	0.015	0.107	0.029
308a	306.5	6.51	1.344	2.673	0.329	1.190	0.128	0.429	0.228	0.032	0.158	0.030	0.069	0.010	0.072	0.010
308b	306.5	6.51	1.262	2.364	0.281	0.934	0.132	0.388	0.183	0.025	0.123	0.024	0.061	0.008	0.048	0.016

323W	321.5	7.35	6.690	14.952	1.558	5.735	1.905	0.546	1.041	0.145	0.762	0.147	0.400	0.061	0.441	0.093
340F	339.14	9.43	17.734	28.264	3.584	11.997	2.923	0.621	1.659	0.215	1.134	0.225	0.643	0.097	0.943	0.189
340W	339.14	9.43	4.996	11.147	1.071	3.962	1.563	0.463	0.763	0.100	0.509	0.100	0.255	0.038	0.333	0.073
349F	347.6	10.47	2.390	3.780	0.493	1.861	1.284	0.482	0.264	0.035	0.140	0.032	0.090	0.020	0.260	0.077
349W	347.6	10.47	15.179	22.658	3.310	11.612	2.824	0.693	1.462	0.171	0.801	0.149	0.384	0.061	0.500	0.130
366F	364.6	13.01	4.514	10.034	1.005	3.821	1.489	0.514	0.669	0.090	0.481	0.104	0.288	0.043	0.379	0.064
366W	364.6	13.01	16.655	29.803	3.644	13.203	3.012	0.797	2.000	0.267	1.397	0.272	0.731	0.100	0.900	0.232
376F	374.7	15.51	94.359	233.106	23.846	93.280	20.988	4.917	19.192	2.840	16.693	3.419	9.559	1.375	9.018	1.290
392F	391.12	31.44	236.788	265.282	53.449	185.365	28.258	4.900	18.062	1.946	8.811	1.608	4.262	0.554	3.735	0.668
392W	391.12	31.44	82.595	104.096	17.833	62.489	10.863	1.986	8.251	1.034	5.149	0.958	2.495	0.343	2.436	0.504
Blank_1_F	N/A	N/A	0.001	0.072	0.003	0.090	0.280	0.689	0.050	0.005	0.031	0.388	0.002	0.004	0.012	0.006
Blank_2_W	N/A	N/A	0.002	0.055	0.004	0.054	0.276	0.638	0.045	0.006	0.006	0.002	0.004	0.005	0.012	0.007
Median samples	N/A	N/A	7.324	14.952	1.749	5.735	1.905	0.627	1.034	0.129	0.645	0.123	0.335	0.051	0.441	0.130
Median blanks	N/A	N/A	0.001	0.063	0.003	0.072	0.278	0.664	0.047	0.006	0.018	0.195	0.003	0.004	0.012	0.007

Table 3.S2. Rare earth element concentrations of traditional acid leach and full acid digestion Taylor Dome ice core samples.

Sample	Na 23 (ppt)	Sr 86 (ppt)
Traditional Acid Leach		
Blank1	6848.34	66.90
Blank2	4166.64	29.15
Blank3	2527.52	4.30
113a	68724.03	18.03
113b	23161.62	6.32
136a	14511.25	2.72
136b	25970.10	10.14
176a	11852.46	2.05
176b	10439.30	5.00
208a	17895.70	3.99
208b	12261.31	1.39
266a	14425.18	5.10
266b	11853.21	1.04
281a	13110.56	1.54
281b	8841.76	3.79
296a	9647.65	14.32
296b	10355.62	16.13
299a	14867.25	28.27
299b	7779.56	20.94
308a	7870.41	-
308b	13761.29	-
323a	15020.69	-
323b	10012.25	-
340a	16940.68	17.00
340b	16564.75	15.35
349a	11191.62	14.51
349b	13129.70	18.45
366a	37539.67	-
366b	20507.49	-
376a	76688.54	-
376b	93934.47	-
392a	36452.61	106.41
392b	39399.71	90.11
Full Acid Digestion		
113F	4681.79	14.67
113W	79241.37	65.77
136F	4240.88	38.21
136W	152160.05	74.39
176F	4725.93	28.39

176W	124336.62	45.65
208F	20692.70	239.96
208W	52360.40	77.19
266F	2945.21	12.95
266W	36709.42	60.41
281F	8321.05	70.12
281W	35345.40	59.92
296F	151835.19	778.24
296W	16288.02	59.63
299F	10460.67	51.81
299W	138801.51	166.74
340F	16122.08	66.79
340W	108382.49	200.89
349F	1251.59	7.62
349W	107019.99	82.95
392F	29135.74	302.96
392W	634566.06	2158.69
308F	5233.59	58.65
308W	145193.91	93.14
323F	6970.32	11.70
323W	116732.31	86.02
366F	38545.49	231.22
366W	352218.01	324.98
376F	44365.61	527.19
376W	511112.16	1165.45

Table 3.S3. Sodium and strontium trace element concentrations of Taylor Dome ice. Both traditional acid leached and full acid digested samples are shown.

Sample code	Collection site	Sample type	Geologic notes	Elevation (m a.s.l.)	Geographic coordinates		87Sr/86Sr	SE	εNd (0)	SE
MW1	Frontier Mountains	Regolith	Pink granite	2200	-72.605239	161.057617	-	-	-4.88	6.27E-06
FM1	Frontier Mountains	Regolith	Granite	2700	-72.988517	160.348164	0.7259550	3.91E-06	-6.74	7.24E-06
MR1	Mesa Range, Mt. Masley	Topsoil on regolith	Dolerite	2520	-72.951900	162.932197	0.7147070	3.01E-06	-4.57	1.17E-05
MR2	Mesa Range, Mt. Masley	Regolith	Dolerite	2533	-72.951689	162.933628	0.7116381	3.29E-06	-	-
IH1	Illusion Hills	Regolith	Dolerite	2760	-73.491756	162.311408	0.7114547	3.30E-06	-4.07	7.70E-06
VH1	Vantage Hills	Regolith, in fracture	Metamorphosed Beacon sandstone	2535	-73.525194	162.439331	0.7338709	4.71E-06	-2.56	3.17E-05
VH2	Vantage Hills	Regolith w/ eolian sand, in fracture	Beacon sandstone	2495	-73.523806	162.442750	0.7292057	8.57E-06	-0.49	1.02E-05
VH3	Vantage Hills	Glacial drift	Drift matrix	2535	-73.524281	162.445242	0.7117190	3.17E-05	-6.62	3.17E-05
VH4	Vantage Hills	Regolith	Beacon sandstone	2495	-73.523806	162.442750	0.7162780	8.32E-06	-2.89	1.78E-05
SM1	Intermediate Hills	Regolith	Dolerite	-	-	-	0.7111960	2.91E-06	-0.90	8.28E-06
LH1	Lichen Hills	Regolith	Pink granite regolith w/ erratic dolerite	-	-	-	0.7114596	3.75E-06	-1.90	7.75E-06
LVD3	Dry Valleys, dunes (Augustinus)	Dune	Beacon sandstone	-	-	-	-	-	-7.17	2.50E-05
DV1	Dry Valleys	Glacial drift	Older drift	1350	-77.394806	161.509861	0.7115440	3.81E-06	-7.29	1.04E-05
DV2	Dry Valleys	Lacustrine sand	Lacustrine sand from Ross Sea I on top of older glacial drift	283	-77.440361	162.661389	0.7141467	3.07E-06	-7.08	1.49E-05
DV3	Dry Valleys	Regolith, thin top soil	Dolerite, scattered Beacon erratics in the vicinity	1000	-78.082389	162.596861	0.7116150	4.33E-06	-3.70	2.36E-05

LVD5	Dry Valleys, dunes (Augustinus)	Dune	Beacon sandstone	-	-	-	0.7121380	3.85E-06	-7.63	1.06E-05
TENT	Tent Island (Erebus Bay)	Regolith	Porphiric phonolite (McMurdo Volcanics)	65	-77.683640	166.395590	0.7030415	3.22E-06	-	-
KNOB	Knob Point	Regolith	Olivine basalt w/ xenolithic inclusions (McMurdo Volcanics)	46	-77.802630	166.676580	0.7030917	3.07E-06	-0.17	2.94E-05
BRA	Bratina Island	Glacial drift	Ross Sea Drift (LGM)	78	-78.006720	165.555930	0.7076074	7.27E-06	3.00	1.55E-05
DA-IS	Dailey Island	Glacial drift	Ross Sea Drift (LGM)	66	-77.877640	164.920710	0.7040450	3.79E-06	3.21	2.32E-05
WB	Walcott Bay	Glacial drift	Ross Sea Drift (LGM)	23	-78.157240	164.029900	0.7081980	4.99E-06	1.24	3.44E-05
CCR	Cape Crozier (Ross Is.)	Glacial drift	Ross Sea Drift (LGM)	226	-77.499350	169.315010	0.7047997	7.23E-06	3.81	1.73E-05
CCR-BP	Cape Crozier, Bomb Peak (Ross Is.)	Glacial drift	Ross Sea Drift (LGM)	672	-77.515990	169.176450	0.7042658	3.53E-06	4.01	4.35E-05
MIS1	McMurdo Ice Shelf	Glacial drift	Ross Sea Drift on the ice shelf (LGM)	-8	-78.006920	165.571750	0.7041357	2.77E-06	1.50	2.83E-05
MIS2	McMurdo Ice Shelf	Glacial drift	Ross Sea Drift on the ice shelf (LGM)	-5	-78.007360	165.696750	0.7043194	3.42E-06	1.29	1.78E-05
BIRD 23.01	Cape Bird	Glacial drift	Ross Sea Drift (LGM) - Cape Bird drift	45	-77.217500	166.439680	0.7061415	7.25E-06	2.42	5.34E-05
BIRD 15.01	Cape Bird	Glacial drift on regolith	Ross Sea Drift on Olivine basalt (McMurdo Volcanics)	67	-77.268750	166.376650	0.7046932	4.43E-05	5.21	1.35E-05
BIRD 20.03	Cape Bird	Glacial drift	Holocene ice-cored moraine	320	-77.252250	166.431690	0.7068268	1.46E-05	-	-
BIRD 23.02	Cape Bird	Glacial drift	Holocene ice-cored moraine	73	-77.217490	166.445400	0.7058292	1.92E-05	2.33	6.85E-05
BIRD 19.08	Cape Bird	Glacial drift	Ross Sea Drift (LGM) - Cape Bird drift	81	-77.257390	166.383660	0.7085116	1.63E-05	4.24	3.44E-06
ROYDS 27.06	Cape Royds	Regolith	Porphiric phonolite and volcanic scoria w/ glass (McMurdo	34	-77.555100	166.165950	0.7034211	3.81E-06	-	-

			Volcanics)							
ROYDS 05.22	Cape Royds	Ash	-	37	-77.551490	166.162980	0.7039911	3.59E-06	4.77	2.71E-05
ROYDS 05.23	Cape Royds	Glacial drift on regolith	Ross Sea Drift on porphiric phonolite (McMurdo Volcanics)	37	-77.551490	166.162980	0.7031008	2.63E-06	5.21	2.88E-05
TAYLOR-1	Taylor Valley - Marr Glacier	Glacial drift	Alpine moraine, Alpine III?	754	-77.699900	162.718800	0.7124026	1.70E-05	0.51	4.88E-05
TAYLOR-2	Taylor Valley - Goldman Ponds	Glacial drift	Large moraine composite. Deglaciated in Stage 2, Stage 6+ in age	370	-77.652000	162.931630	0.7116621	2.40E-06	-7.28	1.76E-05
TAYLOR-3	Taylor Valley - Goldman Ponds	Glacial drift	Large moraine composite. Deglaciated in Stage 2, Stage 6+ in age	367	-77.650917	162.923633	0.7110585	3.55E-06	-	-
TAYLOR-4	Taylor Valley	Glacial drift	Large moraine, very old in appearance – likely Alpine III or IV.	420	-77.646633	162.891633	0.7113443	9.78E-06	-3.60	1.93E-05
TAYLOR-5	Taylor Valley	Glacial drift	Very old moraine, from Taylor Glacier or old Ross Sea drift? Basalt rich	438	-77.645683	162.881533	0.7106944	2.73E-06	2.47	1.14E-05
BULK-MW1	Frontier Mountains	Regolith	Pink granite	2200	-72.605239	161.057617	0.7309246	5.20E-06	-11.46	6.14E-06
BULK-FM1	Frontier Mountains	Regolith	Granite	2700	-72.988517	160.348164	0.7827344	6.77E-06	-12.01	8.27E-06
BULK-MR1	Mesa Range, Mt. Masley	Topsoil on regolith	Dolerite	2520	-72.951900	162.932197	0.7125194	4.31E-06	-4.56	5.82E-06
BULK-MR2	Mesa Range, Mt. Masley	Regolith	Dolerite	2533	-72.951689	162.933628	0.7101546	3.87E-06	-3.00	6.28E-06
BULK-IH1	Illusion Hills	Regolith	Dolerite	2760	-73.491756	162.311408	0.7108454	4.45E-06	-2.55	6.43E-06
BULK-VH3	Vantage Hills	Glacial drift	Drift matrix	2535	-73.524281	162.445242	0.7158163	3.84E-06	-6.21	7.02E-06
BULK-VH4	Vantage Hills	Regolith	Beacon sandstone	2495	-73.523806	162.442750	0.7177290	3.52E-06	-6.24	6.67E-06

BULK-SM1	Intermediate Hills	Regolith	Dolerite	-	-	-	0.7091309	5.08E-06	0.97	7.29E-06
BULK-LH1	Lichen Hills	Regolith	Pink granite regolith w/ erratic dolerite	-	-	-	0.7205949	4.34E-06	-0.14	9.16E-06
BULK-LVD3	Dry Valleys, dunes (Augustinus)	Dune	Beacon sandstone	-	-	-	0.7123017	3.68E-06	-7.46	7.32E-06
BULK-DV1	Dry Valleys	Glacial drift	Older drift	1350	-77.394806	161.509861	0.7123513	6.17E-06	-9.91	7.73E-06
BULK-DV2	Dry Valleys	Lacustrine sand	Lacustrine sand from Ross Sea I on top of older glacial drift	283	-77.440361	162.661389	0.7142118	3.92E-06	-8.05	7.72E-06
BULK-DV3	Dry Valleys	Regolith, thin top soil	Dolerite, scattered Beacon erratics in the vicinity	1000	-78.082389	162.596861	0.7129100	5.06E-06	-5.59	5.72E-06
BULK-LVD5	Dry Valleys, dunes (Augustinus)	Dune	Beacon sandstone	-	-	-	0.7130109	4.23E-06	-7.33	5.37E-06
BULK-TENT	Tent Island (Erebus Bay)	Regolith	Porphiric phonolite (McMurdo Volcanics)	65	-77.683640	166.395590	0.7030415	3.22E-06	5.24	9.85E-06
BULK-KNOB	Knob Point	Regolith	Olivine basalt w/ xenolithic inclusions (McMurdo Volcanics)	46	-77.802630	166.676580	0.7030917	3.07E-06	6.36	1.79E-05
BULK-BRA	Bratina Island	Glacial drift	Ross Sea Drift (LGM)	78	-78.006720	165.555930	0.7045813	3.12E-06	4.28	5.59E-06
BULK-DA-IS	Dailey Island	Glacial drift	Ross Sea Drift (LGM)	66	-77.877640	164.920710	0.7040450	3.79E-06	4.42	5.56E-06
BULK-WB	Walcott Bay	Glacial drift	Ross Sea Drift (LGM)	23	-78.157240	164.029900	0.7048276	3.27E-06	13.02	1.14E-04
BULK-GP	Gneiss Point	Glacial drift	Ross Sea Drift (LGM)	28	-77.396340	163.640700	0.7068313	4.05E-06	0.35	6.62E-06
BULK-CCR	Cape Crozier (Ross Is.)	Glacial drift	Ross Sea Drift (LGM)	226	-77.499350	169.315010	-	-	5.10	3.24E-06
BULK-CCR-BP	Cape Crozier, Bomb Peak (Ross Is.)	Glacial drift	Ross Sea Drift (LGM)	672	-77.515990	169.176450	-	-	2.31	1.59E-05
BULK-	McMurdo	Glacial	Ross Sea Drift on the	-8	-	165.571750	0.7043194	3.42E-	4.45	4.44E-

MIS1	Ice Shelf	drift	ice shelf (LGM)		78.006920			06		06
BULK-MIS2	McMurdo Ice Shelf	Glacial drift	Ross Sea Drift on the ice shelf (LGM)	-5	-78.007360	165.696750	0.7041449	2.75E-06	3.61	2.43E-06
BULK-BIRD 20.02	Cape Bird	Regolith	Porphiric phonolite and volcanic scoria w/ glass (McMurdo Volcanics)	73	-77.254870	166.406090	0.7031705	3.40E-06	5.10	1.89E-06
BULK-BIRD 23.01	Cape Bird	Glacial drift	Ross Sea Drift (LGM) - Cape Bird drift	45	-77.217500	166.439680	0.7034711	2.61E-06	4.49	2.35E-06
BULK-BIRD 15.01	Cape Bird	Glacial drift on regolith	Ross Sea Drift on Olivine basalt (McMurdo Volcanics)	67	-77.268750	166.376650	0.7042621	3.81E-06	-	-
BULK-BIRD 20.03	Cape Bird	Glacial drift	Holocene ice-cored moraine	320	-77.252250	166.431690	0.7037750	3.04E-06	3.57	1.42E-05
BULK-BIRD 23.02	Cape Bird	Glacial drift	Holocene ice-cored moraine	73	-77.217490	166.445400	0.7034866	2.97E-06	4.57	1.22E-06
BULK-BIRD 19.08	Cape Bird	Glacial drift	Ross Sea Drift (LGM) - Cape Bird drift	81	-77.257390	166.383660	0.7040031	3.44E-06	4.24	1.72E-06
BULK-ROYDS 27.06	Cape Royds	Regolith	Porphiric phonolite and volcanic scoria w/ glass (McMurdo Volcanics)	34	-77.555100	166.165950	0.7040359	3.65E-06	5.12	2.54E-06
BULK-ROYDS 05.22	Cape Royds	Ash	-	37	-77.551490	166.162980	0.7034211	3.81E-06	5.10	2.39E-06
BULK-ROYDS 05.23	Cape Royds	Glacial drift on regolith	Ross Sea Drift on porphiric phonolite (McMurdo Volcanics)	37	-77.551490	166.162980	0.7031008	2.63E-06	5.17	4.57E-06
BULK-TAYLOR-1	Taylor Valley - Marr Glacier	Glacial drift	Alpine moraine, Alpine III?	754	-77.699900	162.718800	0.7110585	3.55E-06	-2.36	2.36E-05
BULK-TAYLOR-2	Taylor Valley - Goldman Ponds	Glacial drift	Large moraine composite. Deglaciated in Stage 2, Stage 6+ in age	370	-77.652000	162.931630	0.7116621	2.40E-06	-5.73	3.41E-06
BULK-	Taylor	Glacial	Large moraine	367	-	162.923633	0.7098844	2.59E-	-5.07	8.36E-

TAYLOR-3	Valley - Goldman Ponds	drift	composite. Deglaciated in Stage 2, Stage 6+ in age		77.650917			06		06
BULK-TAYLOR-4	Taylor Valley	Glacial drift	Large moraine, very old in appearance – likely Alpine III or IV.	420	-77.646633	162.891633	-	-	-11.89	5.31E-06
BULK-TAYLOR-5	Taylor Valley	Glacial drift	Very old moraine, from Taylor Glacier or old Ross Sea drift? Basalt rich	438	-77.645683	162.881533	0.7106944	2.73E-06	-8.64	4.97E-06

Table S4. Detailed sample information of Ross Sea Sector potential source area dust (Blakowski et al., In Press).

7.2.2 Figures

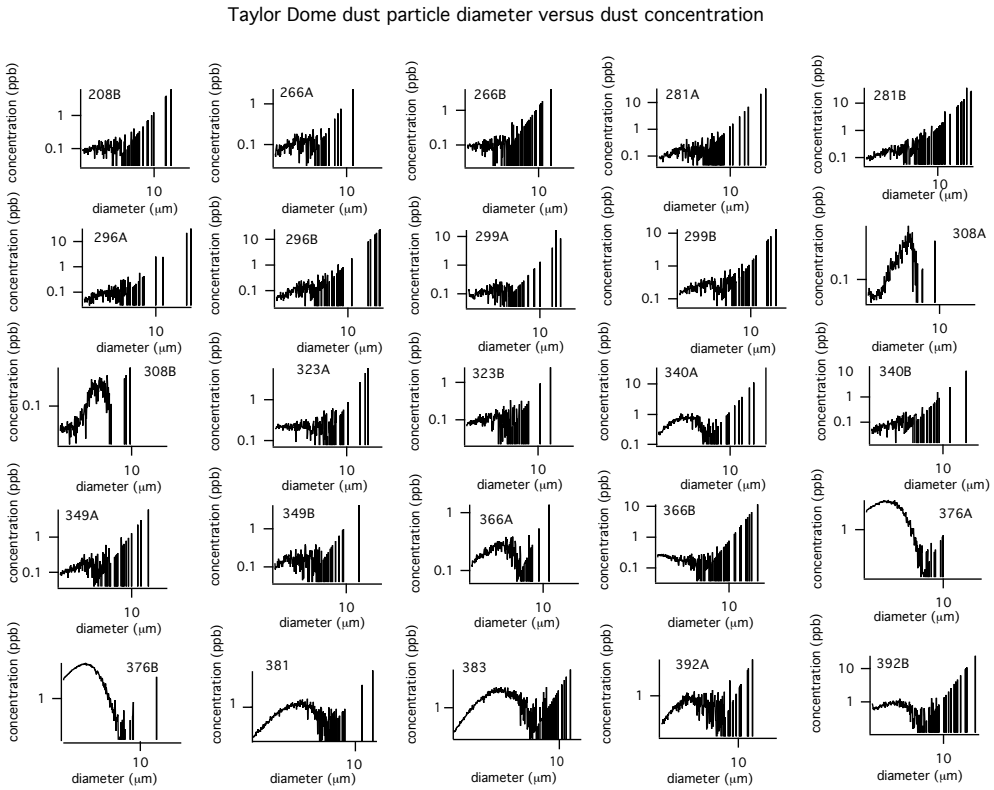

Figure 3.S1. Particle size distributions of samples measured in this study. For sample codes see Table 3.1.

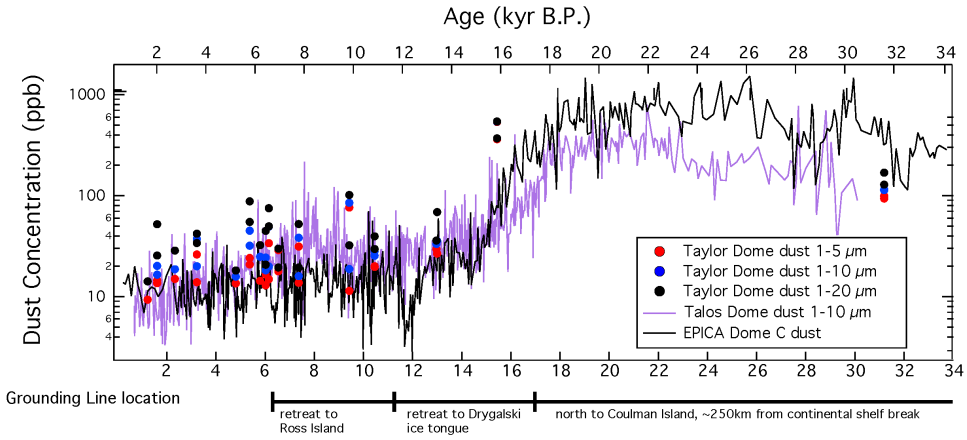

Figure 3.S2. Taylor Dome dust concentration record for three different size fractions (red circles= 1-5 red circles=1-5 μ m, blue circles=1-10 μ m, and black circles=1-20 μ m, this work) with EDC (black line; (Delmonte et al., 2004a)) and TD dust (purple line; (Albani et al., 2012)) concentration records. Also shown is the grounding line location of the Ross Ice Shelf.

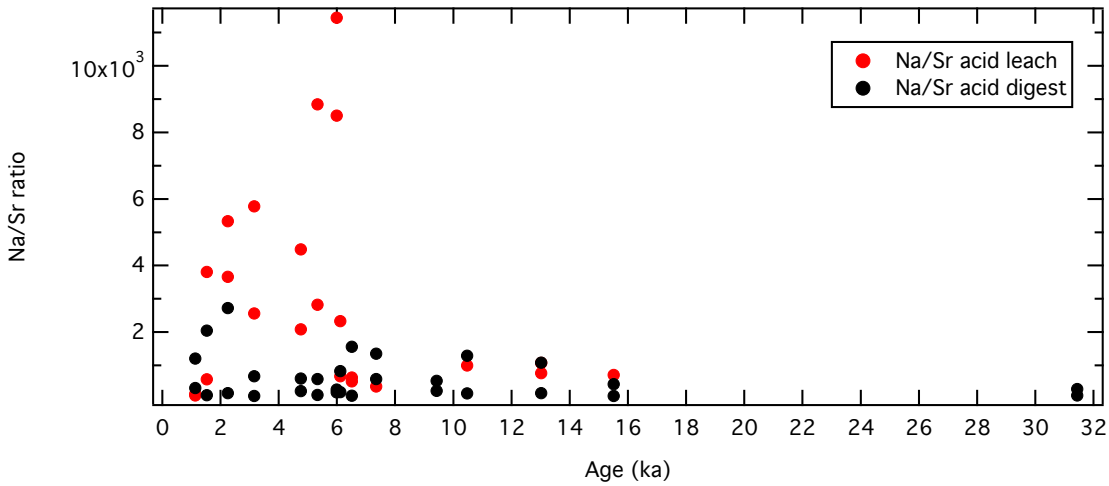

Figure 3.S3. Sodium-to-strontium ratio of samples measured in this study with respect to age.

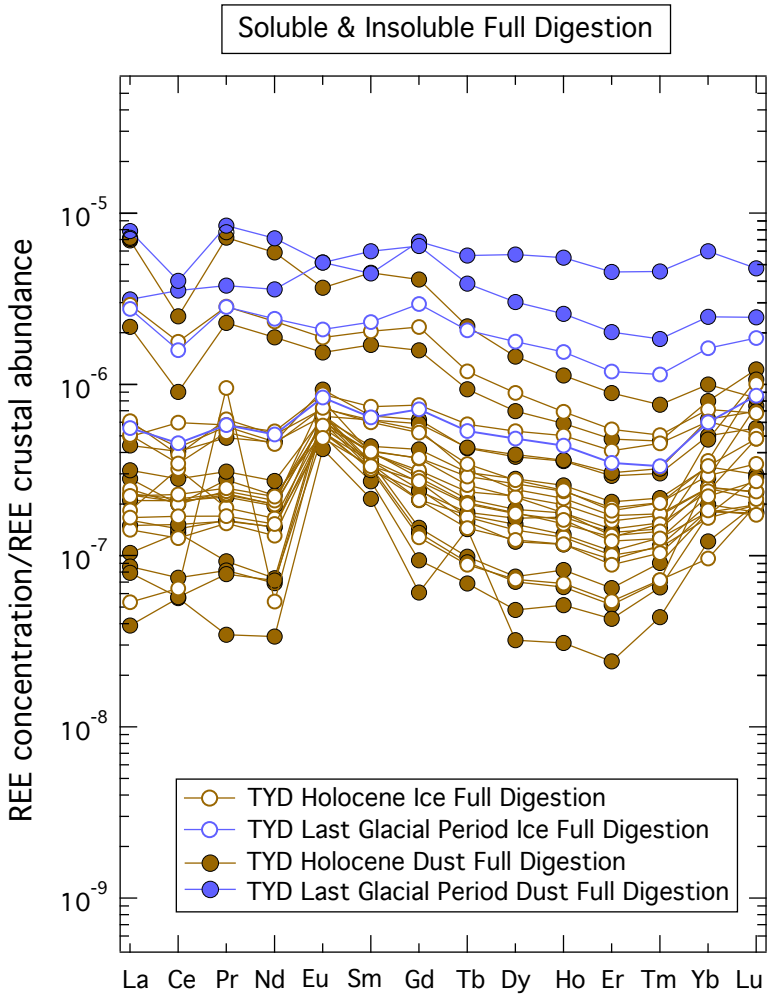

Figure 3.S4. Normalized rare earth element concentrations of TYD ice soluble and insoluble portion (full digestion) to the mean crustal abundance (Wedepohl, 1995) separated by time period.

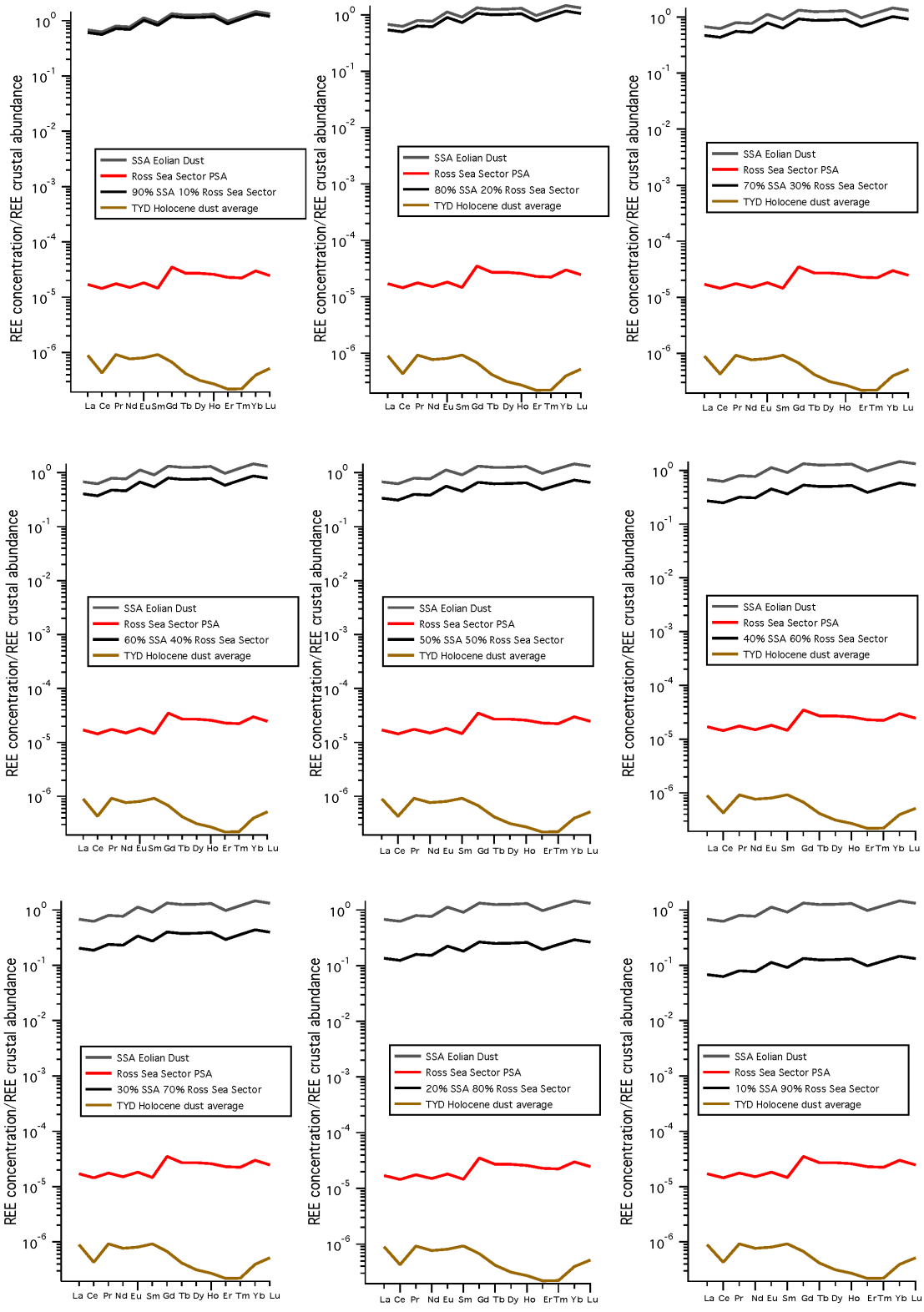

Figure 3.S5. Mixing model results of rare earth element concentrations of Taylor Dome sample with dust input from Ross Sea sector and Southern South America. Normalized modeled rare earth element concentrations of combined dust input to TYD from Ross Sea Sector (Blakowski et

al., In Press) and Southern South America (Gaiero, 2004) (black line) along with the average concentrations of Southern South American dust (gray line), Ross Sea Sector dust (red line), and the average TYD Holocene dust (brown line).

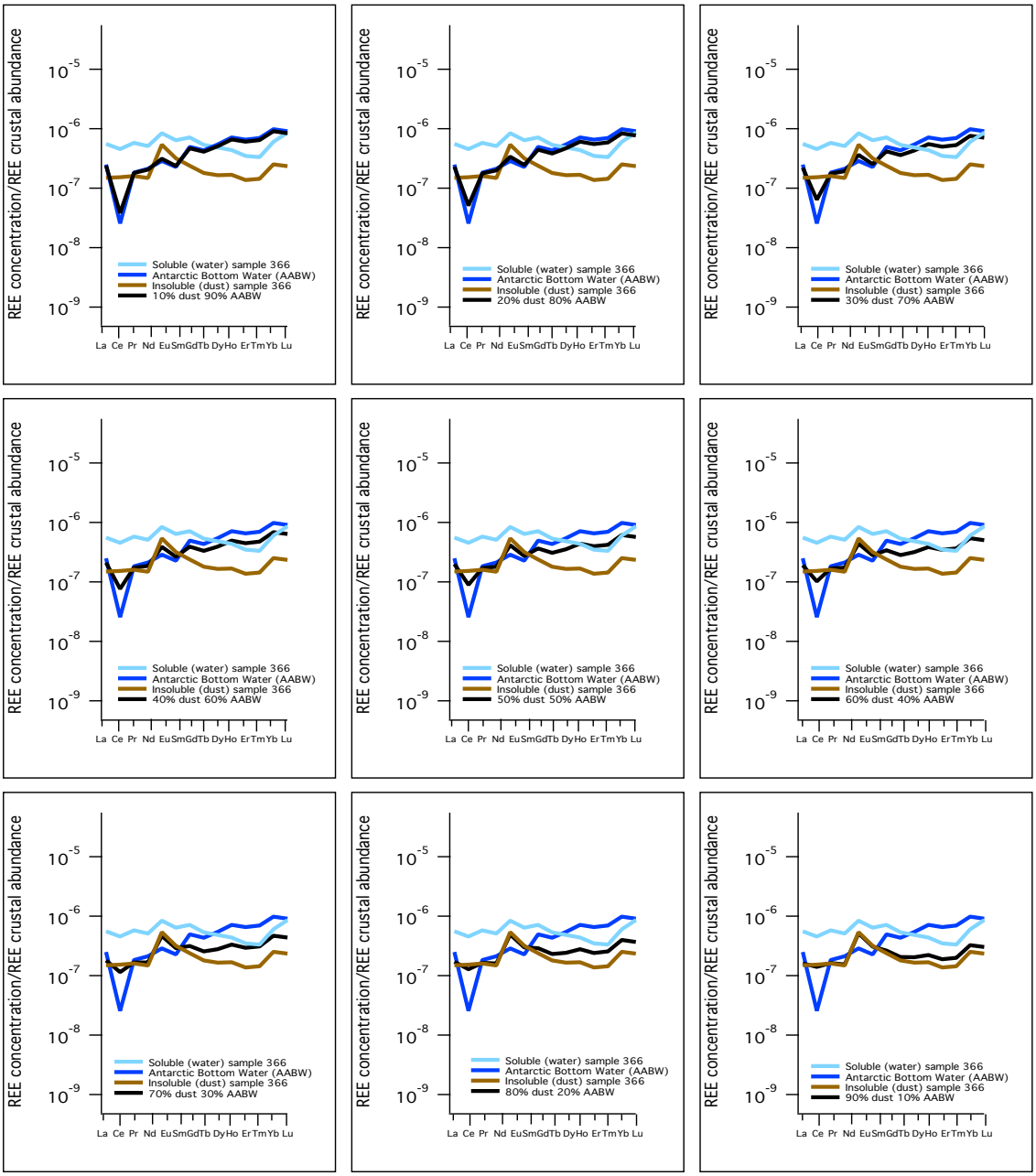

Figure 3.S6. Mixing model results of rare earth element concentrations of Taylor Dome sample with seawater and dust input. Normalized modeled rare earth element concentrations (black line) of a combined input from Antarctic Bottom Water (dark blue line) (Kawabe et al., 1998) and leaching from insoluble TYD sample 366F (brown line), also shown is the measured soluble sample 366W (light blue line).

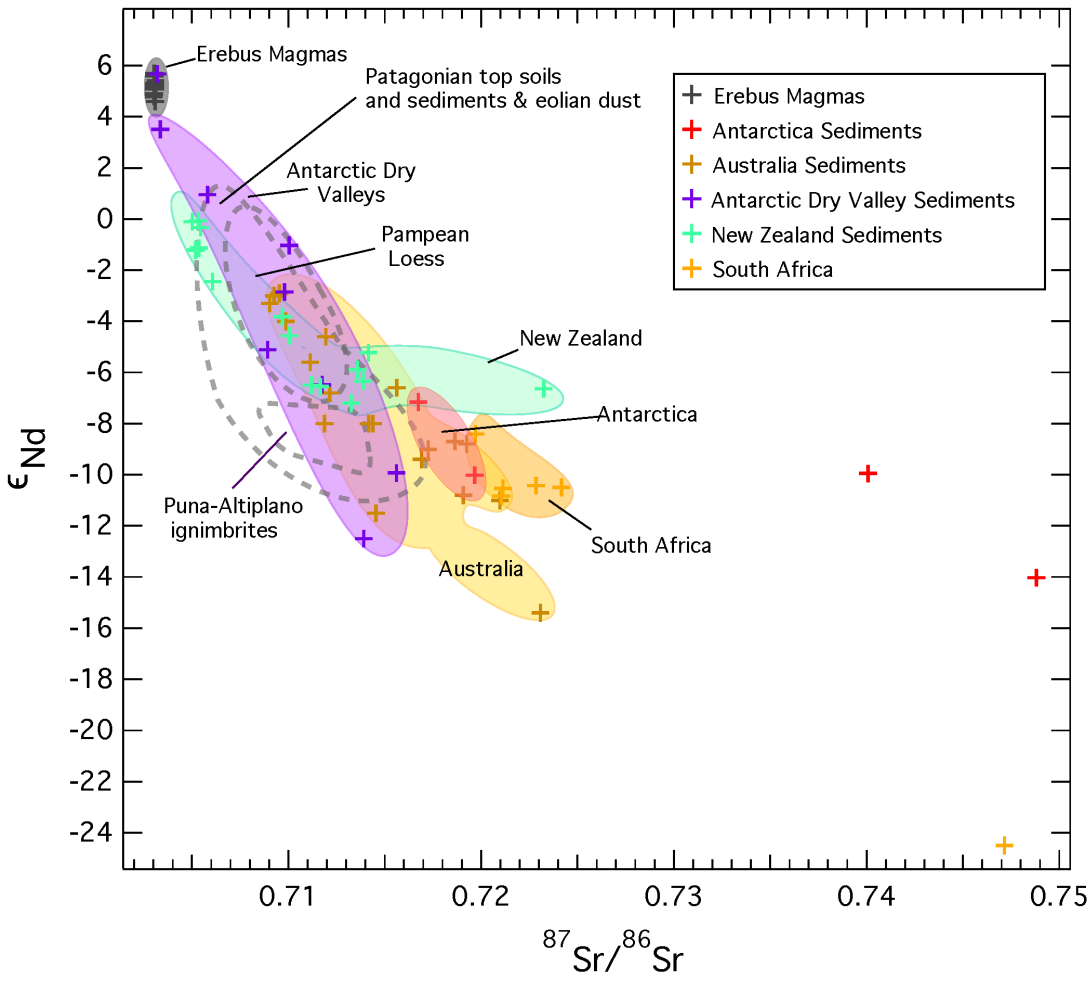

Figure 3.S7. Radiogenic isotopic compositions of potential source areas in the Southern Hemisphere plotted in various colors (colored crosses are individual data points) (Blakowski et al., In Press; Delmonte et al., 2010; Delmonte et al., 2004a; Gaiero, 2007; Grousset et al., 1992; Revel-Rolland et al., 2006; Sims et al., 2008).

7.3. References

Albani, S., Delmonte, B., Maggi, V., Baroni, C., Petit, J.R., Stenni, B., Mazzola, C., Frezzotti, M., 2012. Interpreting last glacial to Holocene dust changes at Talos Dome (East Antarctica): implications for atmospheric variations from regional to hemispheric scales. Climate of the Past 8, 741-750.
Blakowski, M.A., Aciego, S.M., Delmonte, B., Baroni, C., Salvatore, M.C., Sims, K.W.W., In Press. Sr-Nd-Hf isotope characterization of dust source areas in Victoria Land and the McMurdo Sound sector of Antarctica. Quaternary Science Reviews.
Delmonte, B., Baroni, C., Andersson, P.S., Schoberg, H., Hansson, M., Aciego, S., Petit, J.R., Albani, S., Mazzola, C., Maggi, V., Frezzotti, M., 2010. Aeolian dust in the Talos Dome ice core (East Antarctica, Pacific/Ross Sea sector): Victoria Land versus remote sources over the last two climate cycles. Journal of Quaternary Science 25, 1327-1337.
Delmonte, B., Basile-Doelsch, I., Petit, J., Maggi, V., Revel-Rolland, M., Michard, A., Jagoutz, E., Grousset, F., 2004a. Comparing the EPICA and Vostok dust records during the last 220,000 years: stratigraphical correlation and provenance in glacial periods. Earth-Science Reviews 66, 63-87.
Gaiero, D.M., 2004. The signature of river-and wind-borne materials exported from Patagonia to the southern latitudes: A view from REEs and implications for paleoclimatic interpretations. Earth and Planetary Science Letters 219, 357-376.
Gaiero, D.M., 2007. Dust provenance in Antarctic ice during glacial periods: from where in southern South America? Geophysical Research Letters 34.
Grousset, F.E., Biscaye, P.E., Revel, M., Petit, J.-R., Pye, K., Joussaume, S., Jouzel, J., 1992. Antarctic (Dome C) ice-core dust at 18 k.y. B.P.: Isotopic constraints on origins. Earth and Planetary Science Letters 111, 175-182.
Kawabe, I., Toriumi, T., Ohta, A., Miura, N., 1998. Monoisotopic REE abundances in seawater and the origin of seawater tetrad effect. Geochemical Journal 32, 213-229.
Revel-Rolland, M., De Deckker, P., Delmonte, B., Hesse, P., Magee, J., Basile-Doelsch, I., Grousset, F., Bosch, D., 2006. Eastern Australia: a possible source of dust in East Antarctica interglacial ice. Earth and Planetary Science Letters 249, 1-13.
Sims, K.W.W., Blichert-Toft, J., Kyle, P.R., Pichat, S., Gauthier, P.-J., Blusztajn, J., Kelly, P., Ball, L., Layne, G., 2008. A Sr, Nd, Hf, and Pb isotope perspective on the genesis and long-term evolution of alkaline magmas from Erebus volcano, Antarctica. Journal of Volcanology and Geothermal Research 177, 606-618.
Wedepohl, K.H., 1995. The composition of the continental crust. Geochimica Et Cosmochimica Acta 59, 1217-1232.

CHAPTER IV

Dust aerosol composition changes in East Antarctica during Glacial-Interglacial transition

Official citation:
S.M. Aarons, S.M. Aciego, C.A. Arendt, M.A. Blakowski, A. Steigmeyer, P. Gabrielli, Hernandez, R.S., B. Delmonte, Baccolo, G., Pratt, K., and May, N., In Preparation. Dust aerosol composition changes in East Antarctic during Glacial-Interglacial transition. Quaternary Science Reviews.

Abstract

Dust transported in the atmosphere prior to deposition in oceans, ice sheets and the terrestrial biosphere is recognized as a source of critical nutrients and may therefore affect the global carbon cycle. Thus, temporal changes in locations of dust source areas and the transport pathways have implications for understanding the interactions between mineral dust, global climate, and biogeochemical cycles. Chemical and physical characterization of the dust record preserved in ice cores is useful for reconstruction of dust source region, dust availablity for transport, dominant wind direction and storm trajectory. Dust transported to East Antarctica during the Last Glacial Period (LGP) has been investigated using radiogenic isotopes and dust size distribution. In this study we expand the existing Sr and Nd isotopic record of dust particles within East Antarctic ice and integrate Taylor Glacier (TG), Antarctica dust concentration, size distribution, trace and rare earth element concentrations and chloride concentration to act as additional proxies for dust source provenance. The insoluble dust in TG ice ranges in $^{87}Sr/^{86}Sr$ composition from 0.708 to 0.711

during the LGP compared to 0.707 to 0.714 during the Holocene. The ε_{Nd} composition ranged from 0.1 to -3.9 and 1.9 to -8.2 during the LGP and the Holocene respectively. The isotopic compositions combined with multiple physical and chemical constraints support previous work attributing Southern South America (SSA) as the dust source to East Antarctica during the LGP and local Ross Sea Sector dust sources after the transition to the Holocene and the retreat of the Ross Ice Shelf. Measurements on modern dust transported to TG indicate Australia as a possible increasing dust contributor to East Antarctica.

4.1. Introduction

Ice cores drilled from ice sheets in Greenland and Antarctica serve as excellent archives of atmospheric composition and climate over hundreds of thousands of years (Jouzel et al., 1997; Petit et al., 1999; Spahni et al., 2005). Valuable climate parameters such as greenhouse gases (CO_2 and CH_4), stable isotope variability in precipitation, and radiogenic isotope compositions of dust in ice are utilized to reconstruct long-term records of atmospheric change. Dust records preserved in ice cores drilled from Greenland and Antarctica reveal variations in dust flux during glacial-interglacial periods and provide yet another proxy for temperature over long timescales using δD and $\delta^{18}O$ (Basile et al., 1997; Biscaye et al., 1997; Delmonte et al., 2004b; Delmonte et al., 2007; Grousset et al., 1992; Lambert et al., 2008; Petit et al., 1981; Petit et al., 1999; Revel-Rolland et al., 2006). Physical and chemical characterization of dust particles entrained in

Antarctic ice allows the tracing of dust to sediments from potential source areas (PSAs), (Delmonte et al., 2008; Delmonte et al., 2013; Delmonte et al., 2010; Delmonte et al., 2004a; Delmonte et al., 2004b; Delmonte et al., 2007; Grousset and Biscaye, 2005) which are likely sources of aerosol mineral dust transported through the atmosphere and then deposited.

It has been established that the dominant source of dust to East Antarctica during the LGP is most likely Southern South America (SSA) (Basile et al., 1997; Delmonte et al., 2004a; Grousset et al., 1992). Higher amounts of dust transported to Antarctica during glacial periods is a result of increased dust availability at the source area and windier conditions caused by the more pronounced pole-equator temperature gradient (Delmonte et al., 2004a; Hammer et al., 1985). Consequently, dust transported to Antarctica during the Holocene is not well characterized due to the extremely small concentrations in Antarctic ice (Delmonte et al., 2013; Delmonte et al., 2010). The larger observed dust particle diameters and elemental and isotopic compositions of dust in Holocene ice suggest a shift in dust source from long-range (i.e. SSA) to a more proximal area such as ice-free Antarctic terrains (Delmonte et al., 2010; Delmonte et al., 2007; Gabrielli, 2010).

One major analytical limitation for ice core science is the amount of ice available for measurements. Traditional ice cores are expensive and logistically challenging to retrieve, and the small amount recovered places limitations on the

amount and variety of analytical measurements. Due to the extremely small amount of dust present in Antarctic ice, it is necessary to collect larger ice samples for more precise and accurate radiogenic isotope measurements.

The nature of ice sheet dynamics results in old ice exposed at the ablation area, or ice sheet margin, as the ice flows outward from the accumulation area. The horizontal exposure of ice stratigraphy results in the oldest ice at the toe of the glacier and progressively younger ice towards the equilibrium line. Ice exposed in this fashion has been referred to as a 'horizontal ice core' and has been used successfully for paleoclimate studies (Aciego et al., 2007; Reeh et al., 1991) and the acquisition of previously unobtainable measurements of trace gases, isotopes of trace gases (Buizert et al., 2014; Petrenko et al., 2016) and low concentration particles such as dust (this study). In this study, we use a 'horizontal ice core' from Taylor Glacier (TG), East Antarctica to characterize the dust deposited during the LGP, the deglaciation and the Holocene to understand how the aerosol composition changed during major climate shifts.

4.2. Regional setting

Taylor Glacier ice originates from the area of accumulation, Taylor Dome, and winds through the Transantarctic Mountains before terminating on land in the McMurdo Dry Valleys. Taylor Glacier is located on the eastern portion of the East Antarctic ice sheet (Figure 4.1) and is close to the Ross Ice Shelf and the

seasonal sea ice of the Ross Sea. Katabatic-driven movements of cold air masses originating from interior Antarctica influence the weather at TG. These cold air masses approach primarily from the southwest (Morse et al., 1998) whereas warmer air masses with high amounts of precipitation approach from the south (Morse, 1997). The TG ablation area is suitable for paleoclimate reconstruction as demonstrated by previous work (Aciego et al., 2007; Kavanaugh and Cuffey, 2009).

The glacier contains a paleoclimate record extending over 100,000 years (Brook, 1993; Steig, 2000). Taylor Glacier is comprised of blue-ice, and is susceptible to sublimation, which results in approximately 2/3 of the mass loss occurring during the summer months (Bliss et al., 2011). Ice velocities range from approximately 10 m/year in the central portion of the glacier and are slower closer to the lateral ice margins as a result of basal freezing (Kavanaugh and Cuffey, 2009). The ice surface is mostly smooth and crevasse free, but is covered by suncups, bowl-shaped depressions in the ice surface caused by melting from direct solar radiation. Thermal contraction caused by variations in summer and winter temperatures results in surface cracking, which may reach several meters below the surface.

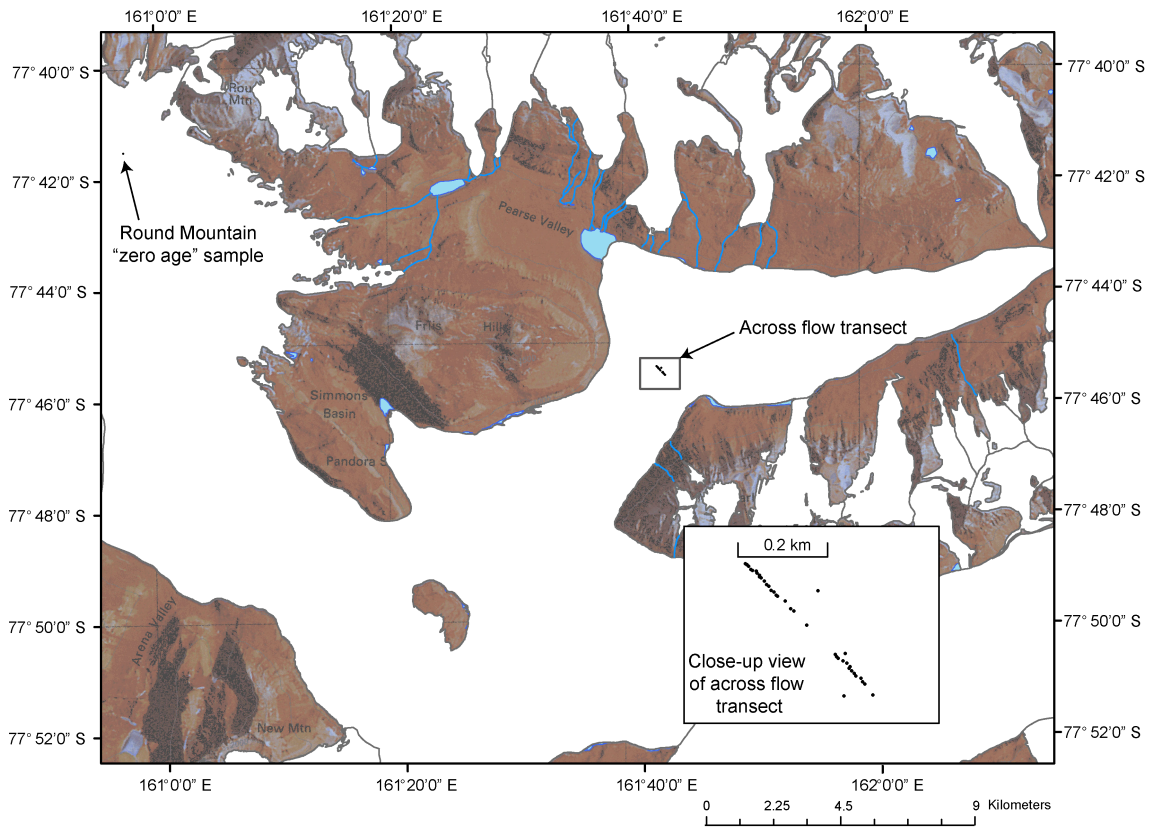

Figure 4.1. Map of Taylor Glacier and sampling transect locations (•) and the 'zero-age' sample at Round Mountain. Each symbol represents one sample. Inset map is a close up of the sampling transect.

4.2.1. Local climate effects of retreating ice shelf extent

Changes in the volume and/or extent of ice sheets and ice shelves should have an influence on local climate, including wind speed and direction, dominant storm trajectories, and even large scale atmospheric circulation. Models have demonstrated that ice sheets can cool air locally (Liakka and Nilsson, 2010), and the high albedo and height of ice sheets can create zonal anomalies in surface temperatures (Beghin et al., 2014; Cook and Held, 1988) both of which can affect the atmospheric flow response. Ice sheets have also been linked to inducing changes in the subtropical jet position, which will undoubtedly have an influence

on dominant wind directions and storm trajectories (Hall et al., 1996; Kageyama and Valdes, 2000; Laîné et al., 2008; Rivière et al., 2010).

Transport and tropospheric mixing at high latitudes are driven by synoptic eddy activity, which grow by baroclinic instability and decay by breaking and mixing of the surrounding air, termed “wave breaking” (Barnes and Hartmann, 2012; McIntyre and Palmer, 1983). Upper troposphere Rossby wave-breaking processes associated with ice sheet extent in the Northern Hemisphere have been examined in coupled ocean-atmosphere models of the Last Glacial Maximum (LGM) and the present (Rivière et al., 2010). The temperature gradient is largely influenced by the presence of large ice sheets, and since the temperature gradient is a driver of Rossby wave breaking there is evidence of an ice sheet influence on zonal winds and storm trajectory dynamics, (Rivière et al., 2010).

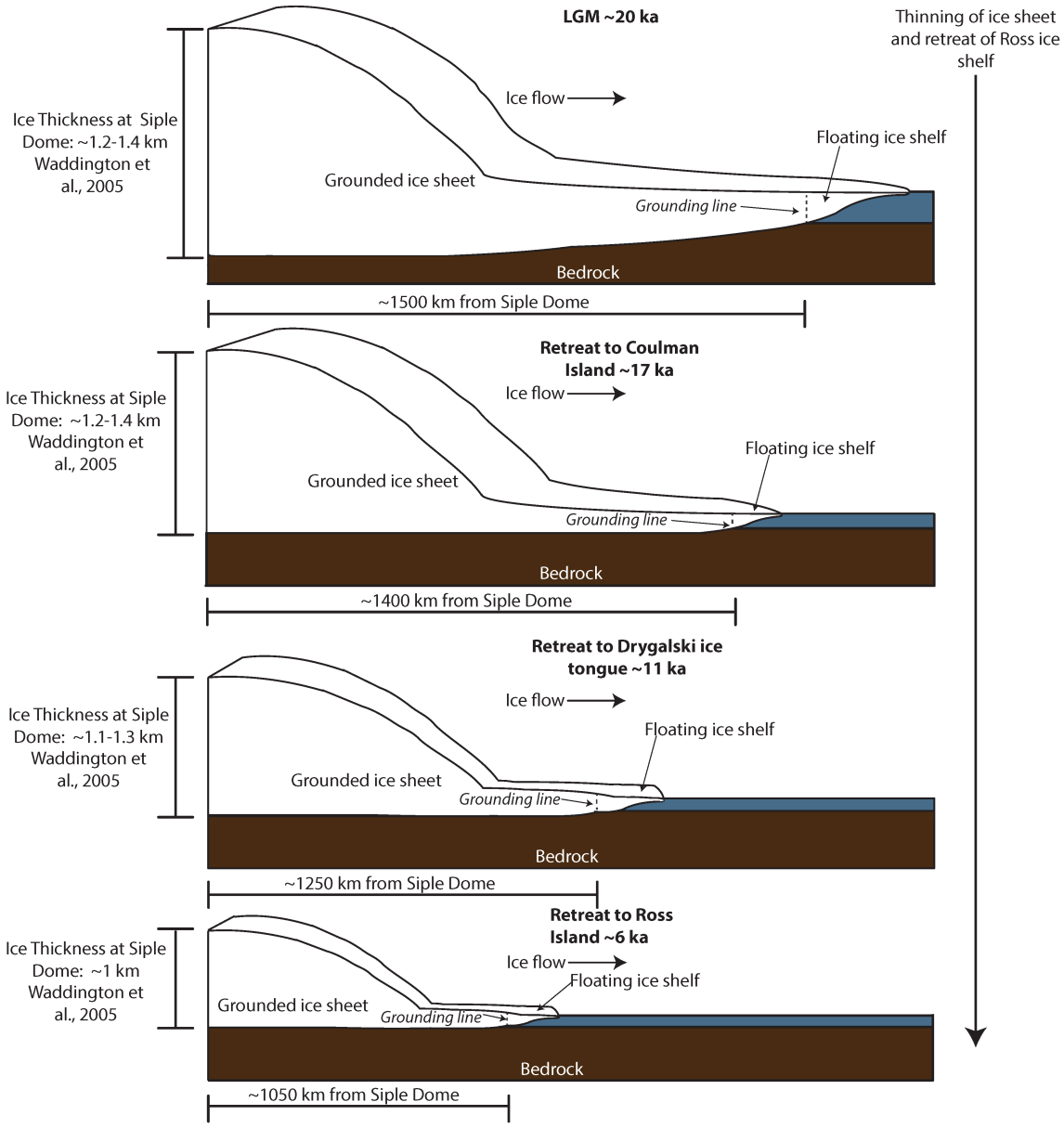

Figure 4.2. Schematic cross section of ice sheet and ice shelf extent from Siple Dome to the Ross Ice Shelf. Ice thicknesses (Waddington et al., 2005) and approximate distance from Siple Dome to Ross Ice Shelf grounding line are shown.

The movement of the Ross Ice Shelf grounding line, transition from ice sheet to ice shelf (Figure 4.2), and the establishment during the Holocene of atmospheric moisture transport from the south, which reduced snowfall on the north side of Taylor Dome and would have been one of the largest and most rapid climate and

weather pattern change in the region (Morse et al., 1998). Changes in ice sheet extent can drive atmospheric dynamics on short (i.e. seasonal and decadal) to long (i.e. millennial and glacial-interglacial) timescales, and the dust record preserved in the TG serves as a model for the effects of ice sheet retreat on local, coastal climate. We use high-precision geochemical techniques to the high-volume, high-resolution horizontal ice core at TG to distinguish regional versus global aerosol flux sources, determine if the changing climate and weather in the Ross Sea region from the LGM (21 ka) through the Preboreal Holocene is recorded by aerosol compositional changes and to provide a record of southern hemisphere dust through the Younger Dryas and Antarctic Cold Reversal. We establish baseline measurements of trace elements, anions and cations, and radiogenic isotopes of dust within the TG horizontal ice core to show the restructuring of sources and transport pathways of dust during the last deglaciation, and we integrate our results into the current understanding of climate in the Ross Sea region, Antarctica.

4.2.2 Age scale of Taylor Glacier 'horizontal ice core'

Ice cores record climate proxies in the gas phase (i.e. CH_4 and CO_2 concentration and $\delta^{18}O_{atm}$) and the ice phase (i.e. $\delta^{18}O$ of precipitation and aerosol mineral dust). Due to the open porosity of firn, gases are still exchanging with the atmosphere prior to ice formation resulting in a gas age-ice age difference that is dependent on the accumulation rate of precipitation at the site. To establish the ice age of the TG across flow transect, previous work

(Baggenstos, 2015) measured trace gases in an across-flow transect on ice from the marine isotope stage (MIS) 3, the LGM, and the deglaciation into the Holocene. Baggenstos (2015) created a high-resolution age model for the TG transect using CH_4 and CO_2 inflection points (Bauska, 2013) and $\delta^{18}O_{atm}$ as additional tie points. Due to a fold in the TG ice stratigraphy, two separate age models were created on opposite sides of the fold for the 'older' ice (-80 to -300 m) and for the 'young' ice (+30 to 260 m) (Baggenstos, 2015). The resulting age models have an overlap of ~2000 years. The relative uncertainties in the 'young' age model are small (<500 years) due to high oscillation of $\delta^{18}O_{atm}$, however the 'older' section contains higher age uncertainties due to fewer methane tie points, lower oscillation of $\delta^{18}O_{atm}$ and lower sample resolution (Baggenstos, 2015). More recent work (Petrenko et al., 2016) used both $\delta^{18}O_{atm}$ and CH_4 values for accurate estimation of sample gas age and visual matching of CH_4 data to the high-resolution WAIS Divide ice core (Members, 2015). The ^{81}Kr radiometric dating (Buizert et al., 2014) at the TG is used as an additional independent method of dating, and supports independently derived ages using CH_4 and $\delta^{18}O_{atm}$.

4.3. Materials and methods

4.3.1 Sample collection

Ice samples were collected during a field season in the austral summer, 2013 for analysis of radiogenic isotope composition, dust concentration and size distribution, and trace and rare earth element concentration. We present data

from an across-glacier sampling line (Figure 4.1), from which 119 samples (80 unique, 39 duplicate) were recovered from between 6-7 meters below the surface. The sampling distance ranged from 1 sample/5 m for 195 m (Holocene ice) and 1 sample/7 m for 133 m (LGP ice). Additionally, 2 samples were collected near Round Mountain (77°41’ S, 160°57' E) for approximate zero-age ice and 2 surface samples were taken for surface contamination analysis. All samples are unfractured and entirely in one piece. All drilling was performed with the Blue Ice Drill (BID) (Kuhl et al., 2014) provided by Ice Drilling Design and Operations (IDDO) and results in ice cores that are 1 m in length and 24 cm in diameter weighing ~40 kg. Immediately after drilling and retrieval, the ice samples were cut in half with an electric chainsaw and were boxed and stored in an ice trench on site until transfer to McMurdo Station.

4.3.2 Sample preparation and processing

A series of 38 samples from TG were selected between the time period of ~46-0 ka based on a previously established timescale (Baggenstos, 2015). Fourteen samples were selected from the LGP (defined here as ~46-15 ka) and 23 samples span the Holocene time period (defined here as ~15-0 ka) including one ‘zero-age sample’ from Round Mountain. In addition, 1 surface sample (N91 surface) was analyzed to determine the potential contribution of dust from ice-free areas surrounding TG.

Each sample is approximately 20 kg and was decontaminated and processed at the Glaciochemistry and Isotope Geochemistry Laboratory (GIGL) at the University of Michigan (UM). A longitudinal portion of each ice core sample was cut using a custom-made stainless steel handsaw in a freezer at -15° C for trace element (TE), rare earth element (REE), ion chromatography (IC) and coulter counter (CC) analysis. The remaining portion of ice was decontaminated by sawing off the outer ice core and rinsing with distilled ethanol prior to transfer into a custom-made acrylic ice core holder. After transport to a class 10,000 clean room at the UM, the samples were rinsed with deionized water and melted using infrared radiation over a 24-hour period and the meltwater was immediately filtered through an acid-cleaned 0.2 μm Teflon filter. The filtrate (hereafter defined as the 'soluble fraction') was collected and dried down inside a class 10 laminar flow hood under nitrogen flow and infrared radiation before dissolution in ultra-pure 9 M HCl acid for ion-exchange column chemistry (Aciego et al., 2009).The separated dust (hereafter defined as the 'insoluble fraction') was digested and dissolved directly off the 0.2 μm filters using ultra-pure HCl, aqua regia, and HNO_3-HF acid and subsequently dissolved in 9 M HCl acid. The samples were chemically separated using ion-exchange columns with Eichrom resins following previously established procedures (Aarons et al., 2013; Aciego et al., 2009) for Sr and Nd isotopic analysis.

4.3.3 Trace and Rare Earth Element analysis

Samples for TE and REE concentration analysis were triple rinsed using MilliQ water using acid pre-cleaned LDPE pliers and melted in pre-cleaned LDPE Nalgene bottles using procedures established by Boutron et al. (Boutron, 1990). The meltwater was immediately acidified in 2% HNO_3 (ultra-pure) for approximately 1 month prior to analysis (procedural blanks are presented in Table 4.S1 and S2). Trace element and REE concentrations were determined at The Ohio State University on a Thermo Element2 Inductively Coupled Plasma Sector Field Mass Spectrometer (ICP SFMS) coupled with a micro-flow nebulizer and a desolvation system (Apex Q). The system allows TE and REE detection down to the sub-pg g^{-1} levels (Uglietti et al., 2014). For TEs, low mass resolution was used for the detection of Li, Na, Rb, Sr, Nb, Ba, Bi, and U, medium mass resolution for Al, V, Cr, Mn, Co, and high mass resolution for As.

4.3.4 Chloride ion analysis

Samples for IC analysis were triple rinsed using MilliQ water using acid pre-cleaned LDPE pliers and kept frozen in PFTE centrifuge tubes triple rinsed in deionized water until just prior to analysis. A Dionex ICS-1100 and ICS-2100 ion chromatographs were used to analyze chloride (Cl^-) ions in the TG samples. The ICS-1100 and ICS-2100 were equipped with a 200 µL sample loop and a heated conductivity cell (DS6, Dionex). Methanesulfonic acid (20 mM) was used as eluent for the cation column and KOH gradient generated by an EGC III KOH system was used as eluent for the anion column. All samples were run in triplicate and averaged.

4.3.5 Dust particle size and concentration analysis

The dust concentration and size distribution samples were triple rinsed using MilliQ water with acid pre-cleaned LDPE pliers and stored in triple rinsed PFTE centrifuge tubes frozen until analysis following procedures described in Delmonte et al. (Delmonte et al., 2004a). Approximately 20 mL was available for Coulter® Counter microparticle concentration and size distribution measurements in the diameter range of 0.6-17.9 μm. Each sample underwent five consecutive measurements to ensure the precision of the results. Blanks were negligible and the reproducibility was good for highly concentrated samples (<2% for 50,0000 particles g^{-1}); however lower concentrated samples do experience scattering (~2% for 1000/g) (Delmonte et al., 2002).

4.3.6 Strontium and neodymium isotope analysis

Following ion-exchange chemistry, chemically separated strontium (Sr) samples were measured on the University of Michigan Thermo Scientific Triton *Plus* Thermal Ionization Mass Spectrometer (TIMS) and normalized to $^{88}Sr/^{86}Sr=8.375209$ to account for mass bias using the exponential law. Rubidium interferences were monitored by observing ^{85}Rb in the center cup, and all beam sizes were less than 10^{-13} A. The long term reproducibility of Sr isotopic standard SRM987 (100 ng) is $^{87}Sr/^{86}Sr=0.710256 \pm 8$ (2σ SD, n=322). The United States Geologic Survey (USGS) reference material BCR-2 was measured concurrently with the TG samples and averaged 0.704999 ± 24 (2σ SD, n=2), similar to

published values (0.705000) (Jweda et al., 2015). The neodymium (Nd) samples were measured on a Thermo Scientific Triton *Plus* TIMS at the University of Michigan and normalized to $^{146}Nd/^{144}Nd=0.7219$ using the exponential mass law and mass 149 was monitored for Sm interference. The long-term average for JNdi-1 is 0.512101± 24 (2σ SD, n=19). The concurrently measured BCR-2 (10 ng) averaged 0.512642 ± 21 (2σ SD, n=4), close to the established measured values (0.512637) (Jweda et al., 2015).

All Nd isotope compositions are reported here as ε_{Nd}, which is defined as: $\varepsilon_{Nd} = ([(^{143}Nd/^{144}Nd)_{sample}/(^{143}Nd/^{144}Nd)_{CHUR}]-1) \times 10^4$, where $(^{143}Nd/^{144}Nd)_{CHUR}$ is the Nd isotopic composition of the Chondritic Uniform Reservoir (CHUR) which is $^{143}Nd/^{144}Nd=0.512638$ (Jacobsen and Wasserberg, 1980).

4.4. Results

The isotopic compositions of TG dust, trace and rare earth element concentrations, Cl^- concentration, and dust particle diameter and concentration analyzed here are reported in Table 4.1, 4.S1, 4.S2, 4.S3 and 4.S4 respectively.

4.4.1 Trace and Rare Earth Element concentration

Concentrations of TEs and REEs in TG ice during the LGP and the Holocene are shown in Figures 4.3 and 4.5 respectively. Distinct variations in concentrations are observed for all elements over the ~46,000 year time period studied here. The highest concentrations for Rb (535 pg/g) are approximately 70 times higher

than the lowest observed concentration (7.9 pg/g). The variations may be related to climatic conditions, as in general, the highest observed concentrations occur during the LGP and concentrations of most elements were markedly low during warm periods, characterized by less negative $\delta^{18}O$ values (Figure 4.3).

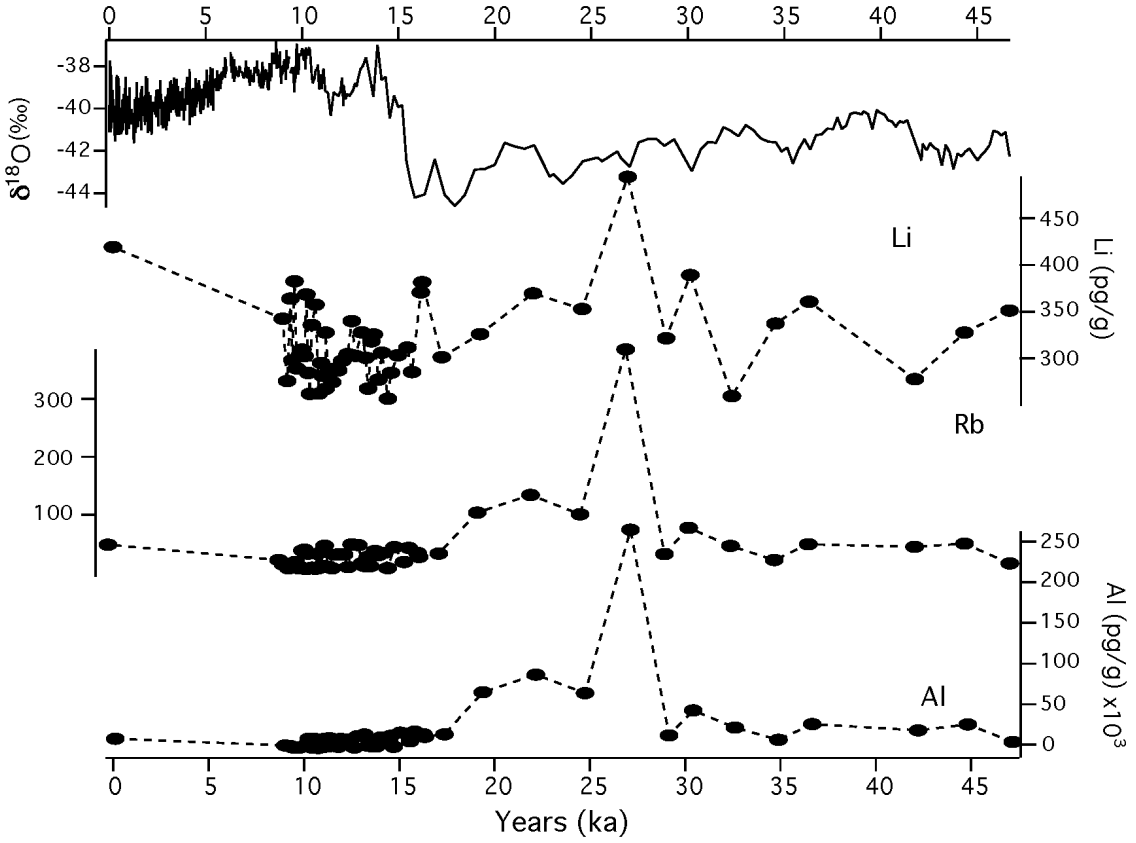

Figure 4.3. Variations in trace elements Li, Rb, and Al concentration as a function of age of the ice during time period studied. Also shown at the top of the figure is the Taylor Dome ice core oxygen isotope profile (Grootes et al., 2001).

To assess the contribution of trace elements originating from rock and soil to the TG, we calculated the crustal enrichment factors (EF_c) for each element and sample. The EF_c is defined here as the concentration ratio of a particular element relative to that of Fe (which serves as a proxy for rock and soil dust, as it is

primarily derived from that source alone) in the ice, normalized to the same concentration ratio found in the upper continental crust. Iron is used as the crustal reference for comparison to previous ice core TE concentration values (Uglietti et al., 2014). For example, the EF_c for Sr is:

$EF_c=([Sr]_{ice}/[Fe]_{ice})/ ([Sr]_{crust}/[Fe]_{crust})$

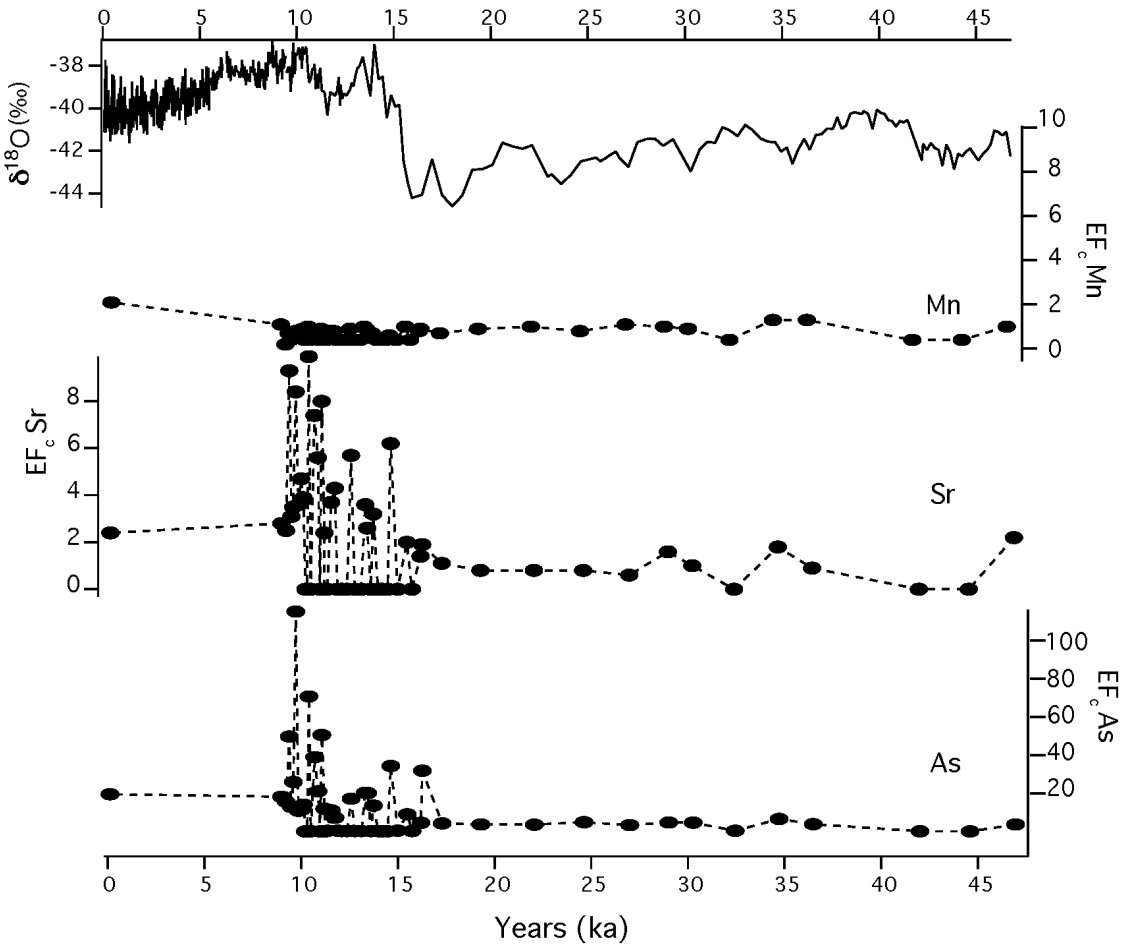

Figure 4.4. Variations in trace elements Mn, Sr, and As crustal enrichment factor as a function of age of the ice during time period studied. Also shown at the top of the figure is the Taylor Dome ice core oxygen isotope profile (Grootes et al., 2001).

We used the upper continental crust concentrations provided by Wedepohl (Wedepohl, 1995) to calculate EF_c, with values between 1 and 10 (Gabrielli et al.,

2005) indicating elements originating from a crustal (i.e. rock or soil) source. Any EF_c values significantly larger than ten indicate a contribution from other natural sources (i.e. forest fires). When analyzing the values obtained for different TEs throughout the time period studied here, the elements may be distinguished into several different groups similar to previous studies of TEs in the Vostok Antarctic ice core (Gabrielli et al., 2005). The first group is comprised of elements with EF_c values close to 1, regardless of the time period: Al, V, Mn, Rb, Nb, Ba and U (Table 4.S1 and Figure 4.3 for Mn). A second group of elements is comprised of Li, Na, Cr, Co, and Sr for which the EF_c values are low in some time periods and higher during others (Table 4.S1). As seen in Figure 4.4 for Sr, the lowest values are observed during the LGP and the higher values are observed during the Holocene, which has also been noted in another East Antarctic ice core (Gabrielli et al., 2005). The last group consists of As and Bi, which have few values close to 1 and whose lowest values are observed during colder time periods and highest are during the Holocene. The values observed during the LGP however, are still moderate compared to the second group of TEs.

The concentrations of REE are within the sub-picogram/g to picogram/g range, and among all samples a large variation is observed. Ice samples from the Holocene (~0-14.8 ka) are in general lower in concentration than those from the LGP (~15.3-46.7 ka) due to a higher dust input during glacial periods. The full range of REE concentrations is summarized in Table 4.S2 and the REE concentrations normalized to mean crustal REE abundance (Wedepohl, 1995)

are presented in Figure 4.5. Comparable REE pattern shapes may be indicative of uniform dust source areas (or a congruent mixing of dust sources) and variations from a constant pattern may be a result of a shift in dust source area. The observed REE patterns during the LGP are similar to concentrations observed in previous Antarctic ice cores (Gabrielli, 2010; Gabrielli et al., 2005; Wegner et al., 2012), and nearly all samples from the Holocene have a positive Eu anomaly (Figure 4.5) which was also observed in samples from the Taylor Dome ice core (Aarons et al., In Press), but not in ice cores from the interior East Antarctic ice sheet (Gabrielli, 2010; Gabrielli et al., 2005; Wegner et al., 2012).

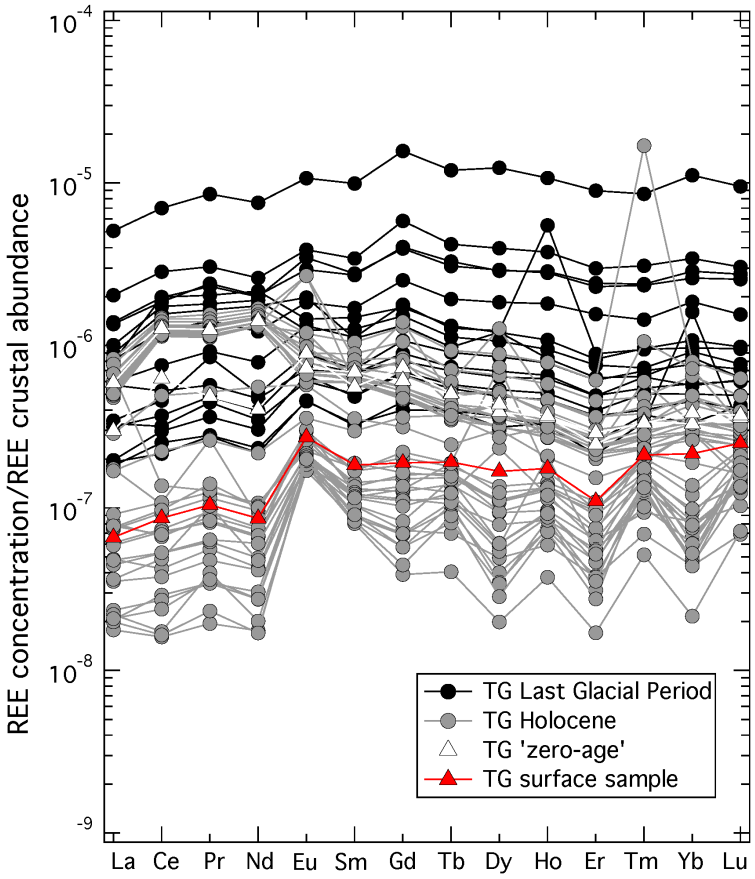

Figure 4.5. Normalized rare earth element concentrations of TG dust in ice with respect to mean crustal abundance (Wedepohl, 1995). Samples are separated by time periods (last glacial period, Holocene, 'zero-age') and by location (surface sample).

4.4.2 Chloride concentration

The Cl^- concentration (serving as a proxy for sea salt) from TG ice follows the general pattern from EPICA Dome C (EDC) (Wolff, 2006) from ~45-19 ka, but in general is higher in concentration (Figure 4.6). Following the retreat of the Ross Ice Shelf to Drygalski ice tongue (~17 ka, Figure 4.6), the Cl^- concentration remains high then experiences lower concentrations during the period of ~15-0 ka, however the TG record is considerably higher than the concentrations measured from the EDC ice core.

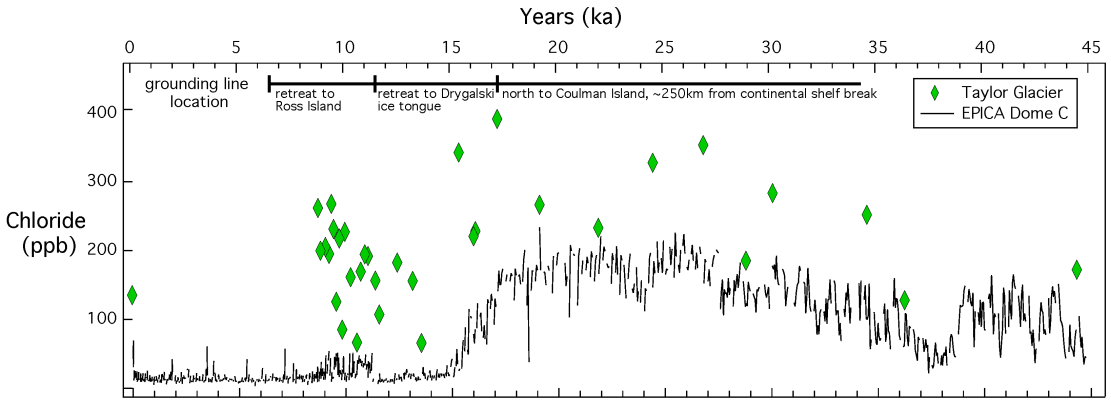

Figure 4.6. Chloride concentration of Taylor Glacier ice (green diamonds) from ~45-0 ka with EPICA Dome C (Wolff, 2006) (black line) for comparison. Also shown is the grounding line location for the Ross Ice Shelf with respect to time.

4.4.3 Dust concentration and size distribution

The dust concentration of TG ice samples follows a similar pattern as EDC dust (Delmonte et al., 2004a), with generally higher concentrations during the LGP and lower concentrations following the transition into the Holocene (Figure 4.7a, Table 4.S4). Dust concentrations reach >1000 ppb during the LGP, and remain

<100 ppb during the Holocene. During the LGP, the fine fraction (0.6-5 μm diameter) of dust lies closer to the observed EDC dust concentration, whereas the coarser dust (5-10 μm diameter) is considerably less than the total dust flux to TG. Following the last deglaciation, the difference between fine and coarse dust concentration is smaller, suggesting that the input of coarser dust particles is larger despite the lower overall dust concentration during the Holocene. The surface sample, N91-surface (red symbols, Figure 4.7a), displays similar dust particle diameter and concentration with respect to the remaining TG samples. In general, the size sorting of dust particles during the Holocene is poor compared to the LGP, which has lognormal size distributions with an average dust particle diameter of ~2 μm (Figure 4.S1). Additionally, the relative input of dust particles >5 μm is larger during the Holocene, which is also observed at Talos Dome, another coastal East Antarctic site (Albani et al., 2012; Delmonte et al., 2010). The presence of larger dust particles during the Holocene is not observed in ice cores from the Central East Antarctic Plateau (Delmonte et al., 2004b).

To analyze the relative input of fine versus coarse dust particles, we define a parameter, $R_{FP/CP}$, which is the concentration of fine dust (0.6-5 μm diameter) with respect to the coarse dust (5-10 μm diameter). The $R_{FP/CP}$ parameter shows a higher relative input of fine particles during the LGP compared to the Holocene (Figure 4.7b), which is also observed at EDC (Delmonte et al., 2004b; Lambert et al., 2008). It may be assumed that the dust 5-10 μm in diameter is originating from local dust sources (Delmonte et al., 2010), and that the dust particles 0.6-5

μm in diameter are most likely a mix of local and more distal sources. The $R_{FP/CP}$ parameter therefore, allows further interpretation of dust provenance. We have also included the $R_{FP/CP}$ parameter of samples from the Taylor Dome ice core (Aarons et al., In Press), to provide a more complete time series analysis (Figure 4.7b). Similar to the dust concentration data, the $R_{FP/CP}$ parameter decreases significantly following the deglaciation, which occurred in Antarctica at 18.2 ± 0.7 kyr BP (Stenni et al., 2011) (Figure 4.7b). During the early Holocene, TG experienced a large variability in the $R_{FP/CP}$ parameter, but with a generally decreasing trend (Figure 4.7b). It is also worthwhile to note that the 'zero-age' sample (R01) has a higher $R_{FP/CP}$ than the majority of the Holocene samples (Figure 4.7b).

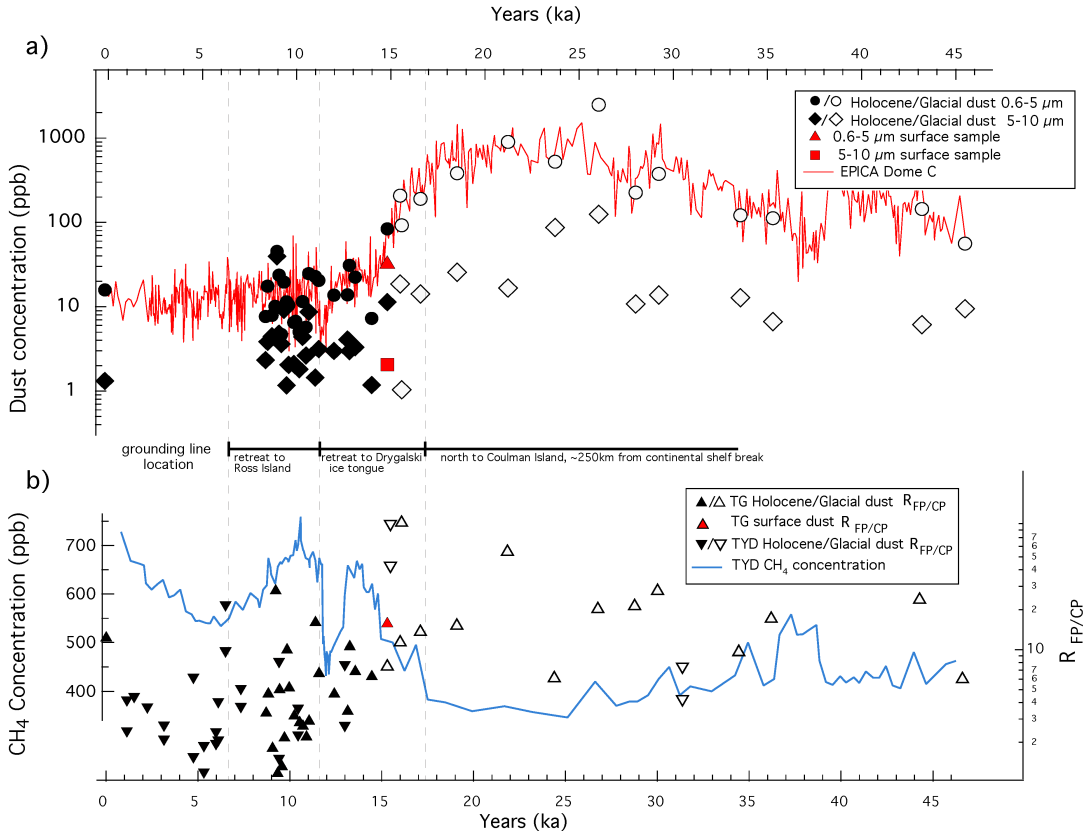

Figure 4.7. Dust concentration with respect to time and ratio of fine to coarse dust ($R_{FP/CP}$) throughout time period studied. a) Dust concentration of Holocene and Glacial dust in 2 size fractions: 0.6-5 μm (black and white circles for Holocene and Glacial respectively) and 5-10 μm (black and white diamonds for Holocene and Glacial respectively). A surface sample (N91 surface) is shown as red diamond and square for 0.6-5 and 5-10 μm size fractions respectively. Also shown is dust concentration of EPICA Dome C (Delmonte et al., 2004a) (red line). b) Ratio of fine to coarse dust from Holocene and Glacial periods in TG samples (black and white triangles respectively), surface sample (red triangle), and Taylor Dome ice core samples (black and white inverted triangles respectively) (Aarons et al., In Press). Also shown is the CH_4 concentration from Taylor Dome (Brook et al., 2000) (blue line).

4.4.4 Radiogenic isotopic composition

Similar to radiogenic isotopes of dust (insoluble fraction) measured in Taylor Dome ice, the Holocene samples cover a broader range of Sr and Nd isotopic composition compared to the LGP samples (Aarons et al., In Press) (Figure 4.4). The TG $^{87}Sr/^{86}Sr$ ratio ranges from 0.708000-0.711300 during the LGP versus 0.707556-0.714944 during the Holocene (Table 4.1, Figure 4.8). The surface sample, 'N91 surface', is the most radiogenic with respect to Sr, at 0.733621 (Table 4.1, Figure 4.8). The Nd isotopic compositions of LGP dust range from ε_{Nd}= -3.9 to 0.1 versus -8.2 to 1.9 during the Holocene (Table 4.1, Figure 4.7). The majority of insoluble Holocene samples are more radiogenic with respect to Sr (average Holocene=0.711322 versus average LGP=0.709456), which has also been observed in ice from the Taylor Dome ice core (Aarons et al., In Press). The average Nd isotopic composition becomes less radiogenic during the Holocene (average Holocene ε_{Nd} = -3.9 versus average LGP = -2.4).

Sample ID	Latitude (S)	Longitude (E)	Approximate age (yr BP)	$^{87}Sr/^{86}Sr$	Sr $\pm 2\sigma 10^{-6}$	$\epsilon_{Nd} \pm 2\sigma 10^{-6}$	Nd $\pm 2\sigma$
N203	77°45.613'	161°43.424'	46711	0.710785	38	-3.9	0.7
N196	77°45.612'	161°43.408'	44374	0.709805	25	-2.4	0.5
N168	77°45.599'	161°43.360'	36281	0.709407	41	0.1	0.3
N161	77°45.596'	161°43.349'	34510	0.711300	86	-3.0	2.3
N147	77°45.592'	161°43.339'	30080	0.709926	9	-3.3	0.6
N140	77°45.589'	161°43.311'	28828	0.709370	37	-2.9	0.4
N133	77°45.586'	161°43.301'	26820	0.708000	32	-1.6	0.2
N126	77°45.583'	161°43.286'	24446	0.708870	47	-1.6	0.2
N119	77°45.580'	161°43.272'	21891	0.708324	28	-1.5	0.2
N112	77°45.578'	161°43.277'	19130	0.708144	45	-1.1	0.2
N105	77°45.574'	161°43.260'	17138	0.710348	142	-	-
N98	77°45.562'	161°43.250'	16116	0.708496	30	-1.4	0.4
N91	77°45.571'	161°43.238'	15333	0.710151	27	-4.9	3.9
P20	77°45.528'	161°43.033'	16035	-	-	-3.1	1.5
P40	77°45.487'	161°43.098'	14491	0.7109740	40	-3.5	0.4
P60	77°45.511'	161°42.961'	13588	0.711238	59	-3.0	0.9
P75	77°45.508'	161°42.943'	13174	0.713714	117	-	-
P90	77°45.499'	161°42.912'	12446	0.710207	24	-4.7	1.1
P110	77°45.493'	161°42.869'	11609	0.710167	95	-4.6	0.7
P115	77°45.492'	161°42.861'	11419	0.709306	63	-	-
P125	77°45.488'	161°42.848'	11071	-	-	-	-
P130	77°45.486'	161°42.832'	10927	0.711525	64	-2.3	0.8
P140	77°45.481'	161°42.820'	10735	0.711879	111	-5.6	3.2
P145	77°45.479'	161°42.807'	10557	0.710797	142	-	-
P155	77°45.475'	161°42.794'	10259	0.707556	101	-	-
P165	77°45.471'	161°42.776'	10082	-	-	-	-
P170	77°45.470'	161°42.768'	9980	0.711790	164	-5.0	4.3
P175	77°45.468'	161°42.757'	9864	0.712290	38	-4.1	1.1
P180	77°45.465'	161°42.753'	9722	-	-	-	-
P185	77°45.463'	161°42.750'	9587	0.712877	70	-7.8	3.2
P190	77°45.462'	161°42.728'	9458	0.713742	64	-1.1	1.3
P195	77°45.461'	161°42.719'	9351	0.713899	212	-	-
P200	77°45.457'	161°42.706'	9247	0.708625	120	-7.2	3.2
P205	77°45.455'	161°42.696'	9076	0.708355	58	-2.7	0.4
P210	77°45.455'	161°42.695'	8843	0.711243	61	1.9	2.2
P215	77°45.454'	161°42.687'	8725	0.711306	73	-2.4	3.4
R01	77°41.513'	160°57.849'	0	0.714944	65	-6.9	1.2
N91-Surface	77°45.571'	161°43.238'	15333	0.733621	32	-8.2	1.2

Table 4.1. Radiogenic isotope compositions of dust from Taylor Glacier ice samples. Sample names, strontium and neodymium isotopic compositions of ice core samples measured in this study, latitude, longitude, and approximate age based on a previously established timescale (Baggenstos, 2015) are noted. See Table 4.S5 for radiogenic isotope compositions of Taylor Glacier soluble samples.

The soluble fraction has more uniform Sr and Nd isotopic compositions compared to the insoluble fraction (Table 4.S5, Figure 4.8). The average soluble TG $^{87}Sr/^{86}Sr$ ratio is 0.708577 during the LGP and 0.709023 during the Holocene, both are close to the established seawater $^{87}Sr/^{86}Sr$ seawater composition of 0.70917 (Hodell et al., 1990). The average soluble TG ε_{Nd} composition decreases following the transition from LGP to the Holocene shifting from -0.6 to -1.9 respectively.

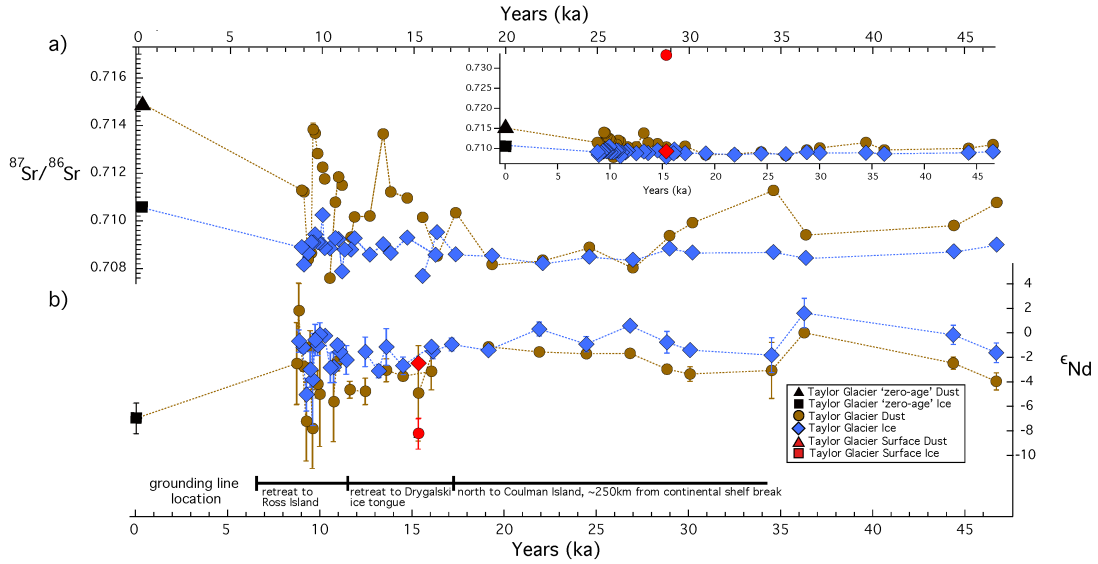

Figure 4.8. Radiogenic isotopic composition of Taylor Glacier insoluble dust and ice throughout time. a) Strontium isotopic composition of Taylor Glacier dust (brown circles) and ice (blue diamonds). Inset figure shows Taylor Glacier surface sample dust (red triangle) and ice (red square) Sr isotopic composition. In many cases symbol size is larger than error bar. b) Neodymium isotopic composition of Taylor Glacier dust (brown circles) and ice (blue diamonds) along with Taylor Glacier surface sample dust (red triangle) and ice (red square). Also shown is the grounding line location of the Ross Ice Shelf.

The combined Sr and Nd isotopic signatures of the samples vary based on age, as plotted in Figure 4.9. The LGP samples plot within the SSA source area, as defined by Delmonte et al. (2004a) and Gaiero (2007) (Figure 4.9). The Holocene samples are in general more radiogenic with respect to Sr, and plot as a potential mix of Ross Sea Sector potential source areas defined by Blakowski et al. (Blakowski et al., In Press). The 'zero-age' sample has an even more Sr radiogenic signature, and the surface sample (N91-surface) plots far outside the range of either LGP or Holocene samples (Figure 4.9). Further discussion of dust provenance based upon Sr and Nd isotopic signatures is provided below.

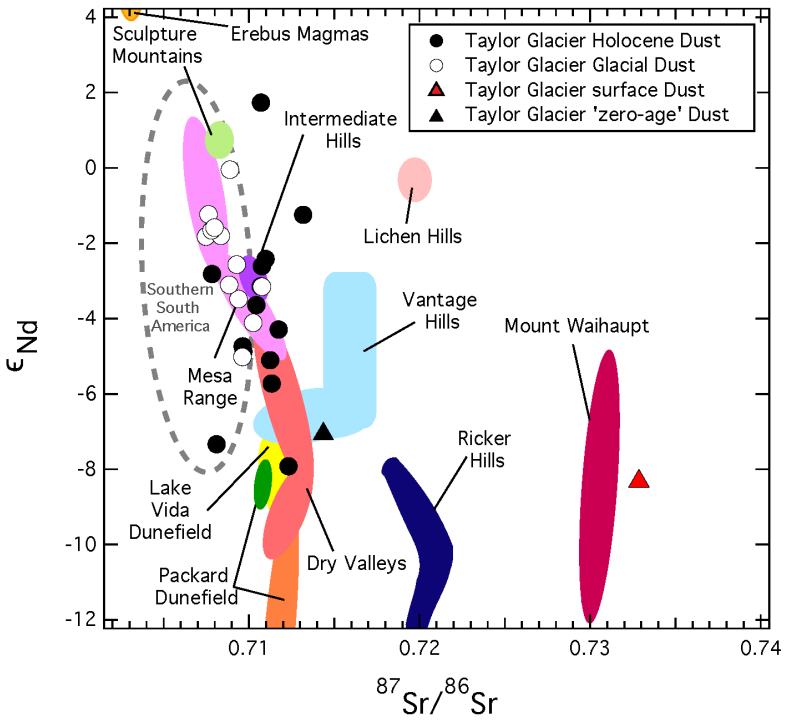

Figure 4.8. Radiogenic isotopic compositions of Taylor Glacier ice core dust and potential source areas. Sr and Nd isotopic compositions of Taylor Glacier ice core dust from Holocene (black circles) and Glacial dust (white circles) with regional potential source areas plotted in various colors (Blakowski et al., In Press; Delmonte et al., 2010; Sims et al., 2008). Long-range potential source area of Southern South America is plotted within dashed gray line (Delmonte et al., 2004a; Gaiero, 2007).

4.5. Discussion

Utilizing physical and chemical data of TG ice samples together provides the most accurate characterization of dust provenance, allowing us to determine whether the dust present within the ice is from a regional or proximal source. These data can be extended to make inferences on changes in regional climate that occurred following the transition from the LGP to the Holocene. In this study, we characterize dust sources by combining Cl^- concentration, Rb-Sr and Sm-Nd concentrations and isotopic compositions, dust concentration and size distribution, TE and REE concentrations to gain the most comprehensive

understanding of the dust sources, transport pathways, and inferred changes in atmospheric conditions.

4.5.1 Changes in dust concentrations and fluxes indicated by trace and rare earth elements

Combining and contrasting data from multiple chemical characterization techniques aids in distinguishing the sources of dust to TG during the time period of study. In this section we first discuss the evidence of shifting dust provenance provided by TE and REEs.

4.5.1.1 Variations in dust contributions inferred from crustal enrichment factors (EF_c)

We separate three groups of elemental concentrations by their behavior over the time period studied similar to the grouping used by Gabrielli et al. (2005). The grouping allows comparison between the TG and the East Antarctic ice core Vostok. The differences in observed elemental concentrations in the TG record may be attributed to variations in dust sources and pathways. The first group consists of Al, V, Mn, Rb, Nb, Ba and U, and is characterized by EF_c values close to 1 throughout the entire time period covered by the TG ice, which illustrates that the source of these elements in East Antarctica was primarily crustal dust throughout both a glacial and interglacial period. The second group of elements displays low EF_c values throughout the LGP and higher concentrations during the Holocene (Table 4.S1, Figure 4.4), which suggests that the atmospheric cycles of

Li, Na, Cr, Co, and Sr were primarily dominated by crustal dust during cold periods, whereas the shift in EF_c values during warmer periods may be the result of changes in dust source areas, soil conditions at the source (a shift in moisture saturation) or dust transport pathways. The third group (As and Bi) is higher in general compared to group 2 and has moderately high values during the LGP, and has been used as evidence of a SSA dust source to Antarctica (Gabrielli et al., 2005). The higher values of As and Bi during the Holocene are an indication of a more variable, uncharacterized source during this time.

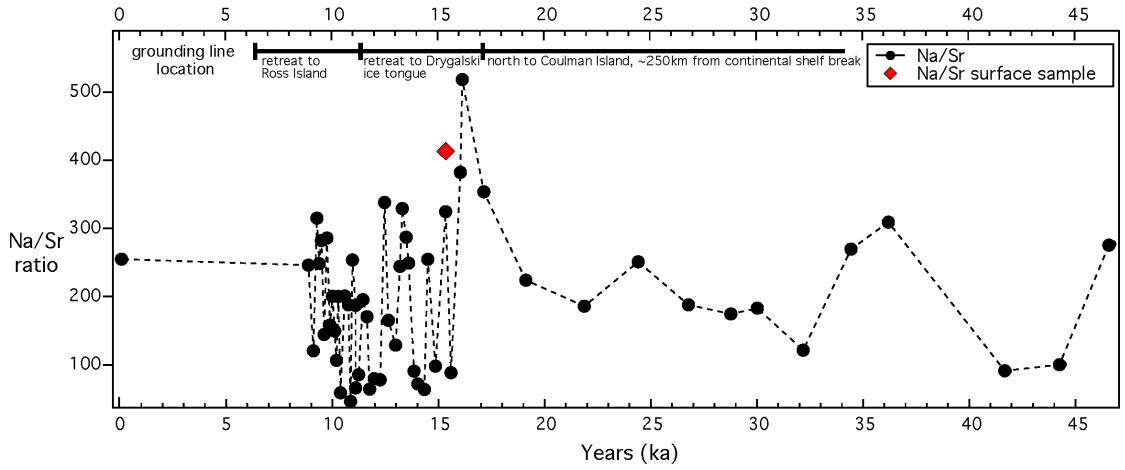

Figure 4.10. Sodium to strontium elemental ratio of Taylor Glacier ice (black circles) and a surface sample (red diamond) during time period studied. Grounding line location of Ross Ice Shelf is also shown.

4.5.1.2 Contributions from sea salt

Another source of TEs to ice sheets and glaciers is sea salt contribution, which can be estimated by calculating the Na to Sr ratio (Figure 4.10) (Aarons et al., In Press). The average upper continental crust Na/Sr ratio is 81 (Wedepohl, 1995) compared to that of seawater at 1358 (Riley and Tongudai, 1967). The TG TE concentrations are both the soluble and insoluble portion of the ice core, and are

representative of sea salt and mineral dust input. In our TG samples, the average Na/Sr ratio is higher during the LGP (~240) compared to the Holocene (~185). The higher Na/Sr ratio during the LGP compared to the Holocene (Table 4.S1) suggests a higher input of sea salt originating from frost flowers on newly formed sea ice. Alternatively, the higher sea salt concentrations could be a reflection of gustier conditions during the LGP, which has been attributed as the cause of increased mineral dust emissions (McGee et al., 2010). The surface sample (N91-surface) has a slightly higher Na/Sr ratio than its counterpart (N91) (Figure 4.10), which could be a reflection of sea salt input to the TG surface as it flows towards the Ross Sea through the McMurdo Dry Valleys.

4.5.1.3 Rare earth element evidence of shifting dust source

The REE patterns for the TG samples have a similar, temporally invariable profile throughout the LGP, however, the majority of samples from the Holocene display a positive Eu anomaly (Figure 4.5) also observed in the Taylor Dome ice core record (Aarons et al., In Press). The positive Eu anomaly is also found in young volcanic source area dust from Patagonia, however our Holocene dust isotopic compositions are not similar to observed Southern South America isotopic compositions (Figure 4.9). It should also be noted that the 'zero-age' sample (R01) does not display this pronounced positive Eu anomaly, suggesting that the dust source may have changed throughout the Holocene.

4.5.2 Chloride as an indicator of ice cover in the Ross Sea

Chemical and isotopic proxies of sea salt in the ice core record serve as indicators of past sea ice and ice shelf extent (Lupker et al., 2010; Wolff, 2006). Aerosol sea salt can originate from sea ice covered with brine and frost flowers, bubble bursting over open seawater or from open leads in sea ice. Chloride concentration is used as an indicator of sea salt in previous ice cores studies (Aristarain and Delmas, 2002; Aristarain et al., 2004), assuming that high levels of Cl^- detected in ice cores is primarily sourced from dry deposition of coarse sea salt particles uplifted by strong winds (Aristarain et al., 2004). The TG Cl^- concentrations are higher than the EDC record (Wolff, 2006), and follow a similar trend, until the Holocene when the Cl^- concentrations in the TG are much higher (Figure 4.6). The highly variable Cl^- concentrations observed in the TG ice during the Holocene coincide with the opening of the Ross Sea, and could be a result of bubble bursting over seawater (Figure 4.6). The higher, more stable Cl^- concentrations present in TG during the LGP may be due to the increased formation, transport and deposition of sea salt aerosol from sea ice, which has been observed in other East Antarctic ice core records (Petit et al., 1999; Wolff, 2006).

4.5.3 Relationship between climate shifts, Ross Ice Shelf retreat, and dust variation

Ice core records of CH_4 concentration have been used to indicate terrestrial climate conditions over long timescales (Blunier et al., 1995; Blunier et al., 1993; Brook et al., 2000; Chappellaz et al., 1990; Chappellaz et al., 1993; Jouzel et al., 1993; Petit et al., 1999). The CH_4 concentration from Taylor Dome (Brook et al.,

2000) is shown in Figure 4.7b, and is clearly correlated with the timing of the retreat of the Ross Ice Shelf. Methane concentrations are fairly low and stable at ~400 ppb during the LGP, and begin to slowly rise at ~17 ka coincident with the retreat of the Ross Ice Shelf to Coulman Island (Figure 4.7b). The CH_4 concentration continues to rise rapidly at the start of the Bølling-Allerød period (~14.8 ka) and remained between 600-700 ppb except during the CH_4 oscillation during the Antarctic Cold Reversal (ACR), which is distinguishable in the Taylor Dome record between ~13 and 11.5 ka (Figure 4.7b). The Ross Ice Shelf retreated to Drygalski ice tongue at the end of the ACR, and reached the Ross Island grounding line location ~6.5 ka.

The $R_{FP/CP}$ parameter (Figure 4.7b) provides insight into dust particle size deposited on TG, and this in turn is a reflection of distance to source and wind strength. The CH_4 concentration in the Taylor Dome record begins to increase ~17 ka, however the $R_{FP/CP}$ values of dust particles remain high until ~15.5 ka (Figure 4.7b), and a similar lag in dust particle size distribution can be noted following the ACR (higher $R_{FP/CP}$ value at ~11.5 ka). The direct correlation between climate shifts reflected in the CH_4 record and retreat in the Ross Ice Shelf is a reflection on ice sheet sensitivity to climate change. The retreat in the Ross Ice Shelf preceded the shifts in dust particle size variation observed in the TG record (Figure 4.7b), and the lag in $R_{FP/CP}$ values therefore suggests that variations in dust sources and transport pathways at a coastal East Antarctic site are closely coupled to ice sheet extent and retreat.

4.5.4 Sr and Nd isotopes

A powerful proxy for dust provenance determination is variation in the Sr and Nd isotopic isotopic composition (Biscaye et al., 1997; Grousset and Biscaye, 2005; Grousset et al., 1992). These tracers are considered robust indicators of source because the ratio of radiogenic to stable isotopic compositions do not fractionate during transport and show variability between source regions due to the varying geologic history and crustal age of each PSA. The combined Sr ($^{87}Sr/^{86}Sr$) and Nd ($^{143}Nd/^{144}Nd$) isotopic composition has been proven to be an excellent "fingerprint" of dust source (Grousset and Biscaye, 2005). It has been demonstrated that Sr isotopic ratios are size fraction dependent (Biscaye et al., 1997; Dasch, 1969), whereas Nd isotopes are less sensitive to size fraction in loess and desert sands (Chen et al., 2007; Rao et al., 2006; Yokoo et al., 2004). Weathering is also noted to affect Sr isotopic ratios: the leaching of carbonates with low $^{87}Sr/^{86}Sr$ ratios results in an increase of the bulk sample's $^{87}Sr/^{86}Sr$ ratio with weathering, and leaching of radiogenic Sr from biotite leaves bulk soils with much lowered $^{87}Sr/^{86}Sr$ ratio (Blum and Erel, 1997b).

4.5.4.1 Possible explanations of variable Sr and Nd isotope compositions

The TG Holocene samples in general have larger dust particle diameters (Figure 4.S1, 4.7b), however they are more radiogenic with respect to Sr (Figure 4.8a, 4.9), which is the opposite of what has been observed in aerosol mineral dust $^{87}Sr/^{86}Sr$ compositions separated by size fraction (Aarons et al., 2013). Previous

work has shown the systematic shift of >400 ppm in Sr isotope compositions of fine aerosol mineral dust compared to its coarse counterpart (Aarons et al., 2013). The observed shift in Sr isotopic composition is indicative of a change in source area, rather than a byproduct of weathering. The more variable Sr and Nd isotopic compositions observed during the Holocene compared to the LGP is another indicator that the sources of dust to TG have shifted from a constant, long-range source during the LGP to a more irregular source following the deglaciation.

To assess the potential input of surface contaminating dust, we analyzed the Sr and Nd isotopic composition of a surface sample (N91-surface), which had a very radiogenic Sr dust composition (see inset, Figure 4.8a). The observed Nd isotopic composition was considerably lower than its subsurface counterpart (N91), and the combined Sr-Nd isotopic composition suggests that any very close range dust input to TG is not diminishing the signal of long range and regionally transported dust (Figure 4.9). It is unlikely that the surface contamination is coming directly from the TG moraine material, which measures between $^{87}Sr/^{86}Sr$=0.710-0.712 (Blakowski et al., In Press).

All of the samples from the LGP plot within or on the source area designation for SSA (Figure 4.9), which has been noted to be the dominant source of dust to East Antarctica during this time period (Delmonte et al., 2010; Delmonte et al., 2004a). The Holocene samples span a broader range of Sr and Nd isotopic

composition and are most likely a mixture of Ross Sea Region dust sources previously identified (Blakowski et al., In Press).

4.5.5 Effect of dust particle size on radiogenic isotope composition

The $R_{FP/CP}$ parameter combined with the Sr and Nd isotopic composition allows analysis of the effect of dust grain size on observed $^{87}Sr/^{86}Sr$ ratios and ε_{Nd} composition (Figure 4.11). Dasch (1969) demonstrated that decreasing grain size leads to higher observed $^{87}Sr/^{86}Sr$ ratios due to the incongruent weathering processes of Rb and Sr, however, the Sr isotope composition is also dependent upon the weathering of minerals such as biotite (Blum and Erel, 1997a). Rubidium-bearing minerals (i.e. micas and feldspar) can be more resistant to chemical weathering compared to Sr-bearing minerals (i.e. plagioclase and calcite) (Dasch, 1969; Faure, 1986), therefore the Sr isotopic ratios should increase in older, more weathered materials. In most cases, Nd is released congruently during weathering processes, that is, the observed isotopic composition of Nd should not differentiate based on degree of weathering (Garcon et al., 2013; Goldstein et al., 1984), however minor isotopic shifts between dissolved Nd isotopes and weathered lithologies have been observed (Andersson et al., 2001). Previous studies of dust demonstrated that the observed Nd isotopic composition varied negligibly between the different size fractions (Chen et al., 2007; Feng et al., 2011; Grousset et al., 1992; Kanayama et al., 2005; Meyer et al., 2011).

The isotopic variation does not follow a linear trend on a Sr-Nd isotope diagram. The largest Sr and Nd isotope variation occurs at low $R_{FP/CP}$ values (<10), which are primarily Holocene samples (Figure 4.11). If a linear relationship between the $R_{FP/CP}$ values and Sr and Nd isotopic composition existed, this would indicate that the observed radiogenic isotopic compositions are a result of weathering processes. The high $R_{FP/CP}$ values do not correspond to radiogenic Sr (Figure 4.11a) or unradiogenic Nd (Figure 4.11b), and we infer this to reflect a change in provenance rather than grain-size related fractionation.

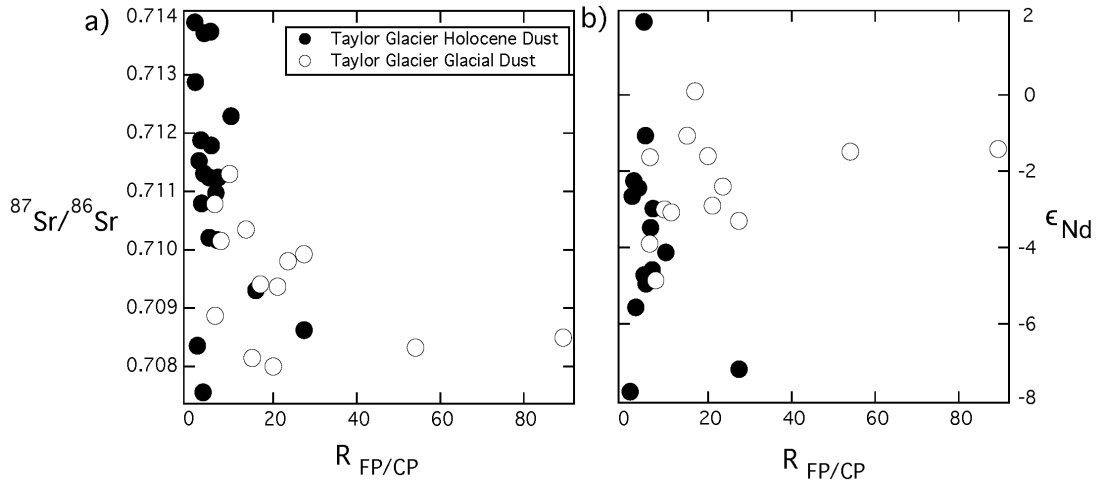

Figure 4.11. Radiogenic isotopic compositions of dust and the ratio of fine to coarse dust ($R_{FP/CP}$). a) Strontium isotopic composition as a function of $R_{FP/CP}$ of dust. b) Neodymium isotopic composition as a function of $R_{FP/CP}$ of dust. Holocene and Glacial samples are represented by black and white circles respectively.

4.5.6 A new source of dust to East Antarctica?

The sources of dust to East Antarctica during the Holocene have been traced to SSA (Basile et al., 1997; Delmonte et al., 2004a; Gaiero, 2007; Grousset et al., 1992), however it has been noted that the Sr and Nd isotopic composition of dust in East Antarctic ice overlaps with dust originating from the Australian Lake Eyre

Basin (Revel-Rolland et al., 2006). Our 'zero-age' sample, R01, has a $R_{FP/CP}$ value higher than the majority of Holocene samples (Figure 4.7b), suggesting that the dust originates from a more distal source. The $^{87}Sr/^{86}Sr$ ratio of sample R01 is more radiogenic than all other samples (Figure 4.8a, 4.9) excluding the surface sample, N91-surface. The Nd isotopic composition is notably very negative, lying on the periphery of the remaining Holocene samples cluster (Figure 4.8b, 4.9). When viewed in context of the Sr-Nd isotope plot of Southern Hemisphere PSA's (Figure 4.S2) sample R01 lies within the established Australian source area (Delmonte et al., 2004a; Revel-Rolland et al., 2006), suggesting Australia as a possible dust source to East Antarctica. The observed $^{87}Sr/^{86}Sr$ and ε_{Nd} isotope compositions for Australian dust are 0.709-0.732 and -3- -15 respectively (Revel-Rolland et al., 2006), and sample R01 lies well within those boundaries ($^{87}Sr/^{86}Sr$=0.714944 and ε_{Nd}=-6.9). Although the Sr and Nd isotopic compositions are quite variable and the recent input of Australian dust to East Antarctica is supported only by one combined Sr-Nd data point, this conclusion is detected by satellite and meteorological observations (Revel-Rolland et al., 2006).

4.6. Conclusions

The combined physical and chemical analyses of TG ice provides the first high-resolution time record of dust input to a coastal East Antarctic site during a full transition from the LGP to the Holocene. We combine timeseries of multiple chemical and physical parameters throughout time to trace the effect of the Ross

Ice Shelf retreat following the transition into the Holocene. The isotopic compositions combined with dust concentration, size distribution, trace and rare earth element concentrations and Cl^- measurements of TG ice suggest a shift in dust source provenance. It is likely that the sources of dust to TG have changed from the SSA during the LGP to more varied local sources during the Holocene, and the transport pathways are possibly still evolving as a 'zero-age' sample appears uniquely different than the remaining Holocene samples. The retreat in the Ross Ice Shelf is strongly correlated with large-scale climate shifts (CH_4 concentration) and preceded the shifts in dust particle size variation in the TG record by several thousand years. The lag in $R_{FP/CP}$ values is indicative of a shift in dust sources and transport pathways as a result of the Ross Ice Shelf retreat. To accurately determine the dust sources during the Holocene it would be beneficial to characterize more Antarctic PSAs in different size fractions as this would have an effect upon observed isotopic compositions.

4.7 References

Aarons, S.M., Aciego, S.M., Gabrielli, P., Delmonte, B., Koornneef, J.M., Wegner, A., Blakowski, M.A., In Press. The impact of glacier retreat from the Ross Sea on local climate: characterization of mineral dust in the Taylor Dome ice core, East Antarctica. Earth and Planetary Science Letters.

Aarons, S.M., Aciego, S.M., Gleason, J.D., 2013. Variable Hf-Sr-Nd radiogenic isotopic compositions in a Saharan dust storm over the Atlantic: Implications for dust flux to oceans, ice sheets and the terrestrial biosphere. Chemical Geology 349-350, 18-26.

Aciego, S.M., Bourdon, B., Lupker, M., Rickli, J., 2009. A new procedure for separating and measuring radiogenic isotopes (U, Th, Pa, Ra, Sr, Nd, Hf) in ice cores. Chemical Geology 266, 194-204.

Aciego, S.M., Cuffey, K.M., Kavanaugh, J.L., Morse, D.L., Severinghaus, J.P., 2007. Pleistocene ice and paleo-strain rates at Taylor Glacier, Antarctica. Quaternary Research 68, 303-313.

Albani, S., Delmonte, B., Maggi, V., Baroni, C., Petit, J.R., Stenni, B., Mazzola, C., Frezzotti, M., 2012. Interpreting last glacial to Holocene dust changes at Talos Dome (East Antarctica): implications for atmospheric variations from regional to hemispheric scales. Climate of the Past 8, 741-750.

Andersson, P.S., Dahlqvist, R., Ingri, J., Gustafsson, O., 2001. The isotopic composition of Nd in a boreal river: a reflection of selective weathering and colloidal transport. Geochimica Et Cosmochimica Acta 65, 521-527.

Aristarain, A.J., Delmas, R.J., 2002. Snow chemistry measurements on James Ross Island (Antarctic Peninsula) showing sea-salt aerosol modifications. Atmospheric Environment 36, 765-772.

Aristarain, A.J., Delmas, R.J., Stievenard, M., 2004. Ice-core study of the link between sea-salt aerosol, sea-ice cover and climate in the Antarctic Peninsula area. Climatic Change 67, 63-86.

Baggenstos, D., 2015. Taylor Glacier as an archive of ancient ice for large-volume samples: Chronology, gases, dust, and climate, Earth Sciences. University of California, San Diego, Ann Arbor, MI, p. 148.

Barnes, E.A., Hartmann, D.L., 2012. Detection of Rossby wave breaking and its response to shifts of the midlatitude jet with climate change. Journal of Geophysical Research 117.

Basile, I., Grousset, F.E., Revel, M., Petit, J.R., Biscaye, P.E., Barkov, N.I., 1997. Patagonian origin of glacial dust deposited in East Antarctica (Vostok and Dome C) during glacial stages 2, 4 and 6. Earth and Planetary Science Letters 146, 573-589.

Bauska, T.K., 2013. Carbon cycle variability during the last millennium and last deglaciation. Oregon State University.

Beghin, P., Charbit, S., Dumas, C., Kageyama, M., Roche, D.M., Ritz, C., 2014. Interdependence of the growth of the Northern Hemisphere ice sheets during the last glaciation: the role of atmospheric circulation. Climate of the Past 10, 345-358.

Biscaye, P., Grousset, F., Revel, M., Van der Gaast, S., Zielinski, G., Vaars, A., Kukla, G., 1997. Asian provenance of glacial dust (stage 2) in the Greenland Ice Sheet project 2 ice core, Summit, Greenland. Journal of Geophysical Research 102, 765-781.
Blakowski, M.A., Aciego, S.M., Delmonte, B., Baroni, C., Salvatore, M.C., Sims, K.W.W., In Press. Sr-Nd-Hf isotope characterization of dust source areas in Victoria Land and the McMurdo Sound sector of Antarctica. Quaternary Science Reviews.
Bliss, A.K., Cuffey, K.M., Kavanaugh, J.L., 2011. Sublimation and surface energy budget of Taylor Glacier, Antarctica. Journal of Glaciology 57, 684-696.
Blum, J.D., Erel, Y., 1997a. Rb-Sr isotope systematics of a granitic soil chronosequence: The importance of biotite weathering. Geochimica Et Cosmochimica Acta 61, 3193-3204.
Blum, J.D., Erel, Y., 1997b. Rb-Sr isotope systematics of a granitic soil chronosequence: The importance of biotite weathering. Geochimica Et Cosmochimica Acta 61, 3193-3204.
Blunier, T., Chappellaz, J., Schwander, J., Stauffer, B., Raynaud, D., 1995. VARIATIONS IN ATMOSPHERIC METHANE CONCENTRATION DURING THE HOLOCENE EPOCH. Nature 374, 46-49.
Blunier, T., Chappellaz, J.A., Schwander, J., Barnola, J.M., Desperts, T., Stauffer, B., Raynaud, D., 1993. ATMOSPHERIC METHANE, RECORD FROM A GREENLAND ICE CORE OVER THE LAST 1000 YEAR. Geophysical Research Letters 20, 2219-2222.
Boutron, C.F., Patterson, C.C., Barkov, N.I. , 1990. The occurrence of zinc in Antarctic ancient ice and recent snow. Earth and Planetary Science Letters 101, 248-259.
Brook, E.J., et al., 1993. Chronology of Taylor Glacier advances in Arena Valley, Antarctica, using in situ cosmogenic 3He and 10Be. Quaternary Research 39, 11-23.
Brook, E.J., Harder, S., Severinghaus, J.P., Steig, E.J., Sucher, C.M., 2000. On the origin and timing of rapid changes in atmospheric methane during the last glacial period. Global Biogeochemical Cycles 14, 559-572.
Buizert, C., Baggenstos, D., Jiang, W., Purtschert, R., Petrenko, V.V., Lu, Z.T., Muller, P., Kuhl, T., Lee, J., Severinghaus, J.P., Brook, E.J., 2014. Radiometric Kr-81 dating identifies 120,000-year-old ice at Taylor Glacier, Antarctica. Proceedings of the National Academy of Sciences of the United States of America 111, 6876-6881.
Chappellaz, J., Barnola, J.M., Raynaud, D., Korotkevich, Y.S., Lorius, C., 1990. ICE-CORE RECORD OF ATMOSPHERIC METHANE OVER THE PAST 160,000 YEARS. Nature 345, 127-131.
Chappellaz, J., Blunier, T., Raynaud, D., Barnola, J.M., Schwander, J., Stauffer, B., 1993. SYNCHRONOUS CHANGES IN ATMOSPHERIC CH4 AND GREENLAND CLIMATE BETWEEN 40-KYR AND 8-KYR BP. Nature 366, 443-445.
Chen, J., Li, G.J., Yang, J.D., Rao, W.B., Lu, H.Y., Balsam, W., Sun, Y.B., Ji, J.F., 2007. Nd and Sr isotopic characteristics of Chinese deserts: Implications for

the provenances of Asian dust. Geochimica Et Cosmochimica Acta 71, 3904-3914.
Cook, K.H., Held, I.M., 1988. Stationary waves of the ice age climate. Journal of Climate 1, 807-819.
Dasch, E.J., 1969. STRONTIUM ISOTOPES IN WEATHERING PROFILES, DEEP-SEA SEDIMENTS, AND SEDIMENTARY ROCKS. Geochimica Et Cosmochimica Acta 33, 1521-1552.
Delmonte, B., Andersson, P., Hansson, M., Schoberg, H., Petit, J.-R., Basile-Doelsch, I., Maggi, V., 2008. Aeolian dust in East Antarctica (EPICA - Dome C and Vostok): Provenance during glacial ages over the last 800 kyr. Geophysical Research Letters 35.
Delmonte, B., Baroni, C., Andersson, P.S., Narcisi, B., Salvatore, M.C., Petit, J.-R., Scarchilli, C., Frezzotti, M., Albani, S., Maggi, V., 2013. Modern and Holocene aeolian dust variability from Talos Dome (Northern Victoria Land) to the interior of the Antarctic ice sheet. Quaternary Science Reviews 64, 76-89.
Delmonte, B., Baroni, C., Andersson, P.S., Schoberg, H., Hansson, M., Aciego, S., Petit, J.R., Albani, S., Mazzola, C., Maggi, V., Frezzotti, M., 2010. Aeolian dust in the Talos Dome ice core (East Antarctica, Pacific/Ross Sea sector): Victoria Land versus remote sources over the last two climate cycles. Journal of Quaternary Science 25, 1327-1337.
Delmonte, B., Basile-Doelsch, I., Petit, J., Maggi, V., Revel-Rolland, M., Michard, A., Jagoutz, E., Grousset, F., 2004a. Comparing the EPICA and Vostok dust records during the last 220,000 years: stratigraphical correlation and provenance in glacial periods. Earth-Science Reviews 66, 63-87.
Delmonte, B., Petit, J.R., Andersen, K.K., Basile-Doelsch, I., Maggi, V., Ya Lipenkov, V., 2004b. Dust size evidence for opposite regional atmospheric circulation changes over east Antarctica during the last climatic transition. Climate Dynamics 23, 427-438.
Delmonte, B., Petit, J.R., Basile-Doelsch, I., Jagoutz, E., Maggi, V., 2007. Late quaternary interglacials in East Antarctica from ice-core dust records. Developments in Quaternary Sciences 7, 53-73.
Delmonte, B., Petit, J.R., Maggi, V., 2002. Glacial to Holocene implications of the new 27000-year dust record from the EPICA Dome C (East Antarctica) ice core. Climate Dynamics 18, 647-660.
Faure, G., 1986. Principles of isotope geochemistry. John Wiley and Sons.
Feng, J.-L., Hu, Z.-G., Ju, J.-T., Zhu, L.-P., 2011. Variations in trace element (including rare earth element) concentrations with grain sizes in loess and their implications for tracing the provenance of eolian deposits. Quaternary International 236, 116-126.
Gabrielli, P., et al., 2010. A major glacial-interglacial change in aeolian dust composition inferred from Rare Earth Elements in Antarctic ice. Quaternary Science Reviews 29, 265-273.
Gabrielli, P., Planchon, F.A.M., Hong, S., Lee, K.H., Hur, S.D., Barbante, C., Ferrari, C.P., Petit, J.R., Lipenkov, V.Y., Cescon, P., Boutron, C.F., 2005. Trace elements in Vostok Antarctic ice during the last four climatic cycles. Earth and Planetary Science Letters 234, 249-259.

Gaiero, D.M., 2007. Dust provenance in Antarctic ice during glacial periods: from where in southern South America? Geophysical Research Letters 34.
Garcon, M., Chauvel, C., France-Lanord, C., Huyghe, P., Lave, J., 2013. Continental sedimentary processes decouple Nd and Hf isotopes. Geochimica Et Cosmochimica Acta 121, 177-195.
Goldstein, S.L., O'Nions, R.K., Hamilton, P.J., 1984. A Sm-Nd isotopic study of atmospheric dusts and particulates from major river systems. Earth and Planetary Science Letters 70, 221-236.
Grootes, P.M., Steig, E.J., Stuiver, M., Waddington, E.D., Morse, D.L., Nadeau, M.-J., 2001. The Taylor Dome Antarctic 18O Record and Globally Synchronous Changes in Climate. Quaternary Research 56, 289-298.
Grousset, F.E., Biscaye, P.E., 2005. Tracing dust sources and transport patterns using Sr, Nd and Pb isotopes. Chemical Geology 222, 149-167.
Grousset, F.E., Biscaye, P.E., Revel, M., Petit, J.-R., Pye, K., Joussaume, S., Jouzel, J., 1992. Antarctic (Dome C) ice-core dust at 18 k.y. B.P.: Isotopic constraints on origins. Earth and Planetary Science Letters 111, 175-182.
Hall, N.M.J., Valdes, P.J., Dong, B., 1996. The Maintenance of the Last Great Ice Sheets: A UGAMP GCM Study. Journal of Climate 9, 1004-1019.
Hammer, C., Clausen, H., Dansgaard, W., Neftel, A., Kristinsdottir, P., Johnson, E., 1985. Continuous impurity analysis along the Dye-3 deep core. Geophys. Monog. Series. 33, 90-94.
Hodell, D.A., Mead, G.A., Mueller, P.A., 1990. Variation in the strontium isotopic composition of seawater (8 Ma to present): Implications for chemical weathering rates and dissolved fluxes to the oceans. Chemical Geology 80, 291-307.
Jacobsen, S.B., Wasserberg, G.J., 1980. Sm-Nd Isotopic Evolution of Chondrites. Earth and Planetary Science Letters 50, 139-155.
Jouzel, J., Alley, R., Cuffey, K., Dansgaard, W., Grootes, P., Hoffmann, G., Johnsen, S., Koster, R., Peel, D., Shuman, C., Stievenard, M., Stuiver, M., White, J., 1997. Vaildity of the temperature reconstruction from water isotopes in ice cores. Journal of Geophysical Research: Oceans 102, 26471-26487.
Jouzel, J., Barkov, N.I., Barnola, J.M., Bender, M., Chappellaz, J., Genthon, C., Kotlyakov, V.M., Lipenkov, V., Lorius, C., Petit, J.R., Raynaud, D., Raisbeck, G., Ritz, C., Sowers, T., Stievenard, M., Yiou, F., Yiou, P., 1993. EXTENDING THE VOSTOK ICE-CORE RECORD OF PALEOCLIMATE TO THE PENULTIMATE GLACIAL PERIOD. Nature 364, 407-412.
Jweda, J., Bolge, L., Class, C., Goldstein, S.L., 2015. High Precision Sr-Nd-Hf-Pb Isotopic Compositions of USGS Reference Material BCR-2. Geostandards and Geoanalytical Research.
Kageyama, M., Valdes, P.J., 2000. Impact of the North American ice-sheet orography on the Last Glacial Maximum eddies and snowfall. Geophysical Research Letters 27, 1515.
Kanayama, S., Yabuki, S., Zeng, F.J., Liu, M.Z., Shen, Z.B., Liu, L.C., Yanagisawa, F., Abe, O., 2005. Size-dependent geochemical characteristics of Asian dust - Sr and Nd isotope compositions as tracers for source identification. Journal of the Meteorological Society of Japan 83A, 107-120.

Kavanaugh, J.L., Cuffey, K.M., 2009. Dynamics and mass balance of Taylor Glacier, Antarctica: 2. Force balance and longitudinal coupling. Journal of Geophysical Research 114.
Kuhl, T.W., Johnson, J.A., Shturmakov, A.J., Goetz, J.J., Gibson, C.J., Lebar, D.A., 2014. A new large-diameter ice-core drill: the Blue Ice Drill. Annals of Glaciology 55.
Laîné, A., Kageyama, M., Salas-Mélia, D., Voldoire, A., Rivière, G., Ramstein, G., Planton, S., Tyteca, S., Peterschmitt, J.Y., 2008. Northern hemisphere storm tracks during the last glacial maximum in the PMIP2 ocean-atmosphere coupled models: energetic study, seasonal cycle, precipitation. Climate Dynamics 32, 593-614.
Lambert, F., Delmonte, B., Petit, J.R., Bigler, M., Kaufmann, P.R., Hutterli, M.A., Stocker, T.F., Ruth, U., Steffensen, J.P., Maggi, V., 2008. Dust-climate couplings over the past 800,000 years from the EPICA Dome C ice core. Nature 452, 616-619.
Liakka, J., Nilsson, J., 2010. The impact of topographically forced stationary waves on local ice-sheet climate. Journal of Glaciology 56, 534-544.
Lupker, M., Aciego, S.M., Bourdon, B., Schwander, J., Stocker, T.F., 2010. Isotopic tracing (Sr, Nd, U and Hf) of continental and marine aerosols in an 18th century section of the Dye-3 ice core (Greenland). Earth and Planetary Science Letters 295, 277-286.
McGee, D., Broecker, W.S., Winckler, G., 2010. Gustiness: The driver of glacial dustiness? Quaternary Science Reviews 29, 2340-2350.
McIntyre, M.E., Palmer, T.N., 1983. Breaking planetary waves in the stratosphere. nature 305, 593-600.
Members, W.D.P., 2015. Precise interpolar phasing of abrupt climate change during the last ice age. Nature 520, 661-665.
Meyer, I., Davies, G.R., Stuut, J.-B.W., 2011. Grain size control on Sr-Nd isotope provenance studies and impact on paleoclimate reconstructions: An example from deep-sea sediments offshore NW Africa. Geochemistry Geophysics Geosystems 12.
Morse, D.L., 1997. Glacier Geophysics at Taylor Dome, Antarctica. University of Washington.
Morse, D.L., Waddington, E.D., Steig, E.J., 1998. Ice age storm trajectories inferred from radar stratigraphy at Taylor Dome, Antarctica. Geophysical Research Letters 25, 3383-3386.
Petit, J.R., Briat, M., Royer, A., 1981. Ice age aerosol content from East Antarctic ice core samples and past wind strength. Nature 293, 391-394.
Petit, J.R., Jouzel, J., Raynaud, D., Barkov, N.I., Barnola, J.-M., Basile, I., Bender, M., Chappellaz, J., Davis, M., Delaygue, G., Delmotte, M., Kotlyakov, V.M., Legrand, M., Lipenkov, V.Y., Lorius, C., Pepin, L., Ritz, C., Saltzman, E., Stievenard, M., 1999. Climate and atmospheric history of the past 420,000 years from the Vostok ice core, Antarctica. Nature 399, 429-436.
Petrenko, V.V., Severinghaus, J.P., Schaefer, H., Smith, A.M., Kuhl, T., Baggenstos, D., Hua, Q., Brook, E.J., Rose, P., Kulin, R., Bauska, T., Harth, C., Buizert, C., Orsi, A., Emanuele, G., Lee, J.E., Brailsford, G., Keeling, R., Weiss,

R.F., 2016. Measurements of 14C in ancient ice from Taylor Glacier, Antarctica constrain in situ cosmogenic 14CH4 and 14CO production rates. Geochimica Et Cosmochimica Acta.
Rao, W.B., Yang, B., Chen, J.D., Lu, J., 2006. Sr-Nd isotope geochemistry of eolian dust of the arid-semiarid areas in China: Implications for loess provenance and monsoon evolution. Chinese Science Bulletin 51, 1401-1412.
Reeh, N., Oerter, H., Letreguilly, A., Miller, H., Hubberten, H.-W., 1991. A new, detailed ice-age oxygen-18 record from the ice-sheet margin in central West Greenland. Global and Planetary Change 4, 373-383.
Revel-Rolland, M., De Deckker, P., Delmonte, B., Hesse, P., Magee, J., Basile-Doelsch, I., Grousset, F., Bosch, D., 2006. Eastern Australia: a possible source of dust in East Antarctica interglacial ice. Earth and Planetary Science Letters 249, 1-13.
Riley, J.P., Tongudai, M., 1967. The major cation/chlorinity ratios in sea water. Chemical Geology 2, 263-269.
Rivière, G., Laîné, A., Lapeyre, G., Salas-Mélia, D., Kageyama, M., 2010. Links between Rossby wave breaking and the North Atlantic Oscillation-Arctic Oscillation in present-day and Last Glacial Maximum climate simulations. Journal of Climate 23, 2987-3008.
Sims, K.W.W., Blichert-Toft, J., Kyle, P.R., Pichat, S., Gauthier, P.-J., Blusztajn, J., Kelly, P., Ball, L., Layne, G., 2008. A Sr, Nd, Hf, and Pb isotope perspective on the genesis and long-term evolution of alkaline magmas from Erebus volcano, Antarctica. Journal of Volcanology and Geothermal Research 177, 606-618.
Spahni, R., Chappellaz, J., Stocker, T.F., Loulergue, L., Hausammann, G., Kawamura, K., Fluckiger, J., Schwander, J., Raynaud, D., Masson-Delmotte, V., Jouzel, J., 2005. Atmospheric Methane and Nitrous Oxide of the Late Pleistocene from Antarctic Ice Cores. Science 310, 1317-1321.
Steig, E.J., et al., 2000. Wisconsinan and Holocene climate history from an ice core at Taylor Dome, western Ross Embayment, Antarctica. Geographical Annals 82A, 213-235.
Stenni, B., Buiron, D., Frezzotti, M., Albani, S., Barbante, C., Bard, E., Barnola, J.M., Baroni, M., Baumgartner, M., Bonazza, M., Capron, E., Castellano, E., Chappellaz, J., Delmonte, B., Falourd, S., Genoni, L., Iacumin, P., Jouzel, J., Kipfstuhl, S., Landais, A., Lemieux-Dudon, B., Maggi, V., Masson-Delmotte, V., Mazzola, C., Minster, B., Montagnat, M., Mulvaney, R., Narcisi, B., Oerter, H., Parrenin, F., Petit, J.R., Ritz, C., Scarchilli, C., Schilt, A., Schupbach, S., Schwander, J., Selmo, E., Severi, M., Stocker, T.F., Udisti, R., 2011. Expression of the bipolar see-saw in Antarctic climate records during the last deglaciation. Nature Geoscience 4, 46-49.
Uglietti, C., Gabrielli, P., Olesik, J.W., Lutton, A., Thompson, L.G., 2014. Large variability of trace element mass fractions determined by ICP-SFMS in ice core samples from worldwide high altitude glaciers. Applied Geochemistry 47, 109-121.
Waddington, E.D., Conway, H., Steig, E.J., Alley, R.B., Brook, E.J., Taylor, K.C., White, J.W.C., 2005. Decoding the dipstick: Thickness of Siple Dome, West Antarctica, at the Last Glacial Maximum. Geology 33, 281-284.

Wedepohl, K.H., 1995. The composition of the continental crust. Geochimica Et Cosmochimica Acta 59, 1217-1232.
Wegner, A., Gabrielli, P., Wilhelms-Dick, D., Ruth, U., Kriews, M., De Deckker, P., Barbante, C., Cozzi, G., Delmonte, B., Fischer, H., 2012. Change in dust variability in the Atlantic sector of Antarctica at the end of the last deglaciation. Climate of the Past 8, 135-147.
Wolff, E.W., et al., 2006. Southern Ocean sea ice, DMS production and iron flux over the last eight glacial cycles. Nature 440, 491-496.
Yokoo, Y., Nakano, T., Nishikawa, M., Quan, H., 2004. Mineralogical variation of Sr-Nd isotopic and elemental compositions in loess and desert sand from the central Loess Plateau in China as a provenance tracer of wet and dry deposition in the northwestern Pacific. Chemical Geology 204, 45-62.

4.8 Supplementary Materials

4.8.1 Introduction

This supporting information file contains additional figures and tables describing the physical and chemical characteristics of the Taylor Glacier samples measured in this study. Table 4.S1 is the trace element raw concentrations and calculated crustal enrichment factors, Table 4.S2 is the rare earth element concentrations, Table 4.S3 is the chloride concentration, Table 4.S4 is the dust concentration and size distribution data, and Table 4.S5 is the geographic location, and strontium and neodymium radiogenic isotope composition of soluble Taylor Glacier samples. Figure 4.S1 is the particle size distributions of samples measured from Taylor Glacier and Figure 4.S2 is the radiogenic isotope compositions of potential source areas in the Southern Hemisphere.

4.8.1.1 Tables

		Raw Concentration (ppt)													
Approximate Age	Sample Name	Li	Na	Al	V	Cr	Mn	Co	As	Rb	Sr	Nb	Ba	Bi	U
	Blank 1	385.59	943.80	2039.46	4.52	67.91	21.94	4.14	2.72	10.31	777.88	1.04	18.80	0.14	0.18
	Blank 2	350.20	901.52	643.08	6.36	39.52	9.40	4.47	2.31	24.17	796.82	4.19	19.83	0.03	0.16
46711	N203	351.13	44311.59	8245.85	19.09	35.32	139.46	4.72	2.11	21.66	1619.06	3.16	68.43	0.09	0.47
44374	N196	327.67	93761.69	30004.21	601.62	101027.47	60560.33	2264.45	392.97	68.98	9304.89	19.68	722.11	14.10	8.06
41788	N189	277.73	98758.21	22614.43	578.68	100911.68	59850.79	2165.49	429.03	61.07	10760.30	19.57	607.14	14.00	7.39
36281	N168	360.60	80706.15	30208.13	49.61	61.03	705.05	14.20	8.85	67.48	2629.46	4.52	315.27	0.35	1.04
34510	N161	337.18	55942.26	11004.33	20.85	44.61	284.02	5.44	5.38	29.48	2087.84	1.85	101.81	0.15	0.66
32247	N154	259.38	135808.52	25986.74	571.93	100622.33	59736.28	2191.58	498.28	63.45	11155.17	19.47	637.73	14.21	7.75
30080	N147	389.21	75808.27	47212.53	88.67	53.71	752.01	16.63	14.18	107.06	4156.70	6.11	472.72	0.39	1.77
28828	N140	321.40	46604.67	16457.36	33.76	40.64	331.36	8.25	5.96	43.85	2678.07	4.62	158.45	0.29	0.83
26820	N133	494.26	261433.71	269393.85	483.15	201.27	4500.35	75.04	58.62	534.96	13955.97	35.08	2593.21	1.73	7.06
24446	N126	352.92	120654.02	68394.69	115.91	74.36	974.25	23.77	21.22	139.39	4836.68	9.09	719.82	0.57	2.13
21891	N119	369.54	101761.94	91170.94	155.01	81.48	1426.16	31.15	20.41	185.73	5492.69	10.90	1054.66	0.65	2.70
19130	N112	325.95	100276.85	69610.79	136.66	71.00	1093.10	21.48	17.30	143.20	4497.04	7.32	745.52	0.55	2.28
17138	N105	301.29	77091.69	17711.43	44.59	56.77	287.12	11.99	6.64	45.10	2197.42	2.02	187.95	0.22	0.74
16116	N98	381.60	109986.47	14600.76	27.87	32.30	199.11	7.15	23.23	36.94	2142.57	3.45	114.43	0.30	0.61
16035	P20	370.48	76679.81	17730.61	31.97	48.32	241.14	7.34	5.23	46.52	2023.87	4.58	147.09	0.14	0.67
15588	P25	285.43	94010.71	21190.77	573.38	100887.92	59509.47	2164.83	476.92	58.80	10544.92	20.53	596.43	14.56	7.92
15333	N91	311.47	51076.27	9132.82	16.75	42.28	160.93	7.81	4.93	24.89	1585.77	1.56	99.16	0.26	0.49
14849	P35	303.19	84180.76	19731.33	597.57	106147.60	62944.74	2324.44	567.73	60.46	8537.05	37.95	545.67	14.76	8.07

14491	P40	284.49	25102.96	2258.56	3.23	50.64	21.07	2.77	3.51	10.00	991.38	0.67	16.89	0.04	0.29
14328	P45	256.81	61468.86	15760.88	539.23	97590.26	57119.95	2069.86	420.10	47.07	9500.26	19.12	505.18	15.21	7.66
14019	P50	306.13	60351.04	11022.07	557.00	100901.84	59924.75	2190.10	405.06	41.55	8308.11	18.47	456.24	13.97	7.22
13835	P55	277.20	88256.95	13905.67	571.38	102221.74	60950.98	2284.83	465.26	51.20	9672.41	19.23	568.39	15.18	7.68
13588	P60	325.61	27237.33	2638.63	6.07	64.57	51.17	4.35	3.14	14.88	1099.73	1.70	51.39	0.18	0.39
13466	P65	318.22	119378.57	6863.07	199.95	37628.02	23236.27	880.87	173.44	37.46	4185.87	9.44	361.90	5.92	2.84
13286	P70	267.45	38951.24	3239.21	6.41	106.67	78.95	4.91	6.03	15.39	1192.15	0.97	50.15	0.13	0.33
13174	P75	300.59	26633.73	3659.16	7.82	169.17	57.16	4.78	4.03	21.69	1096.41	3.23	45.18	0.39	0.35
12970	P80	327.77	135673.33	17605.21	565.62	99921.33	58708.84	2321.89	449.06	65.38	10519.23	21.45	768.18	19.07	7.88
12630	P85	302.81	148288.51	15692.10	560.76	100050.86	59598.72	2321.91	483.61	67.00	8995.66	20.03	716.19	15.00	7.69
12446	P90	339.88	34927.84	1436.83	3.72	33.93	32.93	2.20	2.07	12.68	1041.60	1.24	21.28	0.06	0.30
12238	P95	304.51	61050.69	11655.40	577.31	104353.49	61895.38	2260.79	471.30	42.84	7735.54	19.06	464.83	14.38	7.58
11950	P100	297.42	59777.86	10853.79	531.27	95777.43	56638.48	2078.81	431.43	43.71	7429.31	17.63	540.21	14.23	7.21
11741	P105	287.23	49159.98	12100.81	554.35	100036.86	59534.38	2158.37	525.31	42.60	7545.27	19.29	443.82	13.50	7.31
11609	P110	289.08	16989.67	2318.40	4.98	153.91	38.92	3.41	1.20	9.82	998.47	1.17	33.37	0.15	0.31
11419	P115	274.46	19340.00	3763.83	6.42	27.65	44.74	2.71	2.01	13.74	992.87	1.39	54.41	0.05	0.33
11217	P120	284.88	67400.13	12572.39	549.39	98335.65	57397.36	2147.45	485.19	63.91	7814.47	19.61	548.74	14.99	7.62
11071	P125D	327.66	53235.37	12702.70	582.08	104152.06	61646.82	2389.85	414.40	48.96	7949.71	21.10	524.98	14.62	7.93
11071	P125	267.30	17701.40	2681.89	7.87	36.43	37.71	2.56	3.12	15.16	948.93	1.23	39.93	0.07	0.27
10927	P130	281.21	26603.94	2485.29	3.98	50.91	23.36	3.15	4.23	10.54	1055.28	0.68	32.23	0.10	0.25
10838	P135	295.11	37641.57	11875.27	569.17	104184.16	60709.29	2213.36	419.20	44.67	7934.15	19.62	477.51	15.20	7.53
10735	P140	262.32	16833.99	1677.42	6.67	26.95	24.80	2.28	2.22	8.53	899.19	0.92	227.92	0.04	0.29
10557	P145	357.4	17701.84	791.87	3.64	150.87	18.67	3.09	2.98	11.37	884.85	1.49	17.30	0.10	0.22

		3													
10360	P150	335.67	45308.46	12036.75	554.48	99239.19	58147.97	2123.78	435.57	45.21	7555.07	19.21	454.98	13.61	7.37
10259	P155	261.92	18184.27	1418.50	2.91	34.96	18.21	3.17	4.12	7.94	912.31	0.58	24.26	0.09	0.25
10170	P160	284.42	80861.50	12295.29	557.64	99369.47	58360.56	2164.07	384.53	54.60	7562.76	17.07	560.20	16.38	7.22
10082	P165	368.38	127863.84	12503.29	590.65	106567.34	61972.15	2345.21	408.44	52.52	8560.74	23.31	606.92	15.42	7.98
9980	P170	302.38	18876.71	2820.59	5.21	34.70	42.96	3.58	2.31	11.75	946.24	1.13	26.15	0.05	0.27
9864	P175	309.29	14504.09	2874.78	5.51	38.50	30.94	2.99	1.51	10.16	919.46	1.06	22.44	0.05	0.26
9722	P180	302.59	29055.01	2290.63	5.09	98.51	45.69	6.20	2.11	25.20	1022.98	1.37	40.14	0.14	0.31
9587	P185	289.18	12582.16	1453.23	2.15	45.98	17.42	2.90	7.54	16.19	871.55	0.56	15.33	0.24	0.19
9458	P190	382.48	28815.15	2019.31	4.68	145.76	43.67	2.78	4.96	16.60	1027.49	1.58	25.42	0.19	0.37
9351	P195	298.11	23503.68	1683.15	6.63	42.87	29.01	2.90	2.72	9.80	952.14	0.92	23.60	0.06	0.28
9247	P200	364.01	37109.19	1631.02	8.91	40.88	19.44	3.11	4.03	16.88	1186.65	1.15	17.22	0.06	0.31
9076	P205	275.74	11283.12	3464.38	5.76	23.50	26.72	2.36	3.92	18.47	934.22	0.85	76.55	0.05	0.26
8843	P210	342.37	26609.21	4061.31	8.23	46.86	83.98	3.46	4.73	29.68	1087.31	4.19	37.73	0.20	0.43
0	R01	419.09	37680.57	12342.90	10.35	55.02	229.27	34.99	7.84	66.45	1487.56	1.98	261.34	0.19	0.71
15333	N91-surface	272.55	53584.24	4478.31	8.54	29.63	55.97	4.15	3.22	14.80	1308.37	0.82	76.02	0.07	0.41
		Enrichment Factors													
Approximate Age	**Sample Name**	**Li**	**Na**	**Al**	**V**	**Cr**	**Mn**	**Co**	As	**Rb**	**Sr**	**Nb**	**Ba**	Bi	**U**
46711	N203_TE	70.5	7.6	0.5	1.6	4.5	1.2	1.8	4.7	0.9	22.6	0.5	0.5	3.2	0.8
44374	N196_TE	0.1	0.0	0.0	0.1	15.5	0.6	1.1	1.1	0.0	0.2	0.0	0.0	0.6	0.0
41788	N189_TE	0.1	0.0	0.0	0.1	15.9	0.6	1.0	1.2	0.0	0.2	0.0	0.0	0.6	0.0
36281	N168_TE	18.1	3.5	0.4	1.0	1.9	1.5	1.3	4.9	0.7	9.2	0.2	0.6	3.2	0.5
34510	N161_TE	43.3	6.2	0.4	1.1	3.6	1.5	1.3	7.6	0.8	18.7	0.2	0.5	3.4	0.7

32247	N154_TE	0.1	0.0	0.0	0.1	16.0	0.6	1.0	1.4	0.0	0.2	0.0	0.0	0.6	0.0
30080	N147_TE	14.1	2.4	0.5	1.3	1.2	1.1	1.1	5.7	0.8	10.5	0.2	0.6	2.6	0.6
28828	N140_TE	28.3	3.5	0.4	1.2	2.3	1.2	1.4	5.8	0.8	16.4	0.3	0.5	4.6	0.6
26820	N133_TE	3.3	1.5	0.5	1.4	0.9	1.3	1.0	4.4	0.7	6.6	0.2	0.7	2.1	0.4
24446	N126_TE	8.9	2.6	0.5	1.2	1.2	1.0	1.1	5.9	0.7	8.5	0.2	0.7	2.6	0.5
21891	N119_TE	7.6	1.8	0.5	1.3	1.0	1.2	1.2	4.6	0.8	7.8	0.2	0.8	2.4	0.5
19130	N112_TE	8.1	2.1	0.5	1.4	1.1	1.1	1.0	4.7	0.7	7.7	0.2	0.7	2.4	0.5
17138	N105_TE	21.7	4.8	0.4	1.3	2.6	0.9	1.6	5.3	0.7	11.0	0.1	0.5	2.8	0.5
16116	N98_TE	49.1	12.1	0.5	1.5	2.6	1.1	1.7	32.9	1.0	19.2	0.4	0.6	6.9	0.7
16035	P20_TE	36.2	6.4	0.5	1.3	3.0	1.0	1.4	5.6	0.9	13.8	0.4	0.5	2.5	0.6
15588	P25-D_TE	0.1	0.0	0.0	0.1	16.0	0.6	1.0	1.3	0.0	0.2	0.0	0.0	0.7	0.0
15333	N91_TE	57.6	8.1	0.5	1.3	4.9	1.2	2.7	10.0	0.9	20.4	0.2	0.7	8.7	0.8
14849	P35_TE	0.1	0.0	0.0	0.1	16.0	0.6	1.1	1.5	0.0	0.1	0.0	0.0	0.6	0.0
14491	P40_TE	260.4	19.7	0.6	1.2	29.1	0.8	4.8	35.4	1.8	63.2	0.5	0.6	7.0	2.3
14328	P45_TE	0.1	0.0	0.0	0.1	16.2	0.6	1.0	1.2	0.0	0.2	0.0	0.0	0.7	0.0
14019	P50_TE	0.1	0.0	0.0	0.1	15.9	0.6	1.0	1.1	0.0	0.1	0.0	0.0	0.6	0.0
13835	P55_TE	0.1	0.0	0.0	0.1	15.9	0.6	1.1	1.3	0.0	0.2	0.0	0.0	0.7	0.0
13588	P60_TE	137.7	9.9	0.3	1.1	17.2	0.9	3.5	14.6	1.3	32.4	0.6	0.8	13.6	1.4
13466	P65_TE	0.2	0.1	0.0	0.1	16.7	0.7	1.2	1.3	0.0	0.2	0.0	0.0	0.7	0.0
13286	P70_TE	85.4	10.7	0.3	0.8	21.4	1.1	3.0	21.2	1.0	26.5	0.3	0.6	7.2	0.9
13174	P75_TE	145.2	11.0	0.5	1.6	51.4	1.2	4.4	21.4	2.1	36.9	1.3	0.8	33.4	1.5
12970	P80_TE	0.1	0.0	0.0	0.1	16.0	0.6	1.1	1.3	0.0	0.2	0.0	0.0	0.9	0.0
12630	P85-D_TE	0.1	0.0	0.0	0.1	15.8	0.6	1.1	1.3	0.0	0.2	0.0	0.0	0.7	0.0
12446	P90_TE	272.4	24.0	0.3	1.2	17.1	1.1	3.3	18.2	2.0	58.1	0.8	0.6	8.4	2.1
12238	P95_TE	0.1	0.0	0.0	0.1	15.9	0.6	1.0	1.3	0.0	0.1	0.0	0.0	0.6	0.0
11950	P100_TE	0.1	0.0	0.0	0.1	16.0	0.6	1.1	1.3	0.0	0.1	0.0	0.0	0.7	0.0
11741	P105_TE	0.1	0.0	0.0	0.1	15.9	0.6	1.0	1.5	0.0	0.1	0.0	0.0	0.6	0.0

11609	P110_TE	182.3	9.2	0.4	1.3	61.0	1.0	4.1	8.3	1.2	43.8	0.6	0.8	16.8	1.7
11419	P115_TE	150.2	9.1	0.6	1.5	9.5	1.0	2.8	12.1	1.5	37.8	0.6	1.1	4.5	1.6
11217	P120-D_TE	0.1	0.0	0.0	0.1	16.2	0.6	1.1	1.4	0.0	0.1	0.0	0.0	0.7	0.0
11071	P125-D_TE	0.1	0.0	0.0	0.1	16.0	0.6	1.1	1.1	0.0	0.1	0.0	0.0	0.6	0.0
11071	P125_TE	100.3	5.7	0.3	1.2	8.6	0.6	1.8	12.9	1.1	24.8	0.4	0.6	5.0	0.9
10927	P130_TE	311.9	25.3	0.8	1.8	35.5	1.1	6.6	51.6	2.3	81.5	0.6	1.3	19.7	2.4
10838	P135_TE	0.1	0.0	0.0	0.1	16.0	0.6	1.0	1.1	0.0	0.1	0.0	0.0	0.7	0.0
10735	P140_TE	238.2	13.1	0.4	2.5	15.4	0.9	3.9	22.1	1.5	56.8	0.7	7.8	7.1	2.3
10557	P145_TE	436.4	18.5	0.3	1.8	115.8	1.0	7.1	40.0	2.8	75.2	1.5	0.8	22.0	2.3
10360	P150_TE	0.1	0.0	0.0	0.1	16.2	0.6	1.0	1.2	0.0	0.1	0.0	0.0	0.6	0.0
10259	P155_TE	414.8	24.7	0.6	1.9	34.8	1.2	9.5	71.8	2.5	100.6	0.8	1.4	24.4	3.4
10170	P160_TE	0.1	0.0	0.0	0.1	16.1	0.6	1.1	1.1	0.0	0.1	0.0	0.0	0.8	0.0
10082	P165-D_TE	0.1	0.0	0.0	0.1	16.1	0.6	1.1	1.1	0.0	0.1	0.0	0.0	0.7	0.0
9980	P170_TE	181.0	9.7	0.5	1.3	13.1	1.1	4.1	15.2	1.4	39.4	0.6	0.6	5.0	1.4
9864	P175_TE	230.3	9.3	0.6	1.7	18.0	1.0	4.2	12.4	1.5	47.7	0.7	0.6	7.0	1.7
9722	P180_TE	155.3	12.8	0.3	1.1	31.8	1.0	6.0	11.9	2.6	36.5	0.6	0.8	12.8	1.4
9587	P185_TE	405.3	15.1	0.6	1.3	40.5	1.0	7.7	116.3	4.5	85.0	0.7	0.8	59.2	2.4
9458	P190_TE	189.4	12.2	0.3	1.0	45.4	0.9	2.6	27.0	1.6	35.4	0.7	0.5	17.0	1.6
9351	P195_TE	139.8	9.4	0.2	1.3	12.6	0.6	2.6	14.0	0.9	31.1	0.4	0.4	4.8	1.2
9247	P200_TE	417.8	36.5	0.5	4.2	29.5	0.9	6.8	50.8	3.9	94.8	1.1	0.7	11.4	3.1
9076	P205_TE	106.8	3.7	0.4	0.9	5.7	0.4	1.7	16.7	1.4	25.2	0.3	1.1	3.2	0.9
8843	P210_TE	127.0	8.5	0.4	1.3	10.9	1.3	2.4	19.3	2.2	28.1	1.3	0.5	13.5	1.4
0	R01	100.3	7.7	0.8	1.0	8.3	2.3	15.9	20.6	3.2	24.8	0.4	2.4	8.1	1.5
15333	N91surface_TE	95.9	16.2	0.4	1.2	6.6	0.8	2.8	12.5	1.0	32.1	0.2	1.0	4.3	1.3

Table 4.S1. Trace element concentrations of Taylor Glacier ice samples. Also shown is approximate sample age.

Approximate Age	Sample Name	La	Ce	Pr	Nd	Eu	Sm	Gd	Tb	Dy	Ho	Er	Tm	Yb	Lu
	Blank 1	1.55	0.98	0.05	0.06	0.10	0.23	0.03	0.28	0.01	0.00	0.01	0.00	0.01	0.00
	Blank 2	0.13	0.74	0.06	0.13	0.21	0.43	0.13	0.07	0.28	0.07	0.11	0.06	0.08	0.12
46711	N203	5.46	16.59	1.76	6.05	0.43	1.55	1.12	0.20	1.06	0.20	0.45	0.10	2.42	0.08
44374	N196	23.77	130.47	12.86	56.06	1.38	7.01	4.81	0.66	3.49	0.67	1.73	0.29	1.61	0.27
41788	N189	26.93	102.61	10.43	45.43	1.88	5.20	3.72	0.49	3.50	0.52	1.33	0.19	1.26	0.17
36281	N168	17.96	49.62	5.80	20.46	1.26	5.28	5.00	0.64	3.57	3.40	1.87	0.28	1.45	0.26
34510	N161	9.92	20.90	2.81	9.04	0.57	2.37	1.85	0.27	1.41	0.29	0.78	0.12	0.68	0.11
32247	N154	30.17	114.20	11.38	49.22	1.18	5.94	4.25	0.56	3.08	0.59	1.59	0.22	1.37	0.21
30080	N147	24.44	79.86	8.93	31.66	1.75	8.00	7.06	0.97	5.35	1.12	3.28	0.43	2.79	0.42
28828	N140	17.13	34.52	3.60	12.24	0.68	3.17	2.51	0.37	2.02	0.41	1.04	0.16	0.87	0.16
26820	N133	152.35	460.82	53.86	196.06	10.17	46.65	44.03	5.99	35.96	6.66	18.83	2.57	16.75	2.57
24446	N126	41.69	130.00	14.57	51.66	3.30	13.02	11.06	1.54	8.47	1.74	4.83	0.70	3.90	0.69
21891	N119	61.20	186.81	19.27	67.42	3.69	16.15	16.38	2.10	11.51	2.33	6.27	0.93	5.16	0.82
19130	N112	40.62	122.19	15.15	52.58	2.79	12.76	11.31	1.64	8.36	1.77	5.08	0.72	4.30	0.74
17138	N105	10.33	30.17	5.35	13.09	0.84	3.37	3.00	0.45	2.47	0.48	1.28	0.21	1.15	0.19
16116	N98	5.91	19.57	2.29	7.88	0.62	2.28	1.93	0.29	1.55	0.32	0.83	0.15	0.75	0.13
16035	P20	9.48	24.31	3.05	10.31	0.75	3.20	2.24	0.35	1.86	0.39	1.03	0.19	0.85	0.17
15588	P25	24.91	97.45	9.78	43.84	1.13	4.91	3.65	0.47	2.57	0.49	1.28	5.09	1.19	0.17
15333	N91	5.75	14.19	1.74	5.65	0.44	1.51	1.26	0.20	0.91	0.21	0.54	0.11	0.50	0.12
14849	P35	22.81	95.86	9.19	42.11	0.85	4.19	2.96	0.35	1.90	0.36	0.96	0.14	0.97	0.13
14491	P40	0.61	1.91	0.22	0.79	0.19	0.41	0.19	0.05	0.12	0.05	0.08	0.04	0.07	0.06
14328	P45	20.32	87.77	8.39	38.74	0.85	3.60	2.13	0.29	1.43	0.28	0.74	0.13	0.69	0.10
14019	P50	14.33	74.95	7.05	34.10	2.56	2.72	1.33	0.17	0.92	0.17	0.42	0.07	0.41	0.07
13835	P55	18.05	85.31	8.11	37.43	0.81	3.32	3.91	0.24	1.52	0.23	0.60	0.32	1.08	0.09
13588	P60	2.43	4.38	0.56	1.89	0.20	0.62	0.35	0.07	0.27	0.06	0.13	0.03	0.12	0.03

13466	P65	8.63	32.38	3.26	14.39	0.54	1.67	0.88	0.12	0.88	0.13	0.32	0.06	0.44	0.05
13286	P70	5.22	6.90	0.79	2.78	0.21	0.83	0.57	0.09	0.39	0.09	0.23	0.06	0.44	0.04
13174	P75	2.22	6.13	0.73	2.50	0.28	0.79	0.62	0.09	2.13	0.10	0.20	0.06	0.18	0.06
12970	P80	23.05	91.93	8.81	40.08	2.55	3.84	2.35	0.30	3.68	0.29	0.77	0.11	0.73	0.11
12630	P85	19.92	86.78	8.29	38.06	1.01	3.43	1.85	0.25	1.49	0.24	0.64	0.10	0.65	0.10
12446	P90	1.45	2.78	0.35	1.11	0.20	0.49	0.20	0.03	0.14	0.04	0.08	0.02	0.07	0.02
12238	P95	14.82	78.16	7.39	39.00	0.58	2.81	1.39	0.19	0.91	0.18	0.45	0.08	0.43	0.07
11950	P100	15.06	76.12	7.20	33.83	0.57	2.77	1.30	0.19	0.92	0.17	0.47	0.07	0.46	0.07
11741	P105	16.00	77.49	7.31	34.60	0.64	2.87	1.36	0.19	1.04	0.19	0.49	0.08	0.44	0.07
11609	P110	2.74	7.12	1.67	2.25	0.24	0.67	0.42	0.08	0.32	0.08	0.20	0.06	0.21	0.06
11419	P115	20.11	9.02	0.81	2.66	0.25	0.79	0.52	0.08	0.32	0.08	0.21	0.05	0.14	0.05
11217	P120	17.28	83.51	7.86	36.48	0.75	3.07	2.27	0.22	1.18	0.21	0.57	0.10	0.74	0.09
11071	P125D	16.31	82.23	7.79	36.56	0.64	3.01	1.55	0.21	1.06	0.21	0.53	0.09	0.50	0.08
11071	P125	1.83	4.87	0.60	1.96	0.25	0.64	0.45	0.08	0.27	0.07	0.15	0.06	0.29	0.04
10927	P130	0.71	1.79	0.22	0.71	0.17	0.43	0.16	0.05	0.10	0.05	0.10	0.04	0.07	0.04
10838	P135	15.43	80.57	7.61	35.98	0.93	3.01	1.46	0.19	1.24	0.18	0.49	0.08	0.49	0.09
10735	P140	1.06	2.48	0.30	1.07	0.17	0.49	0.23	0.08	0.18	0.06	0.10	0.04	0.10	0.04
10557	P145	0.53	1.06	0.12	0.46	0.17	0.38	0.11	0.02	0.06	0.02	0.04	0.02	0.03	0.02
10360	P150	16.51	85.07	7.65	36.02	0.65	3.22	1.55	0.22	1.06	0.21	0.56	0.10	0.53	0.08
10259	P155	0.66	1.14	0.25	0.52	0.16	0.40	0.16	0.04	0.10	0.05	0.07	0.04	0.07	0.03
10170	P160	15.73	79.26	7.59	35.82	0.63	2.94	1.47	0.21	1.07	0.21	0.50	0.09	0.53	0.08
10082	P165	15.13	76.84	7.26	34.31	1.14	2.87	1.33	0.18	1.26	0.17	0.45	0.07	0.39	0.07
9980	P170	2.27	6.39	0.89	2.61	0.25	0.89	0.46	0.08	0.32	0.08	0.16	0.04	0.12	0.06
9864	P175	1.34	3.46	0.39	1.28	0.18	0.55	0.36	0.09	0.36	0.08	0.19	0.05	0.15	0.04
9722	P180	1.76	4.69	0.51	1.72	0.29	0.59	0.38	0.06	0.68	0.07	0.13	0.04	0.11	0.04
9587	P185	0.60	1.09	0.15	0.44	0.19	0.39	0.13	0.04	0.08	0.04	0.06	0.05	0.07	0.04
9458	P190	2.33	4.51	0.53	1.75	0.21	0.57	0.32	0.05	0.23	0.05	0.12	0.03	0.09	0.04

9351	P195	1.09	3.20	0.65	1.23	0.20	0.55	0.31	0.06	0.17	0.13	0.11	0.05	0.09	0.05
9247	P200	0.63	1.57	0.23	0.71	0.19	0.43	0.19	0.05	0.16	0.05	0.07	0.04	0.08	0.05
9076	P205	1.43	3.49	0.40	1.57	0.19	0.54	0.29	0.06	0.18	0.06	0.11	0.04	0.12	0.04
8843	P210	5.08	14.71	1.65	5.64	0.34	1.40	1.02	0.19	0.79	0.20	0.48	0.18	0.50	0.09
0	R01	8.96	41.40	3.06	10.51	0.85	2.61	2.05	0.25	1.13	0.22	0.52	0.10	0.49	0.10
15333	N91-surface	1.98	5.71	0.66	2.24	0.26	0.86	0.53	0.10	0.49	0.11	0.23	0.06	0.32	0.07

Table 4.S2. Rare earth element concentrations of Taylor Glacier samples and approximate ages.

Approximate Age	Sample Name	Chloride (ppb)
46711	N203	112.33
44374	N196	172.00
36281	N168	127.83
34510	N161	251.83
30080	N147	283.33
28828	N140	185.17
26820	N133	353.00
24446	N126	327.33
21891	N119	233.00
19130	N112	266.50
17138	N105	391.00
16116	N98	228.17
16035	P20	220.67
15333	N91	342.50
13588	P60	65.83
13174	P75	156.00
12446	P90	182.33
11609	P110	107.00
11419	P115	156.50
11071	P125	192.17
10927	P130	194.33
10735	P140	169.33
10557	P145	66.33
10259	P155	161.33
9980	P170	227.00
9864	P175	85.00
9722	P180	217.50
9587	P185	125.67
9458	P190	231.17
9351	P195	267.67
9247	P200	195.00
9076	P205	205.17
8843	P210	199.67
8725	P215	261.67
0	R01	135.33

Table 4.S3. Chloride concentration of Taylor Glacier ice samples and approximate ages.

Approximate Age	Sample Name	dust concentration (ppb) (0.6-5 micron)	SD (0.6-5 micron)	dust concentration (ppb) (5-10 micron)	SD (5-10 micron)
46711	N203	56.18	1.40	9.48	1.51
44374	N196	144.07	0.04	6.14	5.14
36281	N168	112.46	1.62	6.68	1.58
34510	N161	121.69	1.88	12.85	4.66
30080	N147	376.76	1.47	13.80	3.41
28828	N140	226.25	3.32	10.79	3.97
26820	N133	2488.48	7.35	124.90	25.92
24446	N126	524.63		87.25	
21891	N119	901.85	0.10	16.69	5.03
19130	N112	383.23	4.64	25.69	4.00
17138	N105	190.43	6.90	14.22	4.73
16116	N098	92.79	0.67	1.04	0.21
15333	N091	83.86	0.93	11.38	2.96
16035	P020	208.03	6.35	18.65	6.24
14491	P040	7.29	0.39	1.18	1.67
13588	P060	22.44	1.96	3.32	2.10
13286	P070	31.06	1.06	2.99	1.77
13174	P075	13.86	0.05	4.09	3.49
12446	P090	13.73	0.91	3.00	2.83
11609	P110	20.59	0.81	3.15	1.65
11419	P115	22.85	2.12	1.45	1.00
11071	P125	24.80	4.14	8.69	7.92
10927	P130	5.72	0.51	2.64	3.74
10735	P140	11.53	1.59	4.41	4.52
10557	P145	5.06	0.12	1.82	0.31
10360	P150	6.73	0.39	0.00	0.00
10259	P155	6.54	0.62	2.10	0.52
9980	P170	10.46	0.53	2.05	2.91
9864	P175	11.49	0.88	1.17	0.27
9722	P180	19.68	2.02	9.24	2.49
9587	P185	4.69	0.44	3.63	2.64
9458	P190	23.71	1.06	4.81	2.05
9351	P195	45.49	0.22	39.63	6.28
9247	P200	10.14	0.39	0.37	0.52
9076	P205	7.92	0.54	4.46	3.29
8843	P210	17.60	0.19	3.85	0.50
8725	P215	7.66	0.84	2.33	0.87
0	R01	15.88	1.75	1.32	0.35
15333	N91-surface	32.00	1.05	2.07	1.84

Table 4.S4. Dust concentration and size distribution data for Taylor Glacier samples and approximate ages.

Sample ID	Latitude (S)	Longitude (E)	Approximate age (yr BP)	$^{87}Sr/^{86}Sr$	Sr $\pm 2\sigma 10^{-6}$	ϵ_{Nd} $\pm 2\sigma 10^{-6}$	Nd $\pm 2\sigma$
N203 W	77°45.613'	161°43.424'	46711	0.708990	34	-1.5	0.8
N196 W	77°45.612'	161°43.408'	44374	0.708701	28	-0.1	0.8
N168 W	77°45.599'	161°43.360'	36281	0.708422	29	1.7	1.2
N161 W	77°45.596'	161°43.349'	34510	0.708670	29	-1.7	1.4
N147 W	77°45.592'	161°43.339'	30080	0.708651	18	-1.3	0.4
N140 W	77°45.589'	161°43.311'	28828	0.708822	24	-0.7	0.9
N133 W	77°45.586'	161°43.301'	26820	0.708341	17	0.7	0.3
N126 W	77°45.583'	161°43.286'	24446	0.708473	24	-0.8	0.6
N119 W	77°45.580'	161°43.272'	21891	0.708195	17	0.4	0.6
N112 W	77°45.578'	161°43.277'	19130	0.708514	21	-1.3	0.4
N105 W	77°45.574'	161°43.260'	17138	0.708574	43	-0.9	0.5
N98 W	77°45.562'	161°43.250'	16116	0.709519	16	-1.5	0.6
N91 W	77°45.571'	161°43.238'	15333	0.707652	13	-	-
P20 W	77°45.528'	161°43.033'	16035	0.708554	131	-1.1	0.3
P40 W	77°45.487'	161°43.098'	14491	0.709288	50	-2.6	0.7
P60 W	77°45.511'	161°42.961'	13588	0.708631	17	-1.1	1.5
P75 W	77°45.508'	161°42.943'	13174	0.709005	49	-3.0	0.6
P90 W	77°45.499'	161°42.912'	12446	0.708561	29	-1.5	1.2
P110 W	77°45.493'	161°42.869'	11609	0.709256	53	-	-
P115 W	77°45.492'	161°42.861'	11419	0.708771	19	-2.1	1.2
P125 W	77°45.488'	161°42.848'	11071	0.708776	19	-2.1	1.2
P130 W	77°45.486'	161°42.832'	10927	0.707843	35	-0.9	0.1
P140 W	77°45.481'	161°42.820'	10735	0.709223	58	-2.7	1.3
P145 W	77°45.479'	161°42.807'	10557	0.709266	25	-2.8	1.2
P155 W	77°45.475'	161°42.794'	10259	0.708828	45	-0.1	0.4
P165 W	77°45.471'	161°42.776'	10082	-	-	-	-
P170 W	77°45.470'	161°42.768'	9980	0.708841	36	-0.1	1.0
P175 W	77°45.468'	161°42.757'	9864	0.710252	197	-0.9	0.8
P180 W	77°45.465'	161°42.753'	9722	0.709071	27	-0.5	1.3
P185 W	77°45.463'	161°42.750'	9587	0.709097	33	-3.8	3.8
P190 W	77°45.462'	161°42.728'	9458	0.709423	41	-2.9	1.5
P195 W	77°45.461'	161°42.719'	9351	0.709074	31	-	-
P200 W	77°45.457'	161°42.706'	9247	0.709078	22	-5.0	1.3
P205 W	77°45.455'	161°42.696'	9076	0.708631	25	-1.1	0.5
P210 W	77°45.455'	161°42.695'	8843	0.708132	20	-0.6	0.9
P215 W	77°45.454'	161°42.687'	8725	0.708883	30	-	-
R01 W	77°41.513'	160°57.849'	0	0.710564	37	-	-
N91-Surface W	77°45.571'	161°43.238'	15333	0.709061	28	-2.4	0.3

Table 4.S5. Radiogenic isotope compositions of soluble portion of Taylor Glacier ice samples. Soluble portion is denoted by 'W' following sample number. Sample names, strontium and neodymium isotopic compositions, latitude, longitude, and approximate age based are noted.

4.8.1.2 Figures

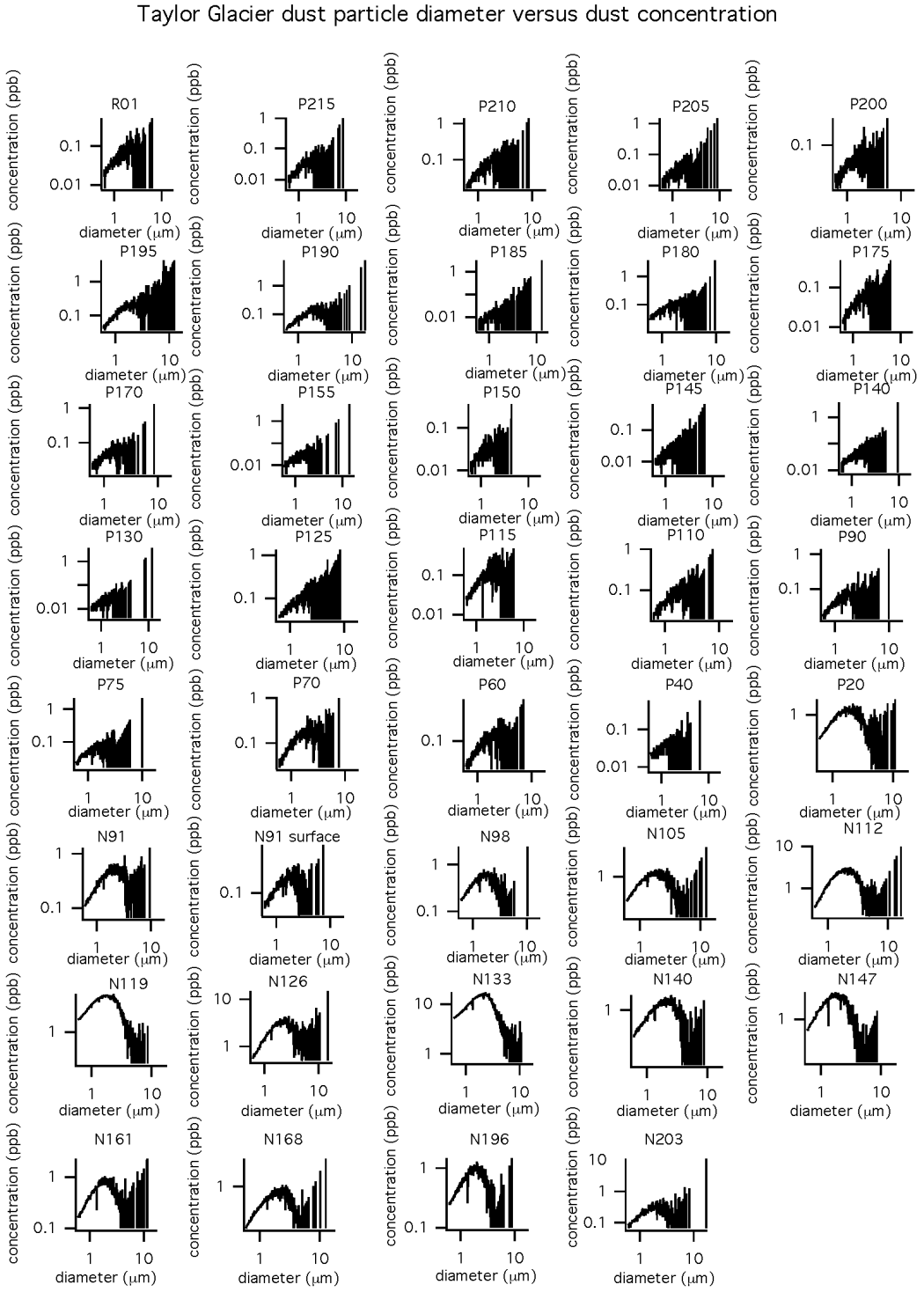

Figure 4.S1. Particle size distributions of samples measured from Taylor Glacier. For sample codes see Table 4.S1.

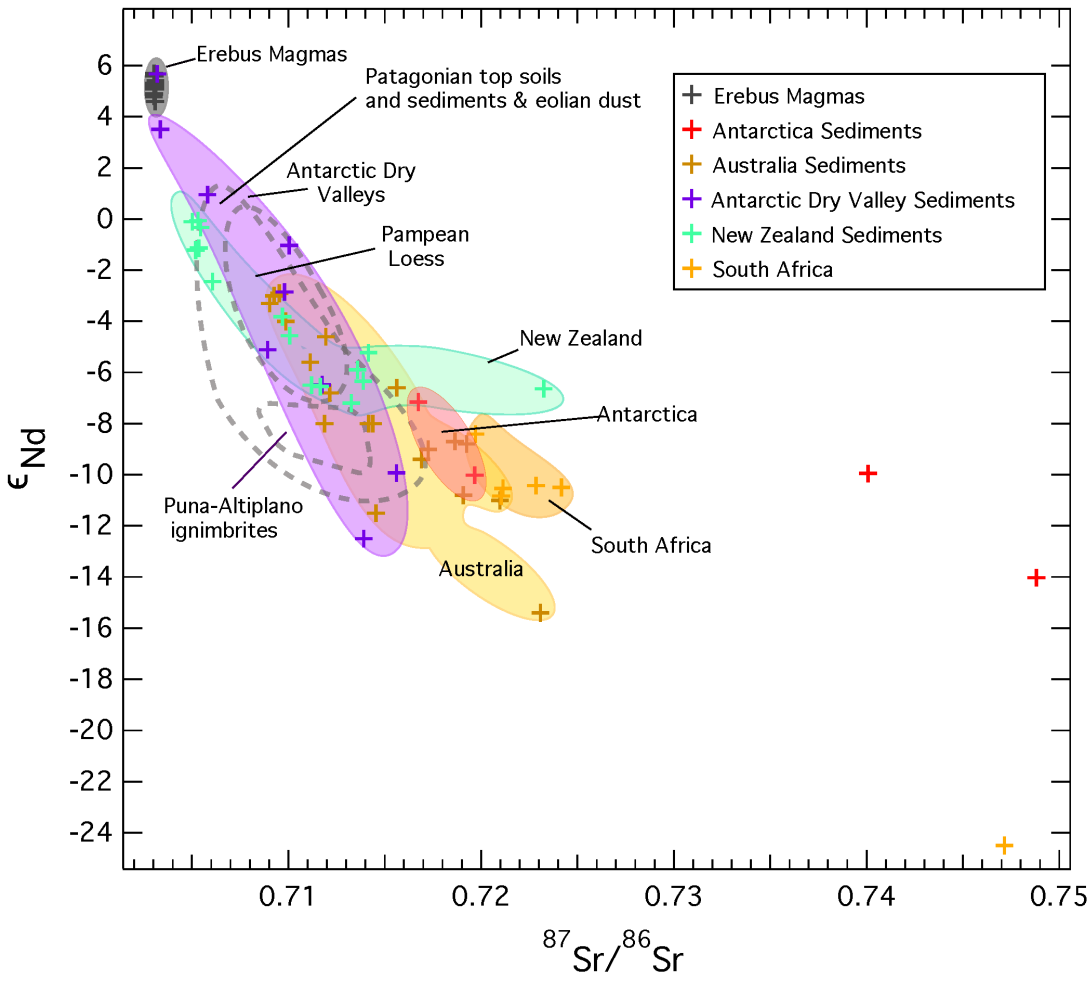

Figure 4.S2. Radiogenic isotopic compositions of potential source areas in the Southern Hemisphere plotted in various colors (colored crosses are individual data points) (Blakowski et al., In Press; Delmonte et al., 2010; Delmonte et al., 2004a; Gaiero, 2007; Grousset et al., 1992; Revel-Rolland et al., 2006; Sims et al., 2008).

4.8.2 References

Blakowski, M.A., Aciego, S.M., Delmonte, B., Baroni, C., Salvatore, M.C., Sims, K.W.W., In Press. Sr-Nd-Hf isotope characterization of dust source areas in Victoria Land and the McMurdo Sound sector of Antarctica. Quaternary Science Reviews.

Delmonte, B., Baroni, C., Andersson, P.S., Schoberg, H., Hansson, M., Aciego, S., Petit, J.R., Albani, S., Mazzola, C., Maggi, V., Frezzotti, M., 2010. Aeolian dust in the Talos Dome ice core (East Antarctica, Pacific/Ross Sea sector): Victoria Land versus remote sources over the last two climate cycles. Journal of Quaternary Science 25, 1327-1337.

Delmonte, B., Basile-Doelsch, I., Petit, J., Maggi, V., Revel-Rolland, M., Michard, A., Jagoutz, E., Grousset, F., 2004a. Comparing the EPICA and Vostok dust records during the last 220,000 years: stratigraphical correlation and provenance in glacial periods. Earth-Science Reviews 66, 63-87.

Gaiero, D.M., 2007. Dust provenance in Antarctic ice during glacial periods: from where in southern South America? Geophysical Research Letters 34.

Grousset, F.E., Biscaye, P.E., Revel, M., Petit, J.-R., Pye, K., Joussaume, S., Jouzel, J., 1992. Antarctic (Dome C) ice-core dust at 18 k.y. B.P.: Isotopic constraints on origins. Earth and Planetary Science Letters 111, 175-182.

Revel-Rolland, M., De Deckker, P., Delmonte, B., Hesse, P., Magee, J., Basile-Doelsch, I., Grousset, F., Bosch, D., 2006. Eastern Australia: a possible source of dust in East Antarctica interglacial ice. Earth and Planetary Science Letters 249, 1-13.

Sims, K.W.W., Blichert-Toft, J., Kyle, P.R., Pichat, S., Gauthier, P.-J., Blusztajn, J., Kelly, P., Ball, L., Layne, G., 2008. A Sr, Nd, Hf, and Pb isotope perspective on the genesis and long-term evolution of alkaline magmas from Erebus volcano, Antarctica. Journal of Volcanology and Geothermal Research 177, 606-618.

Chapter V

Conclusion: Geochemical analysis of dust record preserved in ice cores

This thesis presents a comprehensive set of data characterizing the dust cycle preserved in the ice core record on both short and long timescales. The research used a multi-proxy approach of dust entrained in ice to provide the most accurate characterization of dust provenance, and included the measurement of radiogenic isotopes (strontium, neodymium), trace and rare earth elements, dust concentration and size distribution and anion concentration. All of these parameters place constraints on dust source region and sources of soluble elements (i.e. sea salt aerosol). Understanding the changes in atmospheric transport pathways and dust sources in tandem with documented climate change and anthropogenic activity provide a preliminary projection for future changes to the dust cycle with an emphasis on the effects of regional and global climate change. To address natural and anthropogenically-driven changes in the dust cycle, high-precision geochemical techniques are applied to ice from the Upper Fremont Glacier, Wind River Range, Wyoming, USA, Taylor Dome, Antarctica and Taylor Glacier, Antarctica.

However, the developed research has limitations. Despite multiple physical and chemical proxies for dust provenance, there is still some uncertainty in determining the exact point of origin due to limited potential source area databases, and mixing or possible fractionation of dust during transport. Additionally, extremely small amounts of dust create analytical limitations in terms of radiogenic isotope measurement. Doubling the sample size of Taylor Glacier Holocene samples would likely improve the successful measurement of strontium and neodymium isotopes, however this is not an option in traditional ice core analyses.

5.1 Summary of Conclusions

5.1.1. Chapter 2: A record of dust throughout the Anthropocene

A record of dust deposition at a midlatitude alpine glacier had never before been explored. Our research (Chapter 2) provided a semi-continuous record of North American dust throughout the Agricultural and Industrial Revolution to (1) determine if the changing climate and weather in the western United States coming out of the Little Ice Age (1350-1850 A.D.) through today is recorded by the aerosol compositional changes, and (2) identify regional versus global aerosol flux sources to midlatitude glaciers. Ice cores provide an ultra-pure and continuous record of climate uncontaminated by local sedimentary input from rivers and streams (i.e. lake sediment cores) and can span longer time periods than modern in-situ measurements.

The study focusing on the Upper Fremont Glacier showed that the sources and pathways of dust in the western United States changed significantly from ~1715-1998 A.D. The dust size distribution data combined with radiogenic isotope compositions indicates the dust source region has transitioned from a far to near-range transport, perhaps a reflection of increasing agricultural activity and human population during the time period of study (Aarons et al., in preparation). The Increased dust availability, transport and flux response is complemented by satellite (Prospero et al., 2002) and sediment core data (Brahney et al., 2013; Neff et al., 2008);(Brahney et al., 2014);(Doebbert et al., 2014) of the anthropogenic influence on the dust cycle of the western United States.

5.1.2. Chapter 3: Characterization of dust to East Antarctica during Holocene

Due to the extremely low concentration of dust present in polar glacial ice, previously unobtainable radiogenic isotope measurements are presented here. Earlier studies averaged interglacial samples over longer time periods to obtain enough dust to accurately and precisely measure radiogenic isotope composition (Delmonte et al., 2010). In addition to dust provenance work, trace element concentrations served as an indicator of ice shelf or sea ice extent. In this study we used the sodium to strontium ratio to serve as a proxy for sea salt contribution, which should be reflective of the proximity of young sea ice.

This dissertation represents a substantial advancement in understanding the dust cycle in the Southern Hemisphere as previously unavailable datasets of

interglacial dust composition are presented (Chapters 3 and 4). We first established baseline measurements on the Taylor Dome ice core of trace elements, anions, dust concentration and size distributions, Sr, and Nd isotopes for the time period of ~31.4 to 1.1 ka (Chapter 3) (Aarons et al., In Press). Our results show that the sources of dust to Taylor Dome during the Last Glacial Period are different than the Holocene, and that the dust transport has most likely shifted from a long-range, globally transported source to more local, regionally transported source. The retreat of the Ross Ice Shelf associated with the deglaciation is reflected in the chemical and physical record of dust in the Taylor Dome ice core. These samples provided initial, discontinuous observations of dust changes and acted as a comparison for Taylor Glacier samples.

5.1.3. Chapter 4: A high-resolution record of dust compositional changes during a major climate transition

The work on Taylor Glacier expanded the time period of study from ~47 to 0 ka and provided a higher temporal resolution (Chapter 4). The work on the Taylor Glacier ice cores is transformative in the sense that we have generated a precise, high-resolution record over periods of well-established rapid regional and global climate change and we provide the first high temporal resolution radiogenic isotope data for dust deposited in East Antarctica during the Holocene. We show that the average Sr and Nd radiogenic isotope composition changes from 0.709456 to 0.711322 and -2.4 to -3.9 during the transition from

the Last Glacial Period to the Holocene respectively, and our large sampling strategy ensures that this observation is statistically significant.

Our results support the work established in Chapter 3, that a regional atmospheric transport restructuring occurred following the dramatic retreat of the Ross Ice Shelf. The data includes new trace element concentrations of samples throughout the time period of study and provide context to chemical and physical variations with respect the changing location of the Ross Ice Shelf grounding line. The sources of dust to Taylor Glacier changed from Southern South America during the Last Glacial Period to more varied local sources during the Holocene, and it is likely that the transport pathways are continuing to evolve as a 'zero-age' sample is in agreement with dust originating from Australia (Aarons et al., In Prep.). This research provides new insight into the changes in dust sources and pathways occurring during major global climate shifts (i.e. transition from Last Glacial Period to Holocene) as well as more regional shifts (i.e. rapid retreat in Ross Ice Shelf), and may serve as a preliminary indicator of changes in the dust cycle.

5.2 References

Aarons, S.M., Aciego, S.M., Arendt, C.A., Steigmeyer, A., Gabrielli, P., Sierra-Hernandez, R., Delmonte, B., Baccolo, G., K., P., May, N., In Prep. Dust aerosol composition changes in East Antarctica during Glacial-Interglacial transition. Quaternary Science Reviews.

Aarons, S.M., Aciego, S.M., Gabrielli, P., Delmonte, B., Koornneef, J.M., Wegner, A., Blakowski, M.A., In Press. The impact of glacier retreat from the Ross Sea on local climate: characterization of mineral dust in the Taylor Dome ice core, East Antarctica. Earth and Planetary Science Letters.

Aarons, S.M., Aciego, S.M., Gabrielli, P., Delmonte, B., Koornneef, J.M., Wegner, A., Blakowski, M.A., Bouman, C., in preparation. Ice core evidence for variable dust sources in the western United States over the last 300 years. Chemical Geology.

Brahney, J., Ballantyne, A.P., Kociolek, P., Spaulding, S., Otu, M., Porwoll, T., Neff, J.C., 2014. Dust mediated transfer of phosphorus to alpine lake ecosystems of the Wind River Range, Wyoming, USA. Biogeochemistry 120, 259-278.

Brahney, J., Ballantyne, A.P., Sievers, C., Neff, J.C., 2013. Increasing Ca2+ deposition in the western US: The role of mineral aerosols. Aeolian Research 10, 77-87.

Delmonte, B., Baroni, C., Andersson, P.S., Schoberg, H., Hansson, M., Aciego, S., Petit, J.R., Albani, S., Mazzola, C., Maggi, V., Frezzotti, M., 2010. Aeolian dust in the Talos Dome ice core (East Antarctica, Pacific/Ross Sea sector): Victoria Land versus remote sources over the last two climate cycles. Journal of Quaternary Science 25, 1327-1337.

Doebbert, A.C., Johnson, C.M., Carroll, A.R., Beard, B.L., Pietras, J.T., Carson, M.R., Norsted, B., Throckmorton, L.A., 2014. Controls on Sr isotopic evolution in lacustrine systems: Eocene green river formation, Wyoming. Chemical Geology 380, 172-189.

Neff, J.C., Ballantyne, A.P., Farmer, G.L., Mahowald, N.M., Conroy, J.L., Landry, C.C., Overpeck, J.T., Painter, T.H., Lawrence, C.R., Reynolds, R.L., 2008. Increasing eolian dust deposition in the western United States linked to human activity. Nature Geoscience 1, 189-195.

Prospero, J.M., Ginoux, P., Torres, O., Nicholson, S.E., Gill, T.E., 2002. Environmental characterization of global sources of atmospheric soil dust identified with the Nimbus 7 Total Ozone Mapping Spectrometer (TOMS) absorbing aerosol product. Reviews of Geophysics 40.